Title

Investigation of Ceramic Breeder Pebble Beds Thermo-mechanics with Volumetric Heating and Temperature Gradients Representative of the Fusion Nuclear Environment

Author

Mohammed, Mahmoud

Publication Date

2018

Peer reviewed|Thesis/dissertation

UNIVERSITY OF CALIFORNIA

Los Angeles

Investigation of Ceramic Breeder Pebble Beds Thermo-mechanics with Volumetric Heating and Temperature Gradients Representative of the Fusion Nuclear Environment

A dissertation submitted in partial satisfaction

of the requirements for the degree

Doctor of Philosophy in Mechanical Engineering

by

Mahmoud Lotfy Mohammed

2018

ABSTRACT OF THE DISSERTATION

Investigation of Ceramic Breeder Pebble Beds Thermo-mechanics with Volumetric Heating and Temperature Gradients Representative of the Fusion Nuclear Environment

by

Mahmoud Lotfy Mohammed

Doctoral of Philosophy in Mechanical Engineering

University of California, Los Angeles, 2018

Professor Mohamed A. Abdou, Chair

Ceramic breeder pebble beds undergo complex thermo-mechanical interactions during blanket operations due to stress build-up and relaxation under the effects of confined thermal expansion, thermal cycling, and creep. Understanding the evolution of such processes can aid in guiding blanket design/assembly, breeder materials developments, predicting performance and possible failure modes identification and remedy. Experimental efforts on ceramic pebble beds and their associated constitutive equations have been derived from single effect tests where one parameter is varied and its effects are isolated and studied separately (e.g. using constant temperatures and externally applied loads). These experiments are incapable of reproducing the true multiple/synergistic effects of the physics that occur in real blankets, and the phenomena arising from the interactions of single effects are yet to be discovered. For example, it is unclear

whether the combined effect of plasticity and creep under reactor-relevant loading conditions will either enable the altered pebble bed packing configuration to reach an acceptable self-regulating temperature state, or significantly deteriorate its heat transfer efficiency and subsequent tritium release. Therefore, studying the isolated thermal and mechanical effects is not sufficient to predict pebble bed behavior; it is the coupling and interdependence between the dynamic thermal and mechanical fields, as well as the synergistic effects between the various modes of deformation that is key to fully understand and predict the pebble bed behavior in a realistic fusion environment.

Previous mock-up experimental campaigns thus far have suffered from critical shortfalls which severely hamstringed their scientific impact. The lack of experimental data that incorporates multiple-effects interaction in addition to the complexity of building a full-scaled breeder unit mock-up triggered the need for this experimental and modeling effort. The body of work presented in this document served the following key points: (1) established and validated the practicality of various volumetric heating simulation techniques for representative thermo-mechanics study, (2) recreated prototypical breeder unit's thermal-hydraulic behavior using a scaled-down reduced activation ferretic steel box with optimized manifold design connected to oil cooling loop facility, (3) evaluated the pebble bed thermo-mechanics using a novel non-intrusive in-situ tactile pressure sensing technology capable of generating real-time contact pressure maps that reveal the spatial and temporal stress evolution with emphasis on understanding the roles that each of the thermo-mechanical forces play in dictating the pebble bed's equilibrium operating conditions, and (4) developed and benchmarked thermo-mechanical Finite Element Method (FEM) code that is able to predict the pebble bed's thermo-mechanical evolution under the effects of creep and thermal cycling, in addition to providing useful extrapolations beyond the experimental limitations. Accordingly, this study introduces first-of-a-kind experimental techniques that enable us to both

create as well as investigate an environment in which the pebble bed stresses are organically generated as a result of relevant temperature gradients and magnitudes that allows for observing the combined thermo-mechanical interaction effects on contact pressure rise and fall, as well as temperature fluctuations.

A comprehensive picture of the stress distribution and evolution with time and thermal cycling inside the pebble bed was captured and carefully investigated. The real-time in-situ spatial and temporal thermo-mechanical interactions and evolution were captured under reactor-relevant conditions for the first time using the novel tactile pressure sensor technology. Two types of bed-wall contact pressure drop were recorded: (1) within the subsequent cycles due to pebbles irreversible rearrangements, and (2) within the cycle itself as a result of creep/stress-relaxation. The measured stresses were self-generated, unlike previous experiments where an external force has to be applied on the bed. Similarly, two mechanisms of self-regulation that contributed to the bed's thermo-mechanical stability were identified and studied: (1) stress self-regulation as a result of pressure rise and fall due to thermal expansion and creep/thermal cycling, respectively, and (2) temperature self-regulation as the rise in temperatures caused by the deteriorated interface conductance and loosely packed pebbles with thermal cycling in the non-creep region is balanced by the temperature reduction in the core creep zone due to the locally enhanced thermal conductivity. These two mechanisms are highly desirable as they lower the probability of the events of pebbles crushing/further sintering and thermal runaways under high temperatures and poor heat extraction. The results also showed that the use of effective bed thermal conductivity, that is widely used in the solid breeder pebble bed community, needs to be reevaluated since the thermal conductivity is not only a function of temperature and pressure, but it also varies greatly with the spatial distribution in the bed. Moreover, the positive effects of creep have been

experimentally verified and new effects have been discovered. In addition to stress relief after the build-up caused by confined thermal expansion and irradiation-induced swelling, creep flattens out the temperature profile by locally enhanced thermal conductivity at the hottest core region (gradient smoothing) which not only reduces chances of thermal runaways by staying within the design temperature window, but may also allow the possibility of operating at higher Neutron Wall Load (NWL) after the first 24 hours of operation which could yield tremendous benefits for power extraction. Pebble bed pre-conditioning mechanisms have been investigated as part of the filling procedure and shown high promise of improving packing density and hence Tritium Breeding Ratio (TBR) and thermo-mechanical stability which would enable us to reach an optimal initial packing configuration that allows for safe operation within the design margins.

The phenomenological model developed and validated in this work assumes a pebble bed is a continuum medium and describes the typical overall behavior of the material under fusion-relevant conditions. The modeling incorporates previously derived constitutive equations and described the thermo-mechanical response of a pebble bed by a nonlinear elasticity law, a modified Drucker-Prager plasticity model, a creep model and temperature-dependent physical properties. Finally, a benchmark exercise has been carried out on the basis of the present phenomenological model. The results from the simulation have been compared to the experimental data, showing that the present modelling is suitable for thermo-mechanical analyses of fusion blankets. The model is able to quantify and map out the spatial and temporal stress distributions and evolution of the first thermal cycle as well as for continuous operation, which is experimentally proven to capture the maximum stress the bed will experience during operation. It can also extrapolate the stress results to every point in the bed after validating the interface stress distributions with experiments, which can (1) guide blanket designers in determining geometrical features, sizing components and

selecting materials, and (2) predict failure of pebbles. The model can also predict the spatial and temporal creep strain/stress relaxation evolution, which enables locating regions with high propensity of sintering and correlate creep strain with the volume % of sintered pebbles from experiments in order to assess what percentage of creep strain can be tolerated.

Furthermore, the findings of this work provide a comprehensive framework and guiding objectives to pave the way for "Next-Generation" ceramic breeder mock-up experiments. On the experimental side, test article dimensions' optimization recommendations were provided to account for incorporating various complex flange connections, minimizing packing disturbances, and allowing low wall temperature operation (300 °C at a minimum) for safe sensor operation. Further experimental enhancements that are necessary for a more fusion relevant environment have also been discusses in later chapters of this work. As for the modeling front, all the limitations were outlined and recommendations for using advanced techniques such as adaptive meshing, DEM/FEM coupling, and direct thermo-mechanical coupling were provided for use when the modeling technology and computational resources reach feasible levels. The work presented in this document not only provides novel experimental techniques and data that enhance our understanding of synergistic thermo-mechanical interactions and effects, but it also offers models that, through the validation presented in this work, can now be used to predict the first cycle and continuous operation thermo-mechanics characteristics critical to the success of breeder operations.

The dissertation of Mahmoud Lotfy Mohammed is approved.

Jaime Marian

Hossein Pirouz Kavehpour

Adrienne G Lavine

Mohamed A Abdou, Committee Chair

University of California, Los Angeles

2018

To my beloved grandmother, for supporting me through my journey, without whom none of my success would be possible.

- Mahmoud

Table of Contents

List of Figures

List of Tables

VITA

Education

UNIVERSITY OF CALIFORNIA, LOS ANGELES (UCLA) **Los Angeles, CA (Dec 2014)**

- Master of Science in Mechanical Engineering **GPA:3.85/4.00**

UNIVERSITY OF ILLINOIS at Urbana-Champaign (UIUC) **Urbana, IL (May 2013)**

- Bachelor of Science in Mechanical Engineering with Highest Honors (Summa Cum Laude) **GPA: 3.95/4.00**

Awards & Recognition

- American Nuclear Society Outstanding Research Paper and Presentation Award (2016)
- UCLA Mechanical & Aerospace Department Full 5-year Fellowship (2013, 2014, 2017)
- Named to the Dean's list for academic excellence– College of Engineering UIUC (2013)
- Elected member of the Tau Beta Pi Association -the oldest engineering honor society in the United States (2013)
- ASHRAE Henry Adams Scholarship (2013)
- The Arab American Association of Engineers & Architects Scholarship (2012)
- The University of Illinois –at Urbana-Champaign MechSE Alumni Scholarship (2012)
- ASME Power Division Scholarship (2012)
- The Lockheed Martin Scholarship for Undergraduate Engineers (2012)

Publications and Conference Presentations

- M. Lotfy et al., "Thermo-mechanical Solid Breeder Multiple Effects Experiment (TESOMEX) Construction and Volumetric Heating Analysis", Accepted for publication in Fusion Science and Technology Journal (2018)
- M. Lotfy et al., "Investigating Ceramic Breeder Pebble Beds Thermo-mechanics Evolution Using Novel Pressure Mapping Technology", Accepted for publication in Fusion Engineering and Design, Ref: FUSION10472. (2018)
- M. Lotfy et al., "Study on the Thermally-Induced Stress and Relaxation of Ceramic Breeder Pebble Beds", Fusion Science & Technology, Vol. 72, Issue 3 (2017). Won the American Nuclear Society TOFE Best Paper Award 2016.
- Invited presentation for the Safety/Accident Analysis Technical Session on "Ceramic Breeders Thermal Stress and Subtle Modes of Failure" at the 22nd American Nuclear Society Topical Meeting on the Technology of Fusion Energy (TOFE), August 21, 2016, Philadelphia,PA

Chapter 1

1. Introduction

Considering the dual threat of dwindling oil supplies and climate change, the need for a sustainable solution to the constantly growing energy demand without long-term radioactive waste and greenhouse gas emissions has never been greater. The efforts of thousands of researchers, scientists, and engineers are being employed in a huge international framework to build a machine that can finally show that fusion can be a net producer of energy. In addition to becoming the first fusion experiment in history to produce net energy and demonstrate the integrated operation of technologies for a fusion power plant, ITER (International Thermonuclear Experimental Reactor) will provide a unique opportunity to test in-vessel tritium breeding blankets in a real fusion environment. The focus of this work is on ceramic tritium breeding technology in pebble bed configuration and understanding the thermomechanical interactions evolution during operation.

1.1. Background

1.1.1. Nuclear Fusion and Tritium self-sufficiency

Due to its high energy yield and reaction cross-section, the fusion reaction of Deuterium and Tritium is considered as one of the most promising options for near-term fusion power generation.

$$D + T \longrightarrow {}^{4}He + n + 17.6\ MeV \qquad (1.1)$$

Deuterium is a stable hydrogen isotope with an abundance of 1 out of every 6500 atoms in seawater, which implies virtually limitless resources given the amount of water in the world's oceans. Tritium, on the other hand, is an unstable nucleus with a half-life of 12.3 years under β-particle emission with negligible natural abundance. As a result, the feasibility of achieving sustainable fusion power depends on the availability of tritium. Therefore, tritium breeding blanket is an integral part of a fusion reactor where tritium is bred in-situ to sustain the DT fuel cycle using the following reactions:

$$n + {}^{7}Li \longrightarrow n + {}^{4}He + T - 2.47\ MeV \tag{1.2}$$

$$n + {}^{6}Li \longrightarrow {}^{4}He + T + 4.78\ MeV \tag{1.3}$$

Natural lithium contains 7.42% ^{6}Li and 92.58% ^{7}Li. However, ^{6}Li has a very high neutron capture cross-section, and its density can be raised from 7.42% to higher values through isotopic enrichment. To obtain a closed DT fuel cycle, the rate of tritium production must balance the rate of consumption while accounting for decay and losses due to plant outages and scheduled maintenance. The typical net tritium breeding ratios (TBRs) needed to achieve 'tritium self-sufficiency' are about 1.05 to 1.1.

1.1.2. Solid breeder blankets for fusion reactors

In addition to serving as the primary thermal conversion system and an effective shield for reactor components, the fusion reactor blanket satisfies the main goal of tritium breeding for a sustained DT fusion reaction. After studying many solid lithium materials as potential candidates for tritium generation, the fusion community has come to realize that the lithium-based ceramic oxides are the most promising tritium breeding materials for fusion reactor solid breeder blankets. This conclusion is based on the premise that lithiated cermaics have many desirable characteristics including, but not limited to: high Li density, high melting point, good tritium release, desirable neutronics and irradiation characteristics, good thermomechanical properties under severe temperature environment, good thermal stability and chemical inertness.

As a result of extensive research endeavors, examination and material characterization of optimum ceramic breeder candidates since the 1970s, almost all recent solid breeder engineering designs have converged toward liquid-cooled pebble beds of lithium ceramics. The advantages of a ceramic breeder pebble bed configuration include: ease of assembly into complex geometries, ease of tritium extraction via the helium purge gas through interstitial porous networks, insensitivity to the large magnetic fields confining the plasma, and low chance of thermal cracking due to the small temperature gradients across each pebble.

A typical solid breeder module consists of a breeding volume that is subdivided into several alternating layers of neutron multiplication material (e.g. beryllium) and tritium breeding material (e.g. Li2TiO3 or Li4SiO4) in the form of pebbles (spherical particles). The pebbles are filled in

containment structures of a reduced-activation ferritic steel and the layers are separated by plates with internal channels for flowing liquid coolant. The coolant of choice is typically high pressure helium, though some designs incorporate pressurized water. The heat generated in the tritium breeding modules gets extracted by the coolant, which proceeds into a standard electricity production cycle. After tritium is generated inside the ceramic it gets ultimately picked up by a low-pressure, slow-moving Helium purge gas and extracted in the closed loop fuel cycle. A sketch of a typical ceramic breeder blanket depicting all the features described above is presented in Figure 1.1.

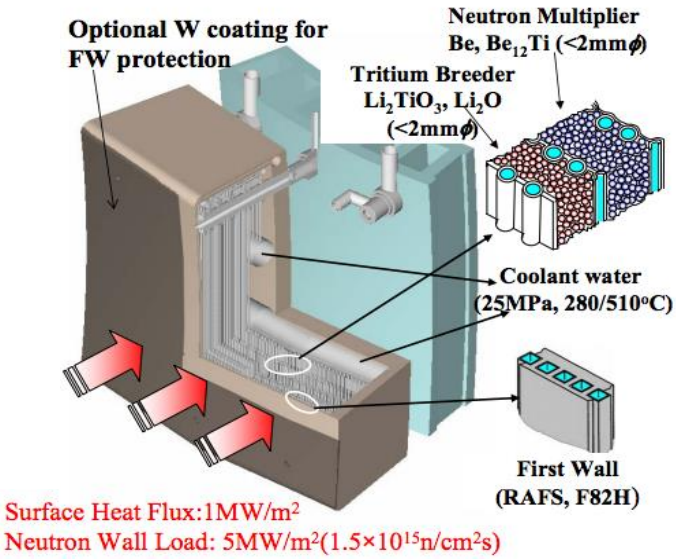

Figure 1.1 Example of typical ceramic breeder blanket components[1]

1.2. Motivation

The goal of this research is to explore methods for simulating volumetric heating, and to investigate the thermo-mechanical behavior of ceramic breeder pebble bed blankets in the presence of volumetric heating and temperature gradients representative of the fusion nuclear environment. The research involves experiments, modelling and analysis. The motivation of this work is elucidated below.

Current ceramic breeder blanket designs consist of alternating layers of lithium ceramic material, e.g. Li_2TiO_3, and the neutron multiplier beryllium, Be, both in the form of pebble beds. During the course of blanket operation, breeding blankets will experience high volumetric heating as deposited by high energy neutrons that are carrying away approximately 80% of the fusion reaction energy in addition to heating from secondary gamma rays. Heat deposited in breeders must be transported through pebble bed regions into the walls of containing structures, then ultimately into the coolant fluid via various mechanisms, such as inter-particle contact conduction, inter-particle radiation, convection with the helium purge gas, and interfacial particle-wall contact conduction. The heat deposition and active cooling in the narrow breeder cells result in significantly steep temperature gradients spanning the range of typically 400 to 850 °C within a 2 cm wide breeder unit. Due to the strong temperature dependence of the pebbles' thermo-physical properties, in addition to the differential thermal expansion between the pebbles and the confining coolant structure, complex thermally-induced stresses arise in the pebble bed causing different modes of deformation in the various temperature zones.

Stresses resulting from thermal expansion under cyclic loading can not only cause pebbles breakage, but also significant unrecoverable rearrangement of the packing structure. This so-called plastic rearrangement of pebble bed may have substantial consequences on the ability of the pebbles to maintain contact with the containing structure and routes for heat extraction due to gap formation and/or contact area reduction between pebble volumes and coolant walls. As a result, the average temperature of the pebble bed may rise above the sintering limit and have a negative impact on Tritium release. In addition to plasticity, thermal creep occurs in the hot regions of the bed where the contact areas between the pebbles start to increase with time under high stresses and temperatures. This behavior causes relaxation of bed stresses, and therefore further reduction in creep strain rate. Additionally, it improves the local thermal conductivity at the creep-compacted regions which reduces the peak temperatures and strain rate even more until saturation, which counteracts the effects of plasticity. However, due to lack of experimental data that incorporates such multiple-effects interaction, it is unclear whether the combined effect of plasticity and creep under reactor-relevant loading conditions will either enable the pebble bed to reach an acceptable self-regulating state, or continue to fluctuate outside suitable temperature limits and significantly deteriorate the heat transfer efficiency and tritium release. Thus, studying the isolated thermal and mechanical effects is not sufficient to predict pebble bed behavior. It is the coupling and interdependence between the thermal and mechanical fields, as well as the synergistic effects between the various modes of deformation that is key to fully understanding and predicting the pebble bed behavior in a realistic fusion environment.

The focus of this work is to use a combination of first-of-a-kind experiments and modeling efforts to answer the key questions pertaining to ceramic breeder pebble beds prototypical operation. Those key questions include:

(1) What is the result of the combination of multiple thermo-mechanical effects occurring simultaneously? Which effects will dominate?

(2) How many thermal cycles/time does it take to reach saturation levels?

(3) Does the self-regulating/saturated state fall within the pebble bed's temperature and stress design window and structural material limit?

(4) What constitutes failure? Pebble sintering, crushing, thermal runaway?

(5) Can a control mechanism be utilized, such as pre-compaction or pre-conditioning the bed to optimize the initial configuration to stay within design margins?

Consequently, recreating the fusion reactor temperature conditions, in addition to using innovative techniques to study the underlying thermo-mechanics are crucial steps in advancing the scientific understanding of the stability and operation of solid breeder blankets and potentially exploring control mechanisms and optimum initial packing configurations to maintain the temperature limits within the acceptable window dictated by tritium release characteristics and heat extraction efficiencies.

The uncertainty in constitutive modeling of pebble bed effective properties is common to engineering situations where multi-effect, integrated phenomena dominate. In such cases, a scientific framework is required where experiments and modeling advance from separate effects up to multiple-effect and partially-integrated studies with carefully designed experimental facilities. As parts of the effort of advancing toward multi-effect facilities, several experimental campaigns have been carried out previously in several European institutes. Unfortunately, all of the campaigns thus far have suffered from critical shortfalls which severely hamstringed their scientific impact. At present, no critical multiple-effect experimental data has been reported.

Nevertheless, multiple-effect experimental investigations and validation to FEM models remains a critical step toward reliable predictions of breeder pebble bed thermo-mechanics performance and must occur.

Several attempts have been made in the past for establishing multiple-effects experiments and many had critical shortcomings. Thus a significant effort has gone into pre-experimental analysis before constructing our laboratory-scale experiment that can recreate fusion-relevant synergistic multiple effects/multiple interactions phenomena and provide data for modeling validation. The experimental campaign at UCLA has been given the title of ThErmo-mechanical SOlid breeder Multiple-Effects eXperiment (TESOMEX). TESOMEX is expected to be the first out-of-pile experiment to simulate prototypical volumetric nuclear heating profile and employ state-of-the-art instrumentation techniques to study the associated thermal and mechanical interactions within a solid breeder cell.

Chapter 2

2. Literature Review

The complexity of the problem of understanding the thermomechanical behavior of ceramic breeder pebble beds lies in understanding how the fusion environment loading conditions affect the various properties of the pebbles assemblage. Under cyclic nuclear loading, the pebbles experience severe transient temperature gradients that affect the thermal and mechanical behavior of the pebbles, both directly and indirectly. Some of the important pebble bed properties that have to be considered are: the packing fraction, the effective thermal conductivity of the bed (i.e. the combined thermal conductivity of the pebbles and that of the purge gas), and the coefficient of thermal expansion of the pebbles. These properties have been investigated using carefully designed experiments for material characterization. Additionally, mock-up experiments that mimic the boundary conditions and geometries of fusion blankets were conducted in several research institutes accompanied with modeling efforts with the aim of strengthening the predictive capabilities applied to ceramic breeders operation.

2.1. Ceramic breeder pebble beds thermomechanics

Several experimental efforts have been carried out in the past with the aim of characterizing the thermomechanical behavior of pebble beds. Those experiments addressed the problem on two levels: the single pebble level, and the overall pebble bed level. On the single pebble level, parameters of interest relate to properties such as the bulk material thermal conductivity, and the average mechanical strength of a single pebble. The latter has been studied using crush load tests.

Knitter et al. and roux et al. showed that the crush loads of 0.5-mm diameter Li4SiO4 and 1-mm diameter Li2TiO3 pebbles studied for the European HCPB project are in the range of 4–5 and 35–50 N, respectively.[2]

Since the effective pebble bed properties cannot be directly deduced from single-pebble testing or base material properties, special experiments that mimic the conditions and dimensions of the breeder unit are required. The main control parameter is the pebble bed packing factor, which is the ratio between the volume of pebbles to that of the container's cavity. Many parameters influence the packing factor, such as the pebble diameter, shape, and surface roughness, in addition to the filling procedure and the dimensions of the container. Ideally, a larger packing factor is more desirable due to its impact on bed stability and effective thermal conductivity. In order to characterize the mechanical behavior of the pebble beds, Reimann et al. used Uniaxial Compression Tests (UCTs).[3,4,5]

In UCTs, the pebbles are filled to the prototypical packing factors in cylindrical cavities of carefully chosen dimensions to rule out the effect of friction. A piston applies a compressive force on the bed while the deformation is being recorded. From the stress-strain measurements of the loading and unloading cycles, the pebble bed's modulus of deformation is deduced.

The common mechanical response features observed in UCTs are:

- Nonlinear elasticity: the bed stiffens as the compressive loads increase, yet softens at higher temperatures for the same applied pressure, as shown in Figure 2.1.
- Irreversible bed deformation caused by pebble rearrangements and inter-particle plastic strains.
- Thermal creep deformation at constant load and high temperatures.

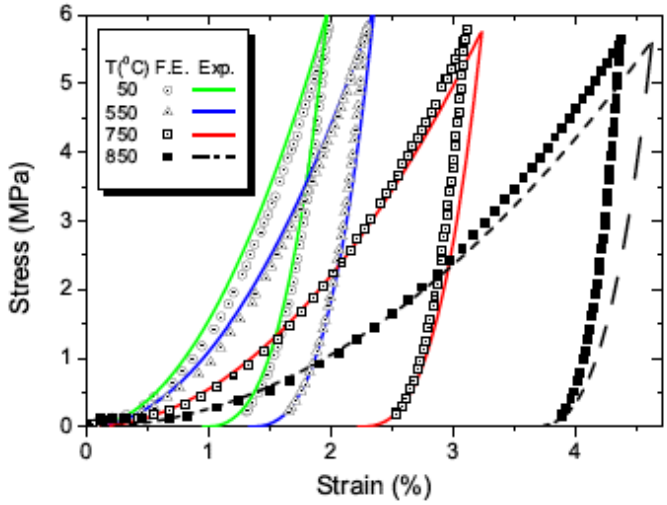

Figure 2.1 Example of uniaxial compression testing results compared with predictions from material constitutive equations for lithium orthosilicate pebble beds at different temperatures.[6]

It is evident in Figure 2.2 that the amount of plastic rearrangement is significantly reduced after the first loading-unloading cycle. This implies that this phenomenon can be avoided by pre-loading the pebble bed prior to operation.

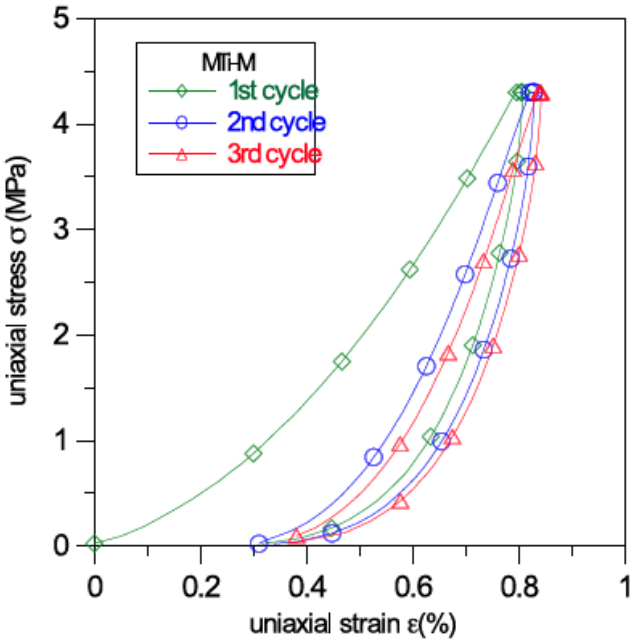

Figure 2.2 Example of uniaxial compression testing results for lithium metatitanate pebble bed.[7]

In order to quantify the expected stress levels induced by the confined expansion of the pebbles, further experiments have been carried out to characterize the thermal expansion coefficient. Thermal cycling experiments with 2 mm Li2TiO3 pebble beds between 100 and 700 1°C with a small load of 0.1 MPa were performed. The result was that the average thermal expansion coefficient is 78% of the value for the bulk material.[8]

UCT creep experiments have shown that thermal creep deformation becomes significant at temperatures greater than 650 C. In those tests, the pressure is kept constant for different bed temperatures for extended periods as the bed deformation is recorded. This phenomenon occurs due to the increase in inter-pebbles contact area with time at high temperatures, which induces a stress-release mechanism that can alleviate the thermal expansion and irradiation stress build-up. Correlations of the form $\varepsilon_{cr} = A(T)\sigma^m t^n$ were proposed by Reimann et al.[9,10,11] for different

materials. The strong dependence of creep strain rate on temperature and stress is clear from the magnitude and steepness of the curves shown in Figure 2.3.

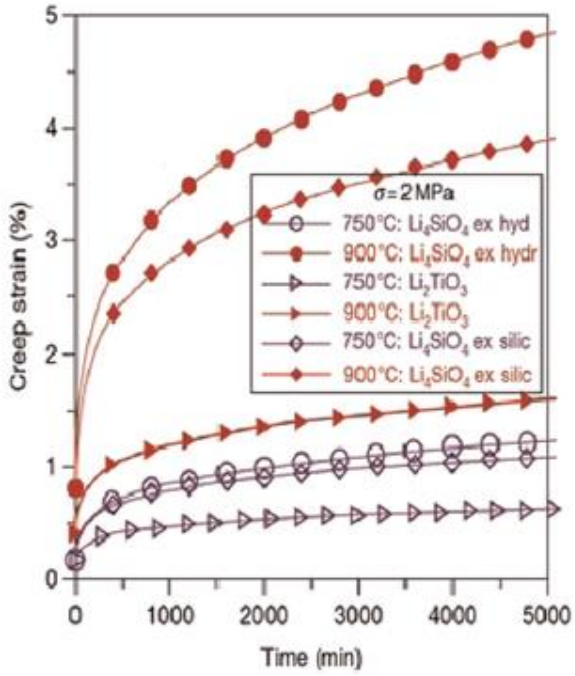

Figure 2.3 Thermal Creep strain curves as a function of temperature and stress for orthosilicate pebbles.

An important aspect to note in pebble bed thermomechanical behavior is that the thermal properties such as the effective thermal conductivity, K_{eff} and interface conductance, h, are not only affected by the average bed temperature, but also by the mechanical properties and compressive state of the bed.[19,31] This feature makes it crucial to model the coupled interaction between the mechanical and thermal fields and their evolution and response to external transient excitation.

2.2. Modeling approaches

There are different types of models to describe the behavior of pebble beds. Similar to Geomechanics models used to simulate the behavior of sand and rocks, pebble beds can be modeled by either continuum approach using Finite Element codes or discrete element method. The models are generally validated against available experimental data such as the UCTs. Both modeling techniques have their advantages and limitations as discussed below, yet their complimentary nature stemming from analyzing microscopic pebble-pebble interactions (DEM) and macroscopic pebble bed behavior (FEM) side-by-side provides a deeper understanding of the overall bed thermomechanical behavior.

2.2.1 Continuum mechanics and Finite Element Analysis approach

Granular materials are often modeled as fictitious continuous media using experimentally derived constitutive equations and effective properties in the framework of Finite Element Method (FEM). It is worth mentioning that the validity of using a continuum modeling approach lies in satisfying the condition that the pebble size is small compared to the dimensions of the pebble bed. Using the suitable phenomenological models, the continuum material can undergo elastic deformations, plastic volume compaction and pressure-dependent shear failure.

Two main phenomenological modeling campaigns developed among institutions include: (1) A non-linear elastic model combined with a modified Drucker-Prager-Cap theory for plasticity[12,13]; and (2) A hyper-porous non-linear elastic model and a Gurson model for the plastic portion.[14,15,16] Together with advancing the modeling techniques, several large scale pebble bed thermomechanics experiments were conducted. These experiments aimed to solidify the understanding of thermomechanical characteristics of ceramic breeder pebble beds, and provide

reliable data for benchmarking the developed models. The majority of work done on modeling the pebble beds in the FEM framework can be found in literature.[13,14,15,17,18,19,20]

Even though the continuum approach offers reasonable predictions, it still has shortcomings. For example, it overestimates tensile forces that do not exist in reality under a tensile free granular material assemblage. Moreover, it lacks the ability of modeling the resettling and rearrangement of the individual pebbles under the forces of gravity during thermal cycling and in the event of gap generation. This may have an impact on the accuracy of simulating the appropriate modes of heat transfer at the pebble bed/wall interface. For that reason, DEM has to be implemented in parallel to FEM in order to capture the microscopic effects.

2.2.2 Discrete Elements Method

As the packing structure evolves in time, due to the aforementioned thermomechanical effects, it becomes more important to model the ceramic breeders from the individual pebbles perspective. The Discrete Element Method (DEM) proposed by[21] to study granular materials through the interaction between individual particles has been shown to be a promising technique. The first DEM application was carried out at UCLA to study the micro-mechanical aspects of cyclic thermal loads on the relaxation of stress in pebble beds for fusion reactors[22,23]. Figure 2.4 shows the stress–strain relations for three cycles of a pebble bed with an initial packing factor of 60.3%. The pebble bed becomes stiffer with increasing the number of cycles.

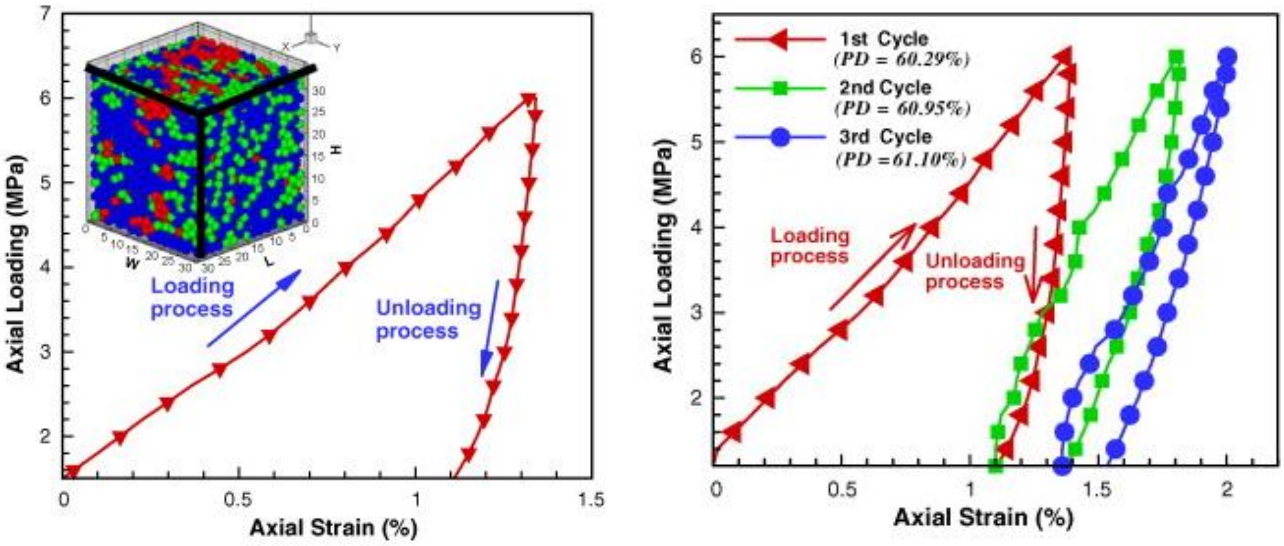

Figure 2.4. Stress–strain behavior of granular materials in (a) a rectangular box under uniaxial compaction and (b) packing density effect[24].

Following UCLA work, researchers at Karlsruhe Institute of Technology (KIT) continued DEM efforts, and started to improve upon the initial studies begun at UCLA. Uniaxial compression test, UCTs were used first by both groups to study the influence of microscopic effects on a characteristic macroscopic pebble bed property. Gan et al. showed that the average coordination number, average normal contact force and the maximum normal contact force in the assembly has a unique functional relation (nonlinear, linear and linear, respectively) with the hydrostatic pressure or the applied pressure independent of the packing factor. These functional relations may be used as master curves for the micro-macro correspondence in the pebble bed thermomechanics studies.[25]

Recently, the influence of pebble failure on pebble bed thermal conductivity was first assessed, using strongly simplifying assumptions.[26] A significant decrease of thermal conductivity on the number of failed pebbles was found.

Despite the shortcomings of a continuum approach, it is the only option which currently

allows treatment of the pebble beds with standard finite element modeling (FEM) that can be scaled up to describe the overall thermomechanics of larger blanket components.

Nonetheless, DEM codes have achieved significant progress in the last years in describing micro-scale effects. Therefore, a combination of discrete and continuum approaches capturing both micro-scale material details and modeling capability at the system level will be the best option for the near future.

2.3. Mock-up Experiments and benchmark activities

In-pile and out-of-pile breeder mock-up experiments have been conducted in various fusion research institutes to evaluate the thermomechanical behavior of ceramic breeder concepts under fusion relevant conditions. A summary of the main accomplishments is presented below.

2.3.1 HELICA/HEXCALIBER Experimental campaigns and comparison with current FEM codes

The constitutive equations used in FEM codes were derived from UCTs where one parameter was varied and its effects were isolated and studied for material characterization. Although this type of experiments is useful for constitutive laws derivation and material properties characterization, it does not represent the real fusion environment where the temperature fields and mechanical loading will be far from uniform. For that reason, several out-of-pile experiments were launched by the HE-FUS 3 facility at ENEA Brasimone. The experiments investigated the thermomechanical behavior of pebble beds within more representative geometries and loading conditions to those of current breeder designs. These include the medium-scale mock-up exercises of HELICA (HE-FUS3 Lithium Cassette) and HEXCALIBER (HE-FUS3 Experimental Cassette

of Lithium Beryllium Pebble Beds).[16,27] For those experiments, the pebble layers are heated by electric heaters, and temperature and displacement were measured.

2.3.1.1 Forschungszentrum Karlsruhe (FZK) benchmarking

FZK validated their FEM code against the experimental data collected from HELICA, and reported simulation data for HEXCALIBER absent experimental validation as of today.[6,18] The experimental loading plan for HELICA was to undergo six hourly-applied thermal ramps followed by active Helium cooling. The process was repeated several times after cool down and data was collected for model validation. Two cycles of the HELICA test and an example of the calculated results and experimental data are shown in Figure 2.5 and Figure 2.6. Temperature histories at 100 mm from the first wall during a loading-unloading cycle are presented in Figure 2.5. Due to the enormous amount of computational resources required to model the full 3D setup of HELICA and HEXCALIBER, the FZK model approximates the problem to a 2-dimensional form with an average inlet/outlet coolant temperature. Even with the 2D simplification of the code, the model temperature results follow the experimental measurements for the temperature increase and cool down fairly closely. Figure 2.6 also demonstrates a strong agreement between the measured displacements and model results throughout the thermal cycle.

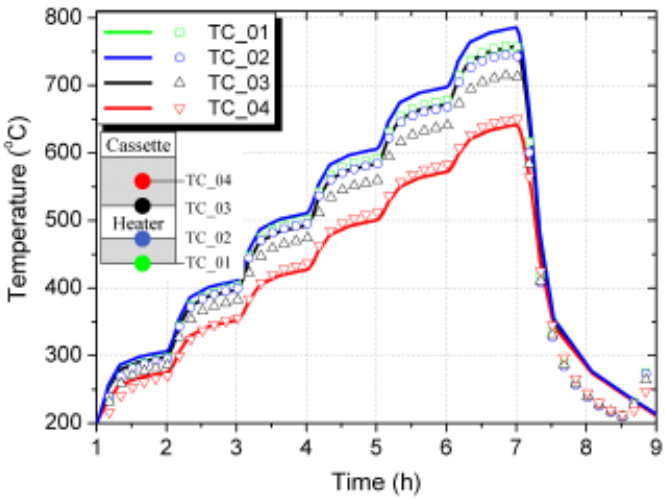

Figure 2.5: Results of the FZK benchmarking with HELICA[18] showing temperature variations with time during a loading cycle (T in ◦C) at 100 mm from FW.

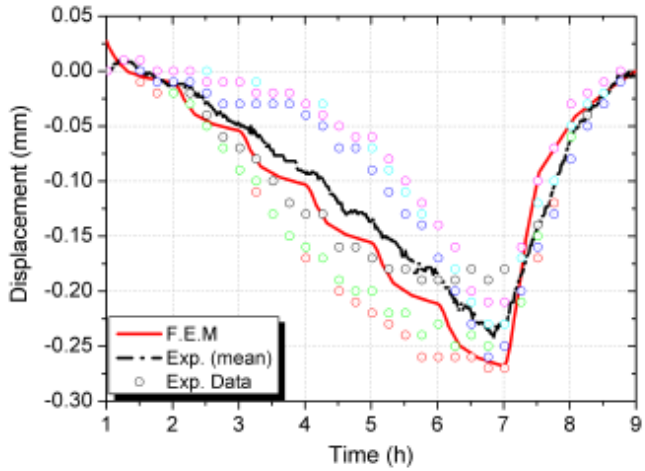

Figure 2.6: Results of the FZK benchmarking with HELICA[18] showing a comparison of displacements (in mm) in HELICA between calculated and measured LVDT values.

Some of the FZK results observations/limitations include: (i) the temperature profile at one cross-section is not representative of the full picture of the temperature evolution given the 3D

nature of the problem dictated by the volumetric heating and active cooling. (ii) the maximum stresses predicted by the model exceed the fracturing limit of the orthosilicate pebbles and further verification of more complete models is required to reach more conclusive results; (iii) gap generation at the bed-wall interface on the order of a pebble diameter was detected.

It is clear from Figure 2.5 that the temperature calculations deviate from the measured values during the cooling cycle. This can be attributed to the gap formation that occurs at the interface due to the pebbles rearrangement during unloading and fragmentation at high stress levels. This discrepancy in the modeling technique utilized is inherent in FEM continuum approach since the microscopic effects can only be revealed via DEM simulations.

2.3.1.2 DIN model benchmarking

The primary improvement of the DIN model of FZK is the 3D modeling capability. DIN model has been validated against both experimental campaigns HELICA and HEXCALIBER as shown in Figure 2.7 and 2.8. The results were reported over a 6-hour heater ramp up period for HELICA. Slightly better agreement of the temperature evolution than that of FZK was found, perhaps due to the inclusion of 3D effects. Due to the breakage of several heaters during HEXCALIBER tests, unfortunately, limited data was presented. However, the temperature results seem to agree with the model predictions to a great extent. Mechanical results were not reported by the ENEA Brasimone team. Only temperature variations as seen in Figure 2.8 were published.

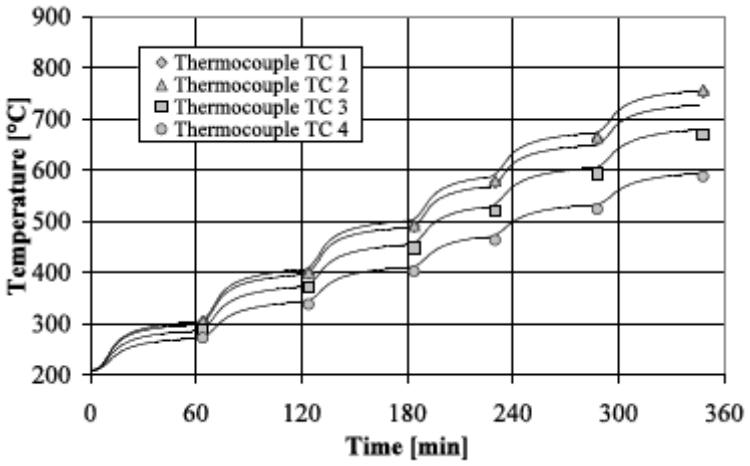

Figure 2.7: Exemplary results of the DIN benchmarking with HELICA: Temperature variations with time during a loading cycle at 100 mm from FW.[14]

Several takeaways from the DIN model benchmarking are: (i) 3D effects in predicting the temperature evolution in ceramic breeders are necessary and can significantly improve the predictive capabilities of FEM modeling efforts. (ii) since the heaters broke at an early stage of the HEXCALIBER experiment, high temperatures were not reached, and therefore, no creep model validation was provided. (iii) the DIN model predicted compressive state in the pebble bed at all times with no gap formations, which disagrees with the FZK model results.

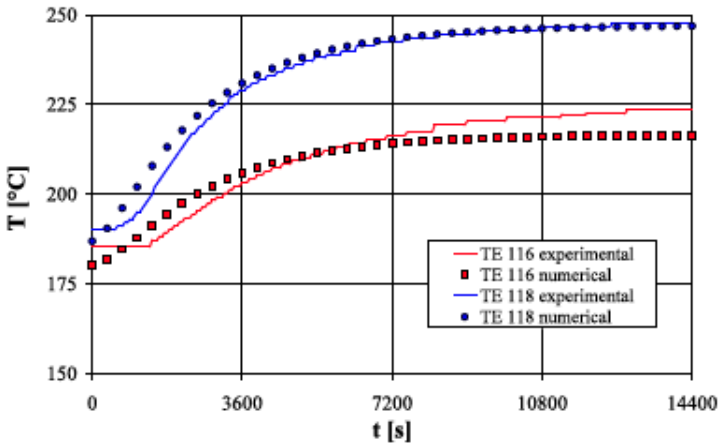

Figure 2.8: Exemplary results of the DIN benchmarking with HEXCALIBER : Temperature

variations with time during a loading cycle within the first lithium-orthosilicate cell.[15]

In summary, the typical sequential thermomechanical FEM model starts with calculating the temperature distributions based on the volumetric heating loads and cooling conditions. After that, the mechanical results are computed based on the effective bed properties. Since the thermal properties of the bed, K and h, depend on the compressive state and deformation of the pebble bed, an iterative fully coupled thermomechanical solution is required to obtain relevant results. Even though the most mature FEM models have had their results validated against experiments, much ambiguity remains and significant efforts are needed to overcome the limitations of FEM in reproducing the individual pebbles behavior. Moreover, the sources of inconsistencies between the two models have to be discovered before proceeding with additional benchmarking activities for future experiments.

2.3.2 Post-irradiation experiments at Petten

The pebble bed assemblies (PBA) experiment was designed to test the pebble bed thermomechanical behavior under fusion relevant neutron irradiation and thermomechanical loads.[28] The setup consisted of are four test elements; each resembling a small-scale mock-up of a HCPB TBM with a ceramic breeder pebble bed sandwiched between two beryllium pebble beds. The compaction procedure consisted of a subsequent loading of the pressure plate of the total assembly to 3 MPa. During progressive irradiation, temperatures are recorded at several locations in the ceramic breeder bed as well as other critical positions. Changes in the pebble beds and their characteristics are examined both in-pile by neutron radiography and out-of-pile by e.g. SEM during post-irradiation examination (PIE). Comparing the temperature in the center of the ceramic

breeder pebble bed during later cycles and earlier cycles revealed a decrease in temperature for the exact same environmental conditions.

As a result of creep compaction, the pebble bed experiences more-developed inter-pebble conduction paths. The effective thermal conductivity for a creep-compacted ceramic pebble bed is thus expected to be higher than a standard ceramic pebble bed. This phenomenon results in lower bed temperatures, which is precisely what was observed in the experiment over the course of the cycling. Various microscopy diagnostic techniques were used to study the deformation state of the pebble beds such as: signs of creep compaction and sintering, formation of gas gaps between the pebble beds and structural materials, and the interaction layers between eurofer-ceramic and eurofer-beryllium. Sintering of the lithium titanite and significant fracturing of the lithium orthosilicate pebbles were observed. Nonetheless, despite the visible deformation the pebble beds performed reliably during the course of operation and irradiation.

2.4. Objectives and scope of work

Within the research thrust of the solid breeder group at UCLA exists an overall objective for predictive capability for thermo-mechanical responses of pebble beds in ceramic breeders under reactor operating conditions. To that end, significant progress was made in characterizing mechanical properties for Li_2TiO_3 pebble beds including non-linear elastic modulus, hardening law, creep rate, and thermal expansion coefficient. Constitutive equations describing these properties have been derived from experimental measurements, and were used in FEM ANSYS code to predict breeder layer thermal-stress/strain states. The experiments and their associated constitutive equations are necessarily derived with single effect tests, where one parameter is

varied and its effects isolated. However, in practical reactor conditions there exist synergistic effects which cannot be synthesized by these single effects and phenomena arising from their interactions are yet to be discovered.

A major effort in this work is the launch of a multiple-effect breeder and structural material thermo-mechanic interaction experiment with a companion effort on FEM modeling enhancement and validation. The experimental activity will help uncover any potential new effects arising from, *e.g.*, mechanical interactions between regions where time dependent creep deformation dominates and regions where no creep deformation is expected, and understanding the impact of its evolution on heat transport and temperatures. In order to simulate the conditions inside a solid breeder, the feasibility of an experimental technique to simulate the nuclear heating profiles in a solid breeder without noticeable disruption to thermo-mechanical responses of the pebble bed must be established. Moreover, non-disruptive diagnostic/instrumentation techniques to measure the pebble bed properties must be explored and identified.

The overall objective is to develop a better understanding and predictive capability for the complex thermo-mechanical interactions of pebble beds in ceramic breeders under practical reactor operating conditions by:

1. Recreating prototypical breeder unit thermal behavior, in terms of temperature profiles and magnitudes under relevant fusion blanket operating conditions.

2. Studying the interdependent spatially and temporally varying thermo-mechanical interactions.

Scope of work:

1. Establish and validate the practicality of a volumetric heating simulation technique for representative thermo-mechanics study.

2. Evaluate the pebble bed thermo-mechanics in prototypical configuration and temperature profiles using adequate non-intrusive in-situ diagnostic tools.

3. Analyze the effect of optimizing the packing density (e.g. due to pre-conditioning) on pebble bed thermo-mechanical stability and evolution.

4. Refine, and benchmark existing thermo-mechanical Finite Element Method (FEM) codes.

Chapter 3

3. Precursor Experiments & Investigation

In order to better describe and predict the interaction between ceramic breeder and beryllium pebble beds and the structural material, the characteristic properties of these pebble beds under not only relevant temperature magnitudes, but also the expected temperature gradients must be known. Previous studies have shown that during the first stress increase, irreversible rearrangement of pebbles is the dominant mode of bed deformation.[4] For subsequent stress increases/decreases, pebble bed stress-strain slopes are steeper and closer to that of the first stress decrease, which indicates more prominent elastic deformation and stiffer bed mechanical behavior. Therefore, the magnitude of thermal stresses induced by the imposed temperature gradient is expected to greatly depend on the initial bed stress state and packing configuration. Particularly, pebble beds will undergo more deformation/rearrangement under low initial packing fraction than beds that have experienced comparably higher initial compaction. To that end, pre-test mechanical compaction load, from here on referred to as 'pre-compaction', is considered as a design parameter in this study, where its effect on bed thermo-mechanical evolution will be analyzed.

The primary goal of the present investigation is to define an optimal initial pebble bed packing configuration in the attempt to minimize any significant in-pile thermo-mechanical deviations that may jeopardize the mechanical integrity of the pebbles assemblage and/or appreciably deteriorate heat transfer performance and tritium release. For that purpose, this work aims to: (1) quantify and analyze the stresses induced by the thermal expansion of the pebbles under prototypical temperature gradients and fixed mechanical boundary conditions, (2) study the effects of thermal

cycling, mechanical pre-compaction, and thermal creep/stress relaxation on the evolution of pebble bed stress levels, and (3) further develop Finite Element Method (FEM) codes to capture all the above-mentioned synergistic effects arising from reactor-relevant temperature distributions.

Two experiments have been executed in this study: (1) a temperature gradient experiment, where the pebble bed is subjected to fusion-relevant cyclic temperature gradients under fixed mechanical boundary; generated stresses are measured for different testing conditions and loading parameters, and (2) a stress relaxation test where the peak stresses measured in the previous experiment are used as initial loads on isothermal beds and allowed to relax to saturation levels under active creep temperatures.

3.1. Test apparatus and experimental campaigns

This section summarizes the experimental methodology and objectives, in addition to providing a basic description of the layout and procedure.

3.1.1 Test apparatus & pebble bed characteristics

The experiments were carried out in a modified uniaxial compression test (UCT) facility with a hydraulic press and a three-zone electrical furnace at UCLA. The modified setup incorporates an active cooling mechanism for pistons. Pre-analysis was performed to define the piston coolant operating conditions in order to limit the upper piston thermal expansion as well as to decrease the thermal cycling time. A Paratherm (thermal-fluid) temperature control loop was set-up and coolant flow passages were machined in the solid pistons allowing the Paratherm to maintain the pistons at the desired temperatures. An auxiliary heater on the upper test frame piston and coolant in lower piston together allow a temperature gradient of about 320 °C across the sample.

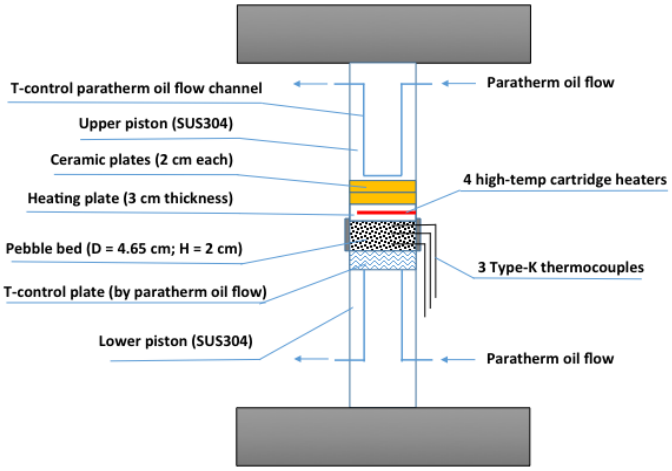

Figure 3.1 Updated UCT test stand schematic with cooled piston rods and top heater for cyclic temperature gradient tests.

The pebble bed temperatures were measured by three fine-diameter thermocouples located in the top, middle, and bottom bed regions. The setup is shown schematically in Figure 3.1.

The breeder material tested in this study is lithium metatitanate (Li2TiO3) in the form of pebbles. The batch used in this study was fabricated using the slurry droplet wetting method, which the National Fusion Research Institute in Korea (NFRI) adopted in its mass-production process.[29] Table 3.1 shows characteristic values of the investigated pebbles.

It was previously demonstrated that UCTs should be performed with bed height to diameter ratio, H/D, less than unity in order to avoid container wall friction effects.[5] Additionally, to maintain the random packing of the pebbles in the bulk region of the bed, the bed diameter to pebble diameter ratio, D/d and H/d, have to be greater than 10. Therefore, the pebbles were filled in a cylindrical container with an inner diameter of D = 46.5 mm and a bed height of H = 20 mm, adhering to the recommended dimensions characteristic of blanket relevant shallow pebble beds.

TABLE 3.1.: Characteristics of investigated granular material

Type	**Assoc.**	**Pebble diameter (mm)**	**Grain size (μm)**	**Sint. Temp. T_s (°C)**	**Crush load (N)**
Li_2TiO_3	NFRI	1.03	10	1000	33

3.1.2 Temperature gradient test

The experiment primarily aims to quantify stresses generated by pebble beds due to prototypical solid breeder blanket temperature gradients and magnitudes under fixed mechanical boundaries. The experimental procedure was established to separate expansion of the piston-heater assembly from that of the pebble bed by heating the upper assembly to an equilibrium temperature before the heater makes contact with the pebble bed, and controlling the power to maintain a constant surface temperature boundary. The procedure defined below is to study pebble bed thermo-mechanics evolution for a fixed boundary configuration.

First, the bed is packed and vibrated to reach a packing fraction of 63% with the thermocouples installed in the designated positions in the bed (top, middle, and bottom regions), piston (at the mid-plane location), and heater. After applying a pre-compaction load, defined in Table 3.2, at room temperature for 5-10 minutes, the upper piston is separated from the bed, heaters energized, and brought to target steady-state temperature while the coolant circulates through the upper and lower pistons. Next, the piston is lowered to make contact with the pebble bed whereupon the crosshead location is fixed and recorded for use in subsequent thermal cycles to simulate the fixed mechanical boundary of the blanket coolant structure. To minimize heat losses,

the pistons are wrapped with insulation, and the furnace is closed during bed heat-up phase. Additionally, a LabVIEW feed-back loop controls the heater power level to maintain a constant heater surface temperature throughout the full experimental procedure. As the bed heats up from room temperature to the final gradient, bed temperatures and the thermally-induced forces are monitored until all values reach steady-state. Finally, the piston is retracted, heater remains energized, and the bed is actively cooled to the initial baseline temperature. The above procedure is then repeated for any subsequent thermal cycle with the upper piston brought down to the fixed crosshead height, as recorded from the first thermal cycle, rather than a target contact load.

3.1.3 Stress relaxation test

Past studies on stress relaxation revealed that for a bed temperature of 770°C, the uniaxial pressure drops to 25% of the initial value during only the first two hours.[5] However, pre-compaction effects were not considered in those studies. Therefore, this second experimental campaign aims to further investigate pebble bed stress state evolution under different creep-relevant temperatures, initial loads, and pre-compaction levels. The three-zone furnace, incorporated in the UCT test stand, is used to raise the bed temperature until reaching steady state, while the temperature controller is used to independently power each zone based on the continuously monitored bed thermocouples to guarantee uniformity. An initial load is applied, after which the bed volume is fixed while allowing the stresses to relax as creep deformation takes effect.

3.2. Experimental results & discussion

The results of both tests are presented in this section, followed by extensive analysis of the observed phenomena.

3.2.1 Temperature gradient test results

Five thermal cycles were carried out at four levels of pre-compaction and two bed temperature states. The experimental matrix, as well as the measured peak stress magnitudes for the first and last cycles are summarized in Table 3.2. The peak uniaxial stresses measured at the end of each thermal cycle were recorded for different pre-compaction levels to test effects of pre-compaction on the stability of generated stresses as the number of thermal cycles increased. Figure 3.2 shows that the reduction of initial peak stress is much more significant for lower pre-compaction. In other words, higher levels of pre-compaction show a more stable behavior during subsequent thermal cycling compared to lower pre-compaction levels. For the 0.1 MPa pre-compaction case, stresses diminished after the first cycle for the two bed temperature states tested, indicating a gap generation at the top of the pebble bed. In contrast, for the highest pre-compaction run of 3 MPa, generated stresses remained practically constant throughout the thermal cycling process. For the 1 MPa case, the stress magnitudes were larger than those for the 0.1 MPa case, but still deviated significantly from the initial cycle stress and continued to drop with cycling. For

the 2 MPa case, the stress level dropped to about half the initial value, but remained stable after the third cycle.

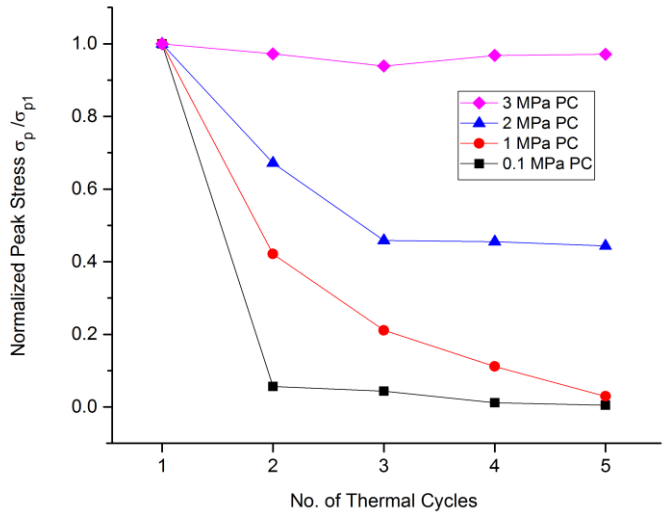

Figure 3.2. Thermally-induced peak stresses normalized by first cycle peak stress for different pre-compaction (PC) loads show higher pre-compaction lead to more stable stresses during thermal cycling.

TABLE 3.2 Temperature gradient test parameters and testing conditions

Initial packing fraction γ (%)	σ_{pc} **(MPa)**	**Meas. PC (µm)**	**Temperature diff.** [a] **ΔT (°C)**	σ_{p1}[b] **(MPa)**	σ_{p5} **(MPa)**
63.2	0.1	--	288 [450-162]	0.25	0.005
63.5	1	366	300 [457-157]	0.98	0.03
63.1	2	446	311 [474-163]	1.8	0.82
63.2	3	597	318 [477-159]	1.92	1.85
63.3	0.1	--	391 [659-268]	0.54	0.04
63.3	3	580	402 [657-255]	3.1	2.89

[a] Bed temp. difference at end of cycle [avg. top bed temperature – avg. bottom bed temperature]

[b] $\sigma_{pi} \rightarrow i^{th}$ thermal cycle peak stress.

3.2.2 Stress relaxation results

Figure 3.3 shows initially-applied stresses relaxing with time for different pre-compaction levels and uniform bed temperatures. A sudden drop in axial stress is observed for the high temperature cases (T > 650 °C) as soon as the bed's volume is fixed. For T = 650 °C, this drop seems to be less abrupt for pre-compacted beds, denoting a stiffer bed response. Nonetheless, after the initial steep drop phase, it is evident that the relaxation process is primarily governed by a relatively slower creep deformation, which saturates to stable levels after approximately the first 5 hours ($\sigma_{sat} \approx \sigma_{5hr}$). Since creep is thermally activated, temperature was, unsurprisingly, the

most sensitive parameter controlling the rate of stress decay. Thus, for the 750 °C case, stresses dropped faster and saturated slower than those for the 650 °C cases. For the highest temperature run of 850 °C, axial stress dropped from 4 MPa to 0.1 MPa in less than 4 hours. By comparing the two runs of initial stress of 4 MPa and 2 MPa at 750 °C, a slower rate of stress relaxation is

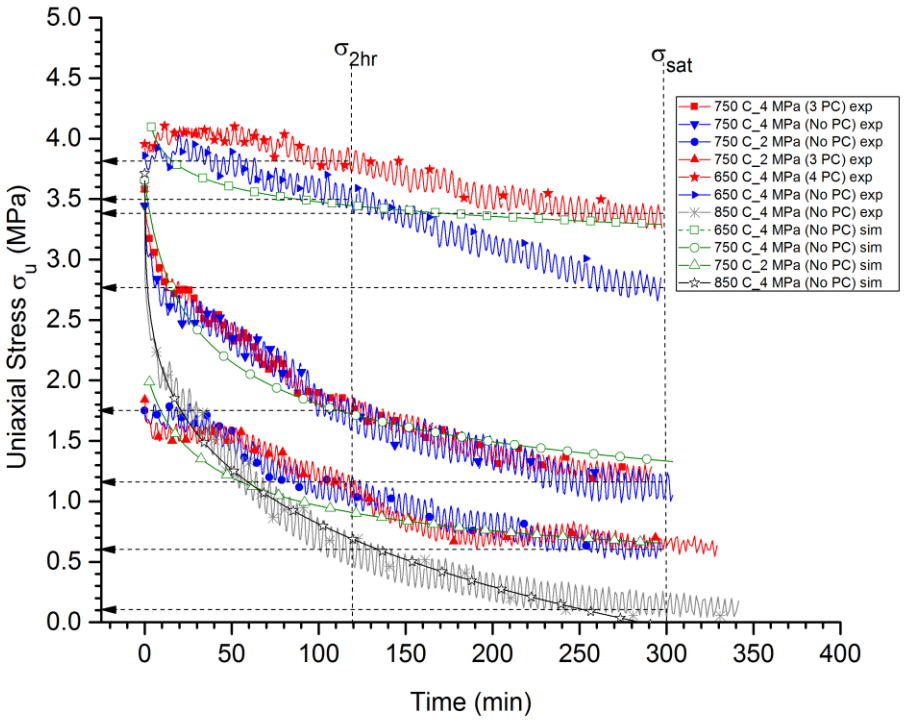

observed for the lower initial stress level.

Figure 3.3 Stress-release by thermal creep for different temperatures, initial loads, and pre-compaction (PC).

3.2.3 Discussion & analysis of results

The above results can be explained by analyzing the mechanisms of multiple effects/interactions of plastic deformation, thermal expansion, and creep in granular materials. Pebble beds irreversible or plastic deformation takes place mainly due to bed consolidation, which typically arises when the bed undergoes compressive stress states, causing pebbles to rearrange into denser packing configurations. This behavior prevents the bed from recovering to its initial configuration and increases its overall stiffness. It has been demonstrated experimentally as well as numerically that the highest levels of bed plastic deformation occur over the first few loading/unloading cycles, followed by mostly recoverable elastic strains for subsequent cycles[30] – provided that the applied/generated stress does not exceed the initial load, as demonstrated in Figure 3.4. Hence, the temperature gradient experiment runs where pre-compaction load was greater than the thermally-induced stress resulted in the most stable bed stress state with cycling.

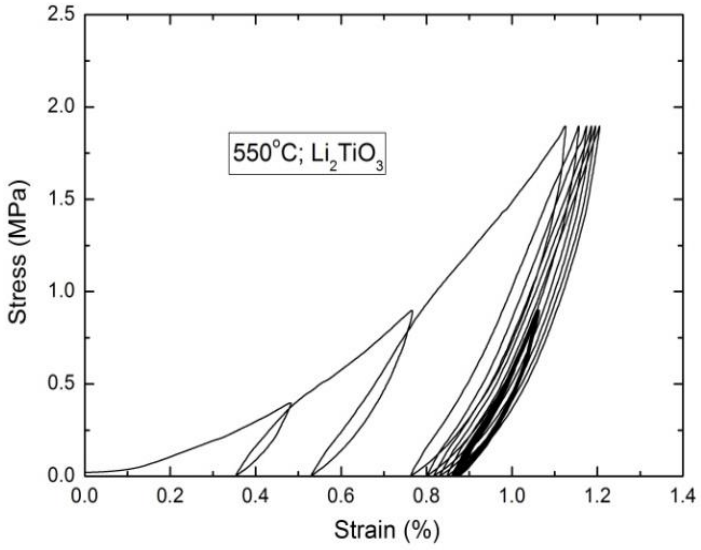

Figure 3.4. Pebble bed stress-strain curves of previous UCLA experiments illustrating initial bed plasticity, bed modulus stiffening, and consistent cyclic behavior below yield stresses[30].

Since the highest temperature reached in the first experimental campaign of 650 °C (below which no appreciable creep is observed) was only experienced by the few top layers of pebbles in the bed, the second campaign was designed to further assess the stress state stability at creep relevant temperatures. Generally, correlations that predict creep behavior in pebble beds strongly depend on the initial stress level and temperature; higher temperatures/stresses accelerate the strain rate, $\dot{\epsilon}_{v,cr}$, see Eq.(3). Additionally, interesting phenomenon was observed while analyzing the effect of pre-compaction on relaxation rates. In Figure 3.3, at 650 °C, the threshold temperature of noticeable stress release, no rapid initial stress drop was observed and the stress relaxation saturated faster than that of the no pre-compaction case. On the other hand, at 750 °C and above, temperature was the dominant parameter governing the rate of stress relaxation, and the effect of pre-compaction was much less apparent.

To understand this behavior, one must carefully examine the mechanisms of permanent deformation in materials with regards to plasticity and creep. At stress levels below the current elastic limit, there is not enough energy available for the pebbles to rearrange themselves irreversibly. Since pre-compaction enhances the bed's yield strength, a compacted bed will exhibit higher resistance to deformation for the same temperature. Nevertheless, elevated temperatures add thermal energy to the system, increasing the likelihood of permanent deformation. Therefore, at high enough temperatures, there is enough thermal energy available to induce creep and stress relaxation, even if the initial stress level is well below the yield strength of the material. During creep, the contact areas between the pebbles increase and initial gaps may close with compaction. This generates new contacts that transmit a fraction of the load and decreases the average stress per contact surface, resulting in slower strain rate with time[9]. Therefore, unlike creep tests where the experiments take days/weeks to reach saturation, the stress relaxation is expected to saturate faster since the strain rate depends on the current stress state, which is

constantly decreasing as more stress is released. This behavior is more relevant to fusion blankets since there will be no constant externally applied loads on the bed.

Although stress relaxation will aid in discharging pressure caused by thermal expansion and irradiation-induced swelling loads in the highest temperature bed zones, a subtle risk stems from its interaction with plasticity in the lower temperature regions. The temperature gradient cycling experiment demonstrated that, for the no pre-compaction cases, the bed pressure drops to practically zero and gaps form at the bed/structure interface after the first few cycles even for the higher temperature runs (RT→650°C). Furthermore, based on the stress relaxation tests, the stresses in the high temperature bed regions will also diminish to much lower levels over the first few hours of operation. Previously proposed and validated thermal models of bed-wall interfacial heat conductance as a function of mechanical stress and gap show strong dependence of the interface heat transfer coefficient HTC on the interface pressure for a fixed bed temperature[14,19,31,32]. Consequently, if a gap forms at the interface or if the pressure reduces to inadequately low levels with continuous thermal cycling and relaxation, the efficiency of heat extraction at the coolant structure walls can deteriorate, risking an increase in bed temperatures until greater expansion once again resumes stress levels; at which point sintering temperatures may be exceeded and tritium extraction is reduced. Therefore, the results suggest pre-compaction is needed to overcome major stress reductions with cycling in the lower temperature bed regions ($T < 650°C$), which is characteristic of the near-wall zone, while relying on a self-regulating stress release mechanism in the core region of the bed ($T > 650$ °C) to compensate for the higher thermally-induced stresses and irradiation-induced swelling loads. Moreover, the results also highlight the necessity for future multiple effect experiments on pebble beds in which the myriad modes of thermo-mechanical interaction predicted in solid breeders are all simultaneously active.

3.3. Summary

Two experimental campaigns were conducted at UCLA to serve as precursors to future efforts of analyzing the multiple effects/multiple interactions of the various phenomena that occur in a prototypical solid breeder fusion blanket. The temperature gradient thermal cycling experiment considered the combined effects of plastic deformation and thermal expansion under thermal cycling conditions, while the stress relaxation test examined the stability and evolution of bed stresses under creep/reactor relevant temperatures. Emphasis was laid upon understanding potential loss of thermal contact between the pebbles and the coolant structure as a result of the combined effect of stress relaxation and bed plastic deformation.

Pre-compaction was investigated as a design parameter and proved to have the following effects on the bed as a result of bypassing the substantial plastic deformation that normally occurs during the first few loading/unloading cycles: (1) artificially increasing the bed stiffness, and thereby raising the thermally-generated stresses to appropriate levels that maintain good interface contact conductance and pressure, (2) reducing the number of thermal cycles required to reach a state of stress saturation, and (3) mitigating sudden stress reductions in the transitional creep regions of the bed.

Efforts are currently underway to develop a 3D, fully-coupled thermo-mechanical volumetrically-heated, transient breeder cell model capable of simulating an adequate number of thermal cycles to reach stress-saturation levels. The model incorporates all previously validated single-effect material models, permitting preliminary analysis of many synergistic effects of a solid breeder in a typical fusion environment. Nevertheless, there is uncertainty in the predictive capability of FEM simulations until validation against multiple-effect experiments. Therefore, in order to reach more conclusive results, extensive experimental efforts are ongoing at UCLA to analyze the interaction of blanket relevant multiple effects with volumetric heating conditions.

Chapter 4

4.Multiple-Effects Experiments

Several attempts have been made in the past for establishing multiple-effects experiments and many had critical shortcomings. Thus a significant effort has gone into pre-experimental analysis before constructing our laboratory-scale experiment that can recreate fusion-relevant synergistic multiple effects/multiple interactions phenomena and provide data for modeling validation. The experimental campaign at UCLA has been given the title of ThErmo-mechanical SOlid breeder Multiple-Effects eXperiment (TESOMEX). TESOMEX is expected to be the first out-of-pile experiment to simulate prototypical volumetric nuclear heating profile and study the associated thermal and mechanical interactions within a solid breeder cell.

TESOMEX (ThErmo-mechanical SOlid breeder Multiple-Effects eXperiment) aims to create a fusion relevant environment in which the myriad modes of thermo-mechanical interaction predicted in solid breeders are all simultaneously active. The experimental campaign is divided into two subsequent design phases: proof of heating, and thermo-mechanical evolution analysis. The main goal of the first design iteration is to test the wire matrix heating scheme's ability to recreate temperature distributions characteristic of pebble bed volumetric heating. The second design iteration aims to: a) reproduce a more relevant thermo-mechanical behavior characteristic of the interaction between the pebbles and the structural material under prototypical temperature profiles. b) Benchmark the most up-to-date FEM models that can then be extrapolated to add more complexities.

4.1. Volumetric heating exploration

One of the possible bulk heating techniques is microwave heating. Microwaves are electromagnetic waves with wavelengths ranging from 1m to 1 mm (f=0.3 and 300 GHz). Microwave heating is a process whereby microwaves couple to materials which absorb the EM energy volumetrically and transform it into heat. This type of dielectric heating involves the heating of electrically insulating materials by dielectric loss; a changing electric field across the material causes heat dissipation as the molecules attempt to align with the continuously changing electric field. A ceramic material that exhibits dielectric heating when exposed to microwave is referred to as a susceptor. A material that allows the microwaves to pass through, is referred to as transparent; conversely, one that does not allow the microwaves to pass through is considered reflecting.

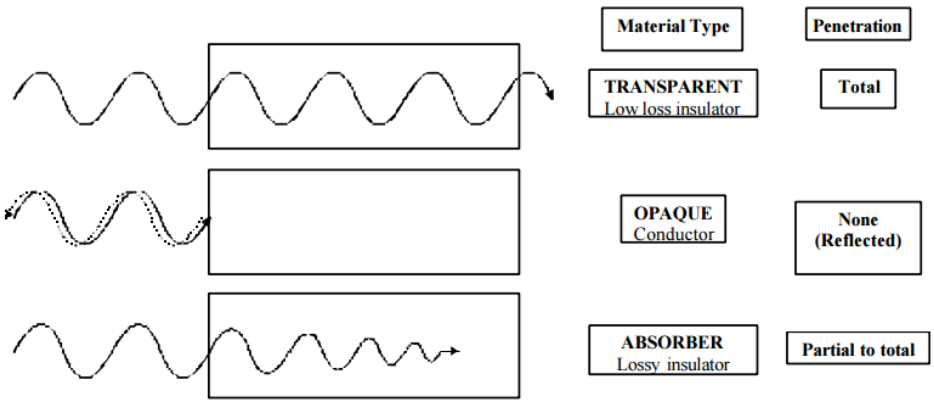

Figure 4.1 Illustration of microwaves penetration through different materials

The average microwave power deposited in the material is given as:

$$P_{av} = 2\pi f[\varepsilon_o \varepsilon''_{eff} E^2 + \mu_o \mu''_{eff} H^2]V \qquad (4.1)$$

Where:

f is frequency of microwave

ε''_{eff} , μ''_{eff}. are effective relative dielectric and magnetic loss factors respectively,

E and H are r.m.s. electric and magnetic fields of microwave within the material respectively,

and V is volume of the material.

From Equation (4.1) it is evident that the amount of microwave power deposited in a material depends on the frequency of the incident wave and the dielectric properties of the material. For example, 25 times more power can be dissipated in alumina at 28 GHz, than at 2.45 GHz. However, such high frequencies are not cost-effective for lab-scale experiments and may result in thermal runaway (i.e. thermal instability caused by an increase in local temperature accompanied by an enhanced microwave energy absorption, which results in local acceleration of heating, a further rise in temperature in an uncontrolled manner).

An electromagnetic wave incident on a conducting surface is attenuated in the material over a characteristic distance known as the skin depth δ, which is the distance at which the power drops to 1/e (0.368) from its value at the surface.

$$\delta = \sqrt{\frac{2\rho}{\omega\mu}} \sqrt{\sqrt{1 + (\rho\omega\varepsilon)^2} + \rho\omega\varepsilon} \qquad (4.2)$$

where ρ is the electrical resistivity, ω is the angular frequency, μ is the permeability, and ε is the permittivity. Materials with high penetration depths are considered microwave transparent (e.g. quartz glass), and materials with extremely low penetration depths will exhibit most of the heating at the surface. Many materials suscept to microwave energy, but different temperatures must be reached prior to this behavior being exhibited. For example, zirconia does not suscept to microwave energy at room temperature. However, it will begin to suspect between 600-1,200°C.

Unfortunately for the ceramic breeder candidates Lithium Orthosilicate and Metatitanite, there is enormous variation in skin depth at a given frequency because of the very large change in both electrical conductivity and permittivity with temperature. This means that heating the pebbles may be possible at elevated temperatures but very difficult at low temperature. Preheating the pebble bed segment using the cooling fluid before applying external heating to simulate the nuclear heating could avoid this problem but may not be possible if the desire is to simulate the heating from start of plasma burn to get transient effects. If the objective of the bulk heating simulation experiments is to get data on the thermally induced stress in the pebble bed, the container surrounding the pebbles must be mechanically and thermally similar to the anticipated breeder design so the boundary conditions are representative. Since the breeder material is contained in a conducting box, any induction or microwave heating scheme must operate at a frequency low enough to have significant energy penetrate through the box wall. If we assume the box is SS316 and the wall is 4 mm thick, an operating frequency of 400 Hz will allow about 83% of the wave energy to be transmitted through the wall to the silicate. Only at very high frequency and temperatures do the pebbles come close to having an acceptable skin depth, but such high frequency waves will not penetrate the steel box.

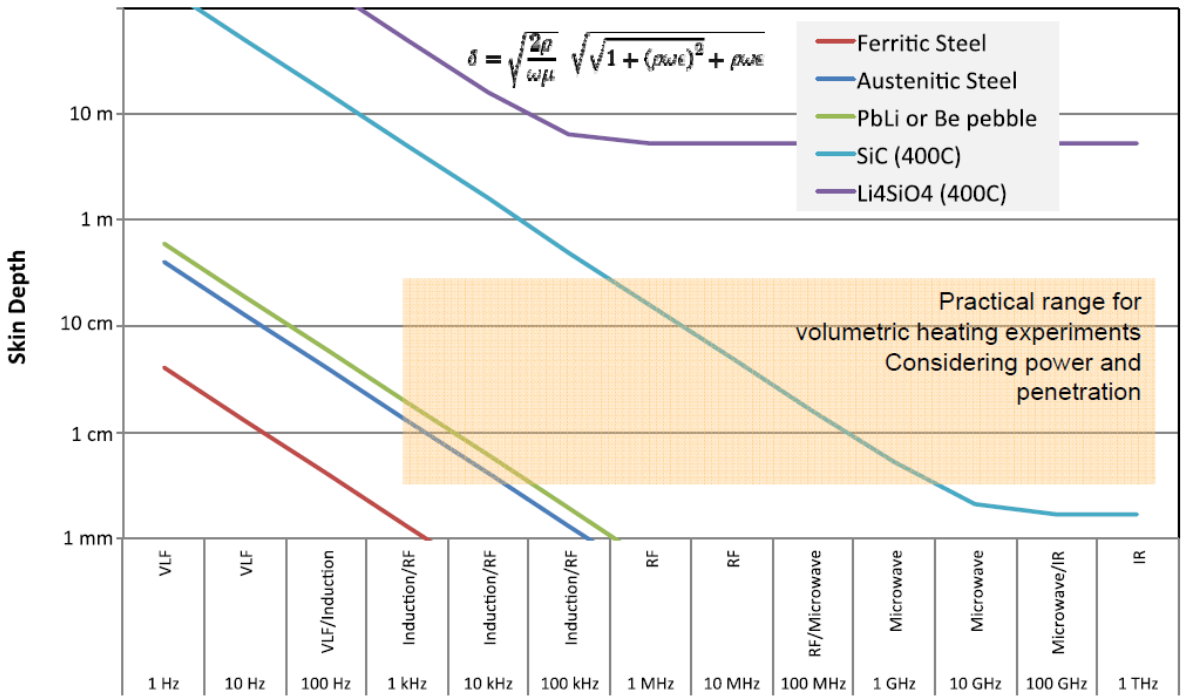

Figure 4.2. Skin depth for various materials show only limited opportunities to use microwave or induction heating for breeder materials[33].

Figure 4.2 shows no potential in using the induction, microwave or RF heating since the size of the pebbles is around 1 mm and the skin depth is greater than 8 m at 400 C, making them transparent to EM waves.

After thoroughly reviewing various methods of volumetric heating, such as microwave and induction heating (further details in Appendix D), using strands of wire heaters proved to be the most feasible option and is discussed in the following section.

4.2. TESOMEX 1.0 pre-experimental analysis/modeling, design and implementation

In order to simulate the conditions inside a solid breeder, we must develop and prove the feasibility of an experimental technique to simulate the nuclear heating profiles in a solid breeder without notable disruption to thermomechanical response of the pebble bed. Moreover, we must explore and identify non-intrusive diagnostic/instrumentation techniques to measure the pebble bed properties, with minimal impact on the pebble bed behavior.

A primary objective of the multi-effect experiment is simulation of nuclear heating profiles with novel heating techniques without disrupting the natural behavior of the granular pebble bed. To this end, embedding matrices of wire heaters in the pebble bed has been chosen as the most feasible solution similar to Premux studies[34]. The heaters are connected to independent power blocks to allow custom-tailored heating profiles. The heater assembly had to satisfy the following requirements and considerations to ensure the satisfaction of experimental objectives:

1. Impose minimal local packing disturbance
2. Simulate nuclear heating temperature profiles
3. Perform reliably from an electrical standpoint
4. Maintain ease of assembly and fabrication

Analysis of the wire matrix disruption to thermo-mechanics has been performed with both DEM and FEM models and is discussed below.

4.2.1 Wire heater matrix selection, design criteria, and implementation

4.2.1.1 Simple case analytical solution derivation and FEM thermal model validation

If we consider the simple case of the flow of heat in an infinite circular cylinder, we find that the heat conduction equation expressed in cylindrical coordinates is:

$$\frac{\partial T}{\partial t} = k\left(\frac{\partial^2 T}{\partial r^2} + \frac{1}{r}\frac{\partial T}{\partial r} + \frac{1}{r^2}\frac{\partial^2 T}{\partial \theta^2} + \frac{\partial^2 T}{\partial z^2}\right) \tag{4.3}$$

If a circular cylinder whose axis coincides with the axis of z is heated, and the initial and boundary conditions are independent of the coordinates θ and z, the temperature will be a function of **r** and **t** only, and this equation reduces to:

$$\frac{\partial T}{\partial t} = k\left(\frac{\partial^2 T}{\partial r^2} + \frac{1}{r}\frac{\partial T}{\partial r}\right) \tag{4.4}$$

For the steady state case, if the solid is a hollow cylinder whose inner and outer radii are r_1 and r_2, Equation (4.3) becomes:

$$\frac{\partial}{\partial r}\left(r\frac{\partial T}{\partial r}\right) = 0, \quad r_1 < r < r_2 \tag{4.5}$$

Which has a general solution of:

$$T = A + B\ln(r) \tag{4.6}$$

Where A and B are constants to be determined from the boundary conditions at r= r_1 and r= r_2.

If the temperature at r_1 is kept at T_1. At r_2, there is ambient convection into the medium at h and T_2 with the boundary condition being:

$$\frac{dT}{dr} + h(T - T_2) = 0, \quad r = r_2 \tag{4.7}$$

We have,

$$T = \frac{T_1\left[1 + hr_2\ln\left(\frac{r_2}{r}\right)\right] + hr_2T_2\ln(\frac{r}{r_1})}{1 + hr_2\ln(\frac{r_2}{r_1})} \tag{4.8}$$

If heat is supplied at a constant rate q' per unit length of the inner cylinder, since it follows from (4.5) that $\left(r\frac{\partial T}{\partial r}\right)$ is constant, the flow of heat over a cylinder is independent of its radius, and:

$$q' = -2\pi rk\frac{dT}{dr}, \quad r_1 < r < r_2 \tag{4.9}$$

Then if T_1 and T_2 are the temperatures at r_1 and r_2 respectively, integrating (7), we get:

$$2\pi k(T_1 - T_2) = q' \ln\left(\frac{r_2}{r_1}\right) \tag{4.10}$$

If the heat is supplied by a wire along the axis of the cylinder of resistance R ohms per unit length and carrying current I amps, we have:

$$q' = I^2 R \tag{4.11}$$

Substituting equation (10) into (8), we get:

$$T(r) = \frac{T_2\left[1 + hr_2 \ln\left(\frac{r_2}{r}\right) + hr_2 \ln\left(\frac{r}{r_1}\right)\right] + \frac{q'\left[1 + hr_2 \ln\left(\frac{r_2}{r_1}\right)\right]\left[1 + hr_2 \ln\left(\frac{r_2}{r}\right)\right]}{2\pi k h r_2}}{1 + hr_2 \ln\left(\frac{r_2}{r_1}\right)} \tag{4.12}$$

- The results shown in Figure 4.3 are generated by substituting the values in Equation (4.12) for a 1 mm heater wire generating 2 KW/m embedded in a 10 mm cylinder of K=1.2 W/m.K.

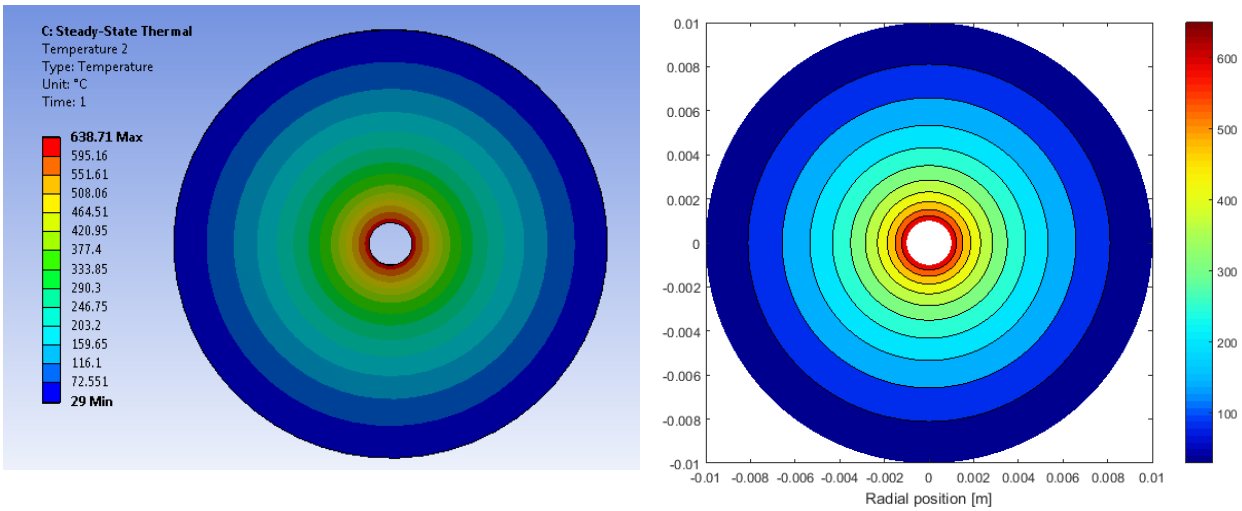

a) ANSYS model solution b) MATLAB Analytical solution

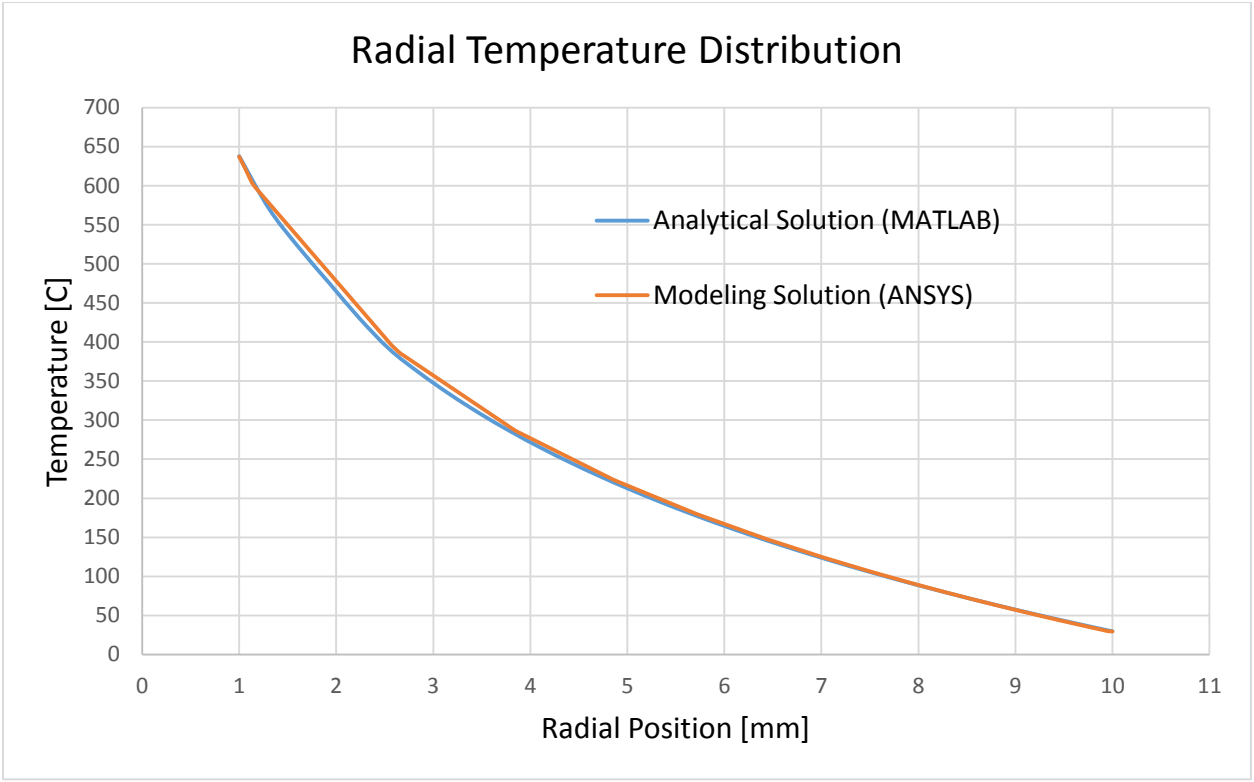

Figure 4.3 showing almost discrepancy between the analytical solution and the ANSYS model.

4.2.1.2 FEM/DEM analysis toward selecting an optimal wire heater configuration

After validating the ANSYS thermal model against the simple analytical solution case, numerical modeling of the interaction between pebble bed assembly with coolant structure and wire heaters was first analyzed with finite element method (FEM) models. FEM models provided a route toward optimization of heater wire schemes, power deposition requirements, and expected temperature distributions in the pebble bed.

In addition, a major requirement of the experiment is to attain breeder-bed-relevant thermomechanics which requires that heater wires should not disrupt the random packing which happens in the bulk region of solid breeder pebble beds. Thus we also performed discrete element method (DEM) investigations of representative volumes of TESOMEX to determine packing structure disruption due to heater wire size and spacing. DEM simulations were performed on a unit cell representative of the bulk region in TESOMEX. The first objective was to determine if the large wires imposed any packing structure on the bulk of the pebble bed where random packing would exist in a typical pebble bed. The second goal was to consider heat transfer between the heater wires and nearby pebbles from a contact conductance point of view.

In the DEM model, a single unit cell of the system was analyzed; the unit cell, as looking down from above, is shown in Figure 4.4 with the locations of the three unit-cell heater wires identified. The conditions analyzed had: control case of no wires, small wires of diameter 0.5 mm, medium wires of diameter 0.8 mm, and large wires of diameter 1 mm.

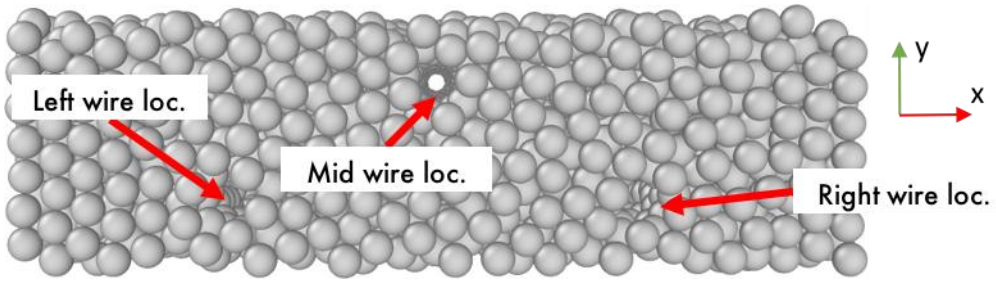

Figure 4.4: Perspective view of a single unit cell looking down into wire openings. The unit cell is periodic in y with rigid walls at the limits of x.

Analysis of packing structure was performed by measuring the radial/linear distance of pebble centroids near the three wire locations C_1, C_2, and C_3 as well as near the wall. For the wall, commonly-seen structured packing is seen in the high peak/ deep valleys of the histograms in Figure 4.5 (a-d). In order for the pebble bed in the experimental setup to behave most like pebble beds in actual breeding blankets, the heater wires cannot disrupt the thermomechanical interactions in the ensemble. From the DEM packing analysis, 1 mm diameter wires impose much packing structure internally to the bed, and as a consequence thermomechanical responses of the pebble bed during heat cycles will be affected and such wire sizes should not be considered. For wire diameters 0.8mm and below, significantly less packing structures are formed and should be acceptable from a stable thermomechanical point of view.

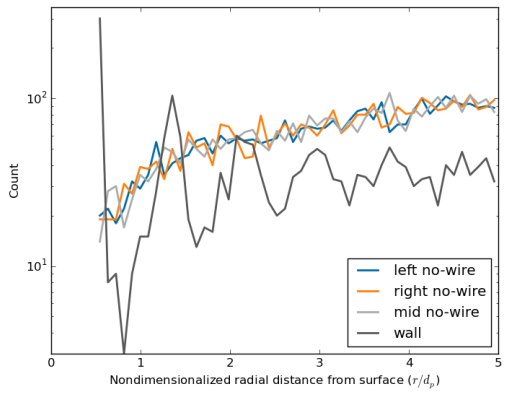

a) At bed locations where wires would be present, no packing structures are formed in control case.

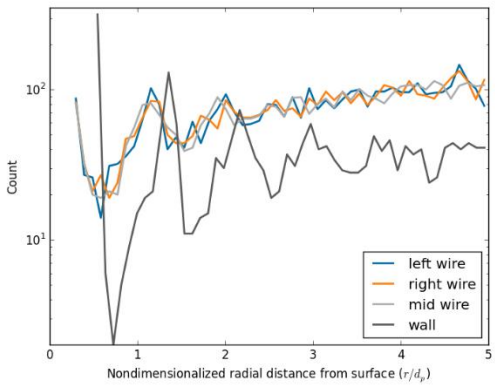

b) With 0.5 mm wire diameter, small packing structures are formed but completely disappear after 2 pebble diameters distance from wire.

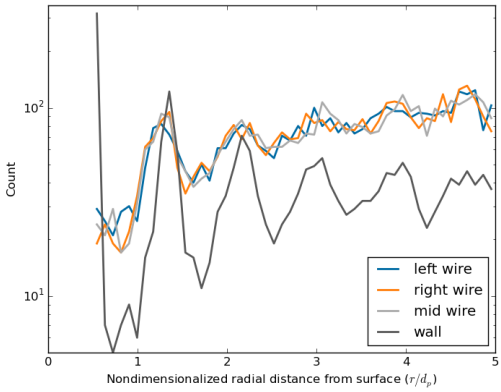

c) With 0.8 mm wire diameter, slightly larger packing structures are formed near wires but are only faintly present after 2 pebble diameters and removed at approximately 3 pebble diameter distance from wire.

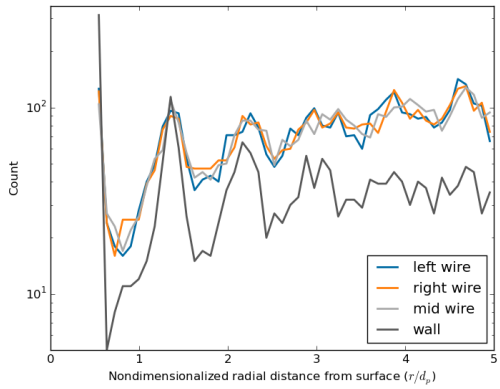

d) With 1 mm wire diameter, packing structures are created that extend beyond 3.5 pebble diameters, beyond which structuring from neighboring wires are visible.

Figure 4.5: Logarithmic histogram of pebble centroids near structure surfaces. Wire spacing is 7 mm, pebble diameter is 1 mm. Highly structured packing is found near walls, visualized as peaks near 0.5, 1.5, etc. up to approximately 4 pebble diameters. Note that increase in

count as a function of r for ‘wire’ conditions is due to increasing volume spanned with constant Δr slices in radial coordinate system.

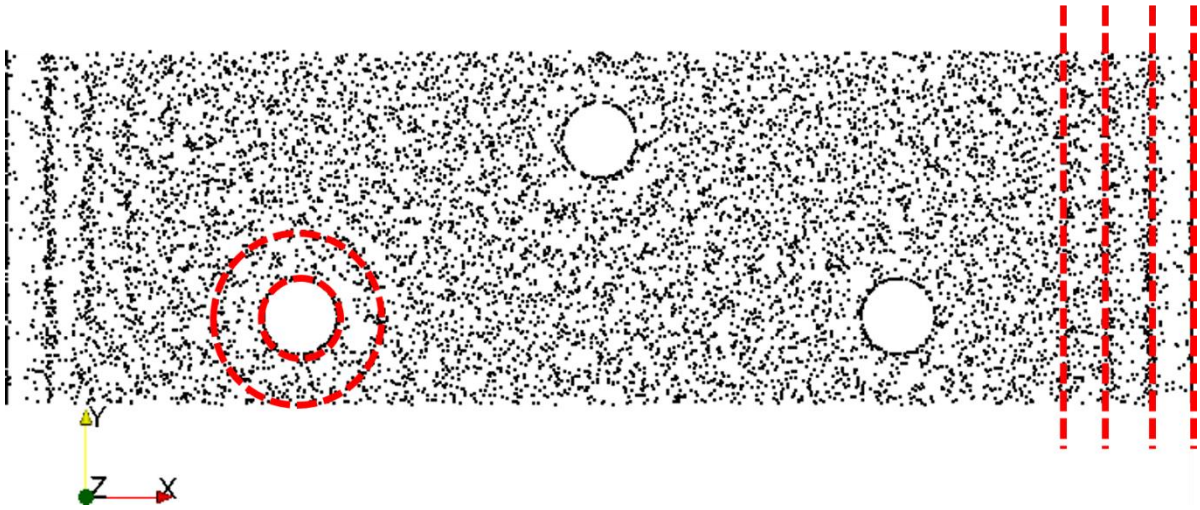

a) Weak structural formation is seen in the second ring (2 pebble diameters) away from the 0.5 mm heater wire. The bed is mostly random packed.

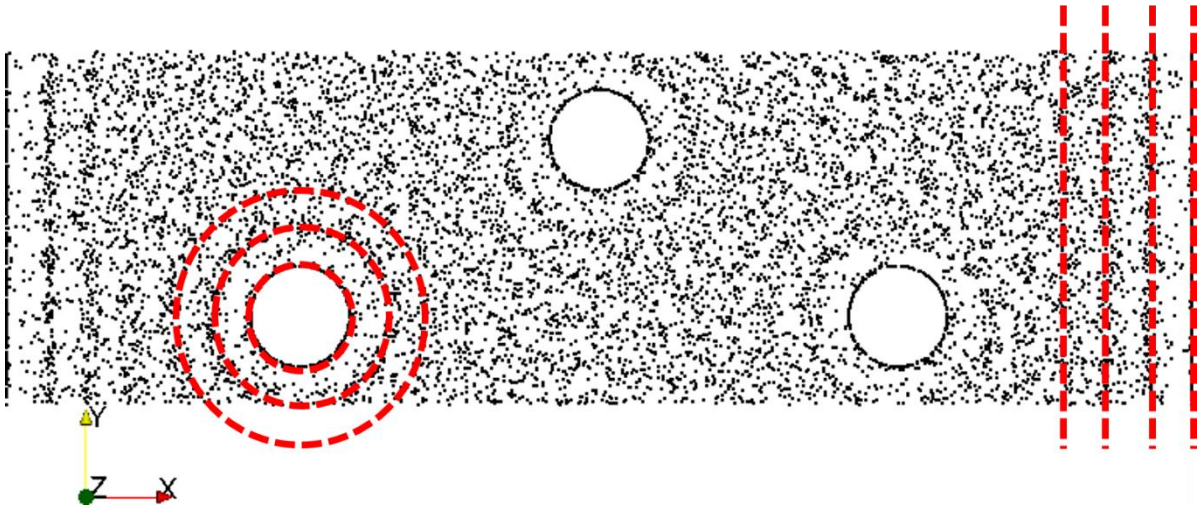

b) Strong structural formation due to pebble arrangement near 1 mm heater wires. Three rows of formation are visible near heater wires.

Figure 4.6: Strong structural formation due to pebble arrangement near side walls, highlighted on right of (a) and (b). Packing structuring around the heater rods in (b) extends 3 diameters beyond the wire; formation in (a) is only light by the second diameter.

Temperature distributions in the DEM pebble bed were also calculated for the cases with embedded heater wires, shown in Figure 4.7. Due to the small surface area of the 0.5 mm wire, heating from the wire is concentrated into the few pebbles in contact. These pebbles consequently have much higher temperature than their neighbors, Figure 4.5 (a). Because many phenomena in pebble beds are a result of increased temperature, we must avoid the situation with high localized temperature spikes and thus concluded that wire sizes of 0.8 mm are the smallest that should be implemented in TESOMEX.

The DEM results shown above considered only packing structure formation and localized spikes in heating for a unit cell. In order to achieve prototypical temperature values and distributions in the pebble bed, the number and density of heater wires in the entire assembly must also be considered. Using DEM results as guidance, in order to maintain the mechanical integrity of the pebble bed, a design comprised of largely spaced fine wires is preferred. However, FEM analysis also revealed that, in such a configuration, power deposition in each wire exceeds surface loading requirements as shown in the bottom right corner of Figure 4.9 designated as wire configuration #10. Consequently, surface temperatures of the fine wires (0.5 mm) were unreasonably high and would significantly lower the heaters' service life. A compromise of larger wires (0.8 mm) with slightly denser packing was made. Differences in temperature distributions obtained with different packing densities is shown in Figure 4.9. The configuration finally chosen struck a balance of wire density and ability of the heaters to create prototypical nuclear heating profiles. The final configuration is shown in the bottom-left image of Figure 4.9, designated as

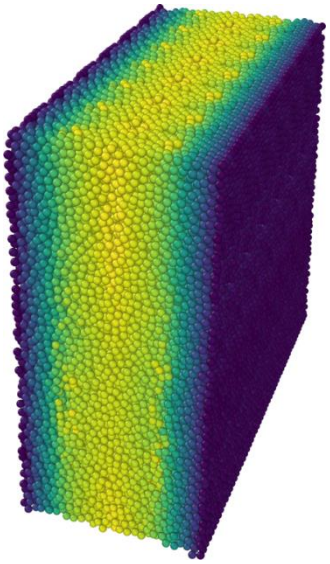

a) Isometric view of pebble bed system in DEM with color map to nondimensional temperature (showing the 1 mm heater wire condition)

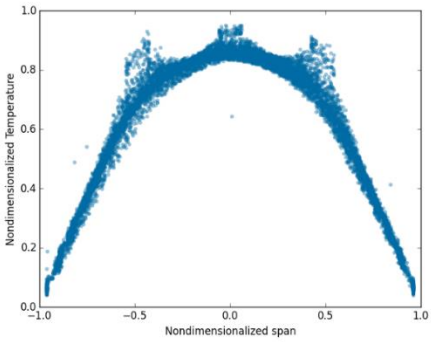

b) Nondimensional temperature distribution across x for all pebbles in the DEM system with 0.5 mm wires. Large local spikes are seen in the system with lower overall temperatures.

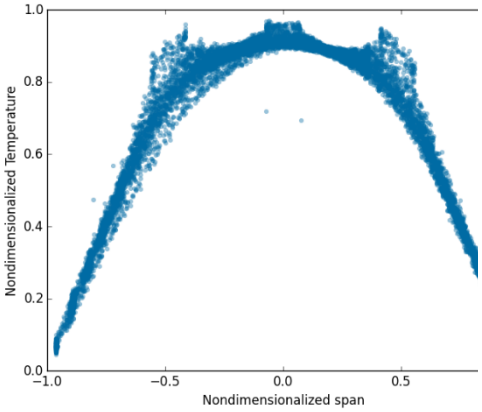

c) Nondimensional temperature distribution across x for all pebbles in the DEM system with 0.8 mm wires. Localized temperature spikes are smaller than the 0.5 mm case and temperatures are overall higher.

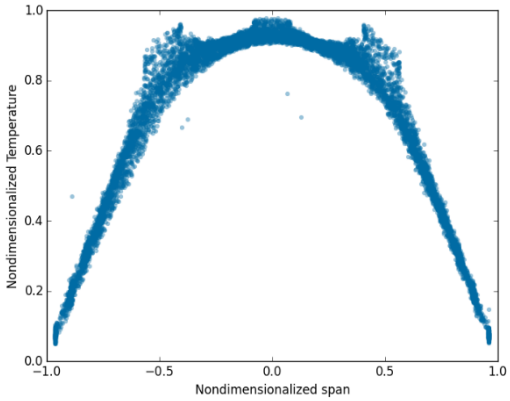

d) Nondimensional temperature distribution across x for all pebbles in the DEM system with 1 mm wires. Localized spikes in temperature are small and overall bed temperatures are highest.

Figure 4.7: Temperature analysis in DEM shows no variation along z and only localized influences of heaters. The majority of the pebble beds in the volume experience temperatures along a distribution representative of volumetric nuclear heating.

configuration #4.5. To quantify variation in temperature profiles along radial paths in the pebble bed, Figure 4.8 (a) shows a plot of the temperature distribution versus radial location along 3 radial paths for our chosen wire configuration: one passing through one heater wire, another passing through two wires, and a third path along the midpoint between the wires. The FEM-based temperature profile shows acceptable limits to localization of heat increase due to inserted heater wires.

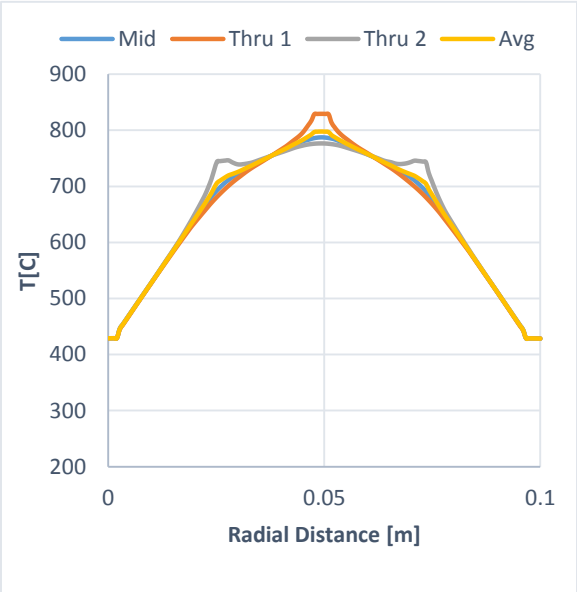

a) Temperature profiles through several cross-sections determined from FEM simulations

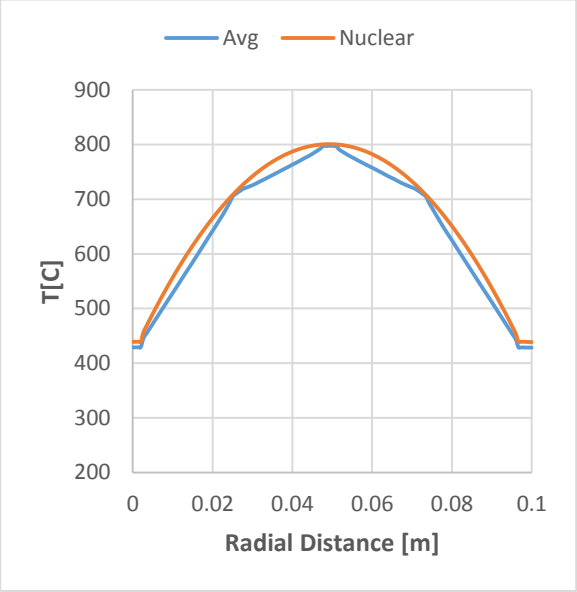

b) average radial path temperature profile compared to nuclear heating profile

Figure 4.8: Temperature analysis for chosen wire heater configuration in (a) FEM-based analysis and (b) DEM-based analysis indicate acceptable temperature spikes and comparison with nuclear heating for pebbles in contact with heater wires. In FEM, contact conductance is a prescribed value.

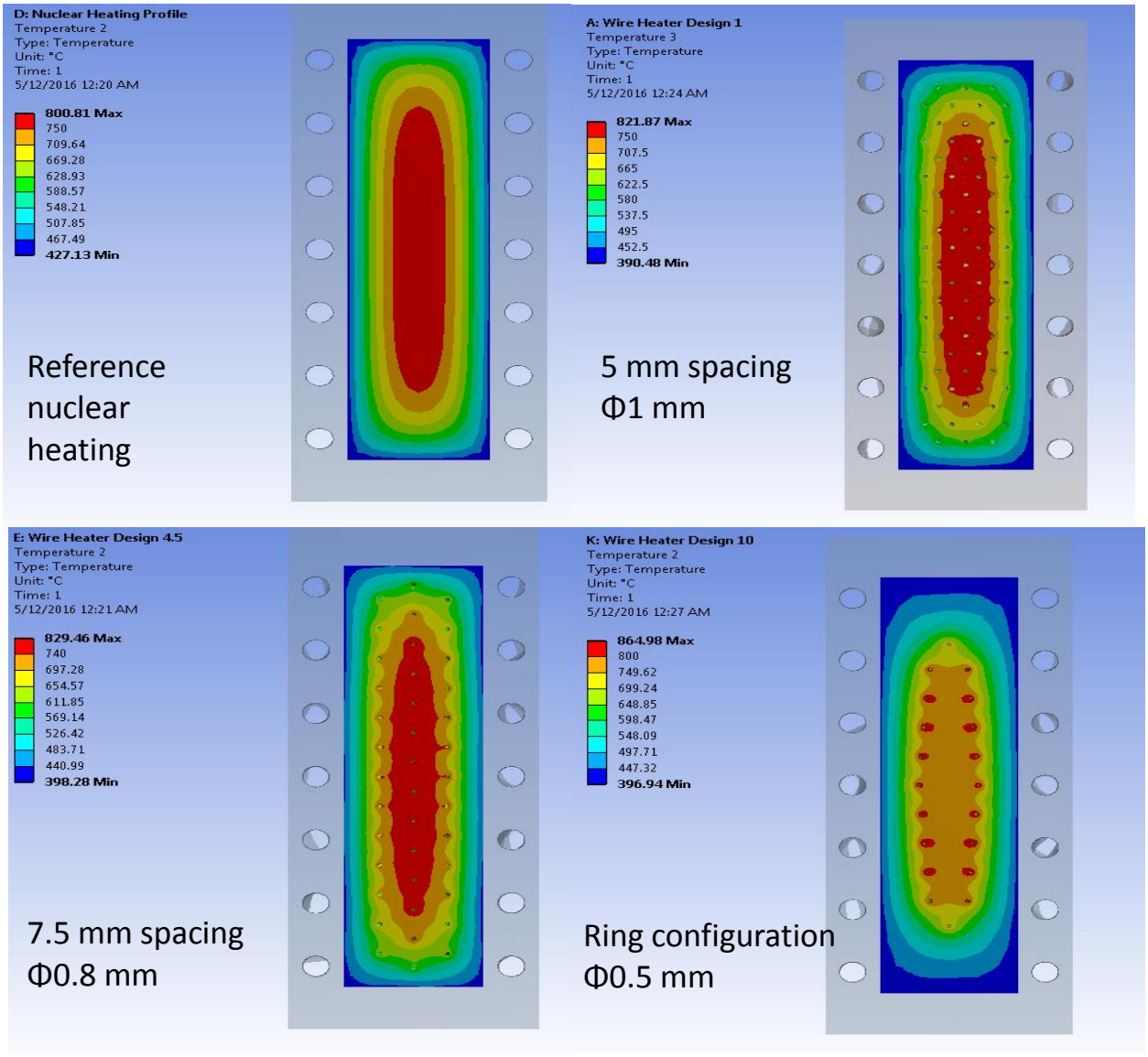

Figure 4.9: Mid-section temperature contours with nuclear heating (top-left), the most dense-wire-matrix (top-right), the least dense (bottom-right), and a compromise heater matrix (bottom-left) demonstrating the heater wire ability to recreate volumetric heating temperature distributions, while adhering with packing disruption limitations.

4.2.1.3 Electrical and power characteristics

From an electrical stand point, three important points were considered: a) Wire resistance/temperature sensitivity, b) Power/Surface loading, c) Transient heating.

a) Wire resistance/temperature sensitivity:

It is crucial for the heater wire to have a stable resistance over a wide range of temperatures to minimize power level fluctuations. The property that describes this behavior for a specific wire material is the Temperature Coefficient of Resistance (TCR). Therefore, the optimal heater wire material should have a low TCR.

$$R = R_{ref}(1 + \alpha(T - T_{ref}) \quad (4.13)$$

Where, R= Wire resistance at temperature T

R_{ref}= Wire resistance at temperature T_{ref}, commonly room temperature 20 °C

α = Temeprature Coefficient of Resistance, analogous to the slope of the curve.

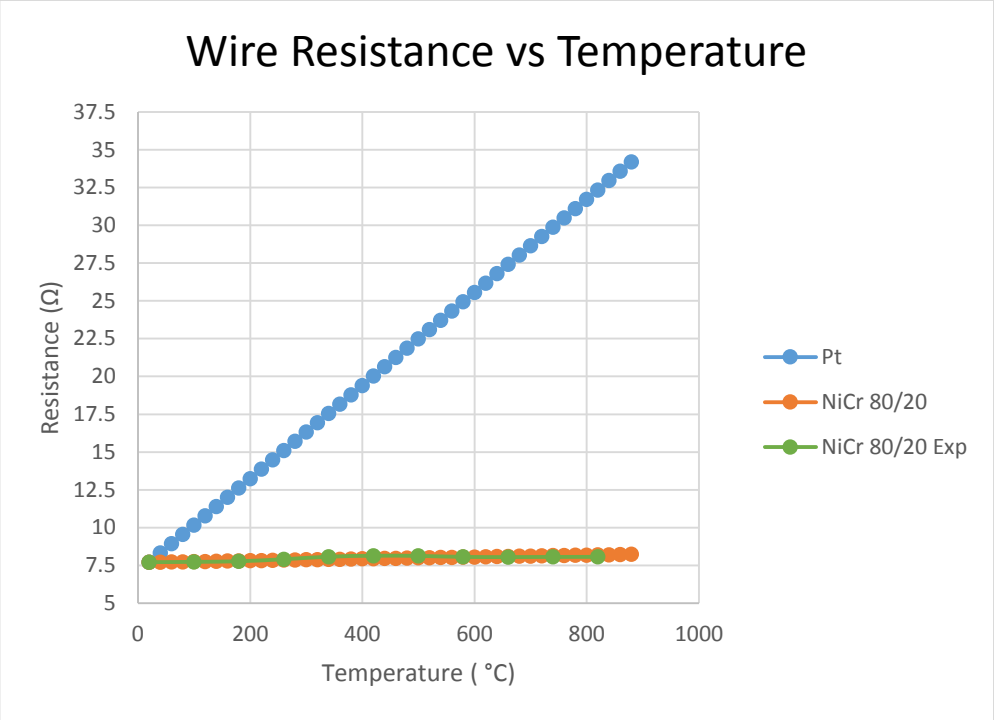

Figure 4.10: Stability of the change in resistance with temperature for NiCr wires

b) Power/Surface loading:

For NiCr 80/20 (20 AWG→0.8 mm diameter), resistivity $\rho = 1.09*10^{-6}$ Ω.m, maximum power desired P_{max}= 800 W for each heater block (1600 W total power), wire length L=3.5 m (7m total).

Total wire resistance at room temperature:

$$R_{Tref} = \frac{\rho L}{A} = \frac{\rho L}{\frac{\pi}{4}D^2} = 7.6\ \Omega \tag{4.14}$$

Total wire resistance at 800 °C operating temperature:

$$R_T = R_{Tref}\left(1 + 0.00008(800 - 20)\right) = 8.07\ \Omega \tag{4.15}$$

Which was verified experimentally to be 8.06 Ω

$$P = I^2 R \tag{4.17}$$

$$\text{for } I = 10 \text{ A}$$

$$P = 807 \text{ W } (1614 \text{ W total})$$

$$\text{Surface loading} = \frac{P_{max}}{\pi DL}\ 9.17 \text{ W/cm}^2 (\text{well below limit})$$

Surface loading values recommended for maximizing heating element's service life vary depending on the application. For heating element embedded in insulation (pebbles), the allowed surface loading varies from 15- 80 W/cm^2.

c) Transient heating and description of short/long-pulse experimental campaigns

Unlike the previous experimental set-ups which had relatively large time constants and no realistic thermal cycling effects, the heating scheme with applied cooled boundary utilized in TESOMEX is expected to reproduce ITER-relevant thermal cycles that are more representative of fusion's pulsed operation. The heat capacity of the small heating elements is much lower than that of the large conventional plate surface heaters, making the wire heater a perfect candidate for accommodating the rapid transients of the pulsed operation planned for ITER. The experimental campaign will operate with two heating schemes: (i) ITER inductive heating cycles (short pulse) and (ii) ITER hybrid heating cycles (long-pulse). The short-pulse of standard ITER inductive heating is 400/1800 of plasma on/off. In the short heating cycle, it is not expected to reach a steady-state thermal condition. The thermomechanical responses will be unique from steady-state conditions that will be reached in the long-pulse hybrid heating cycle of 1000s burn time.

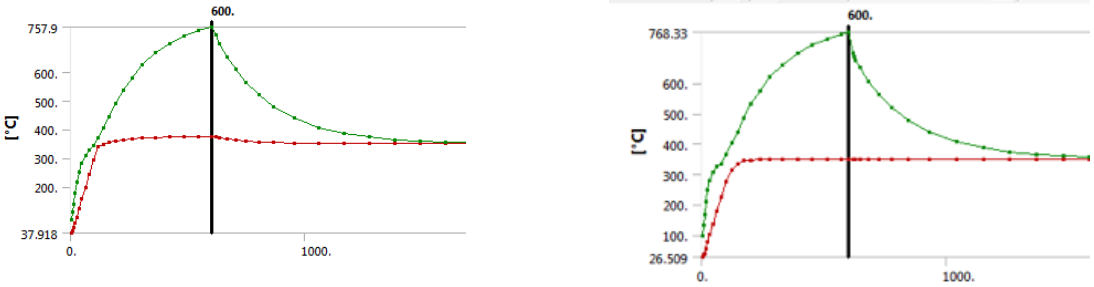

a) Volumetric heating b) TESOMEX wire-matrix heating

Figure 4.11: Example temperature profiles (peak in green, minimum in red) achievable with TESOMEX wire matrix heating matching the inductive heating cycle

4.2.1.4 Final heater assembly considerations

Finally, the different configurations were evaluated from a design for assembly (DFA) point of view, and the densely distributed wires option has been discarded due to the difficulty of accurately placing a large number of wires closely spaced while maintaining the straightness over an 18 cm length. Configuration #4.5, on the other hand, was reasonably easier to assemble after iterating with several methods and assembly steps. Figure 4.12 a) shows the early assembly technique of passing the wires through the ceramic spacer, which fails to maintain the straightness of the wires, followed by b,c) a systematic approach of pre-bending the wires into u-shaped sections and crimping/spot-welding them at the opposite side of the spacer after wiring the two circuits, and lastly, d) showing the final assembly being tested up to about 1400 W.

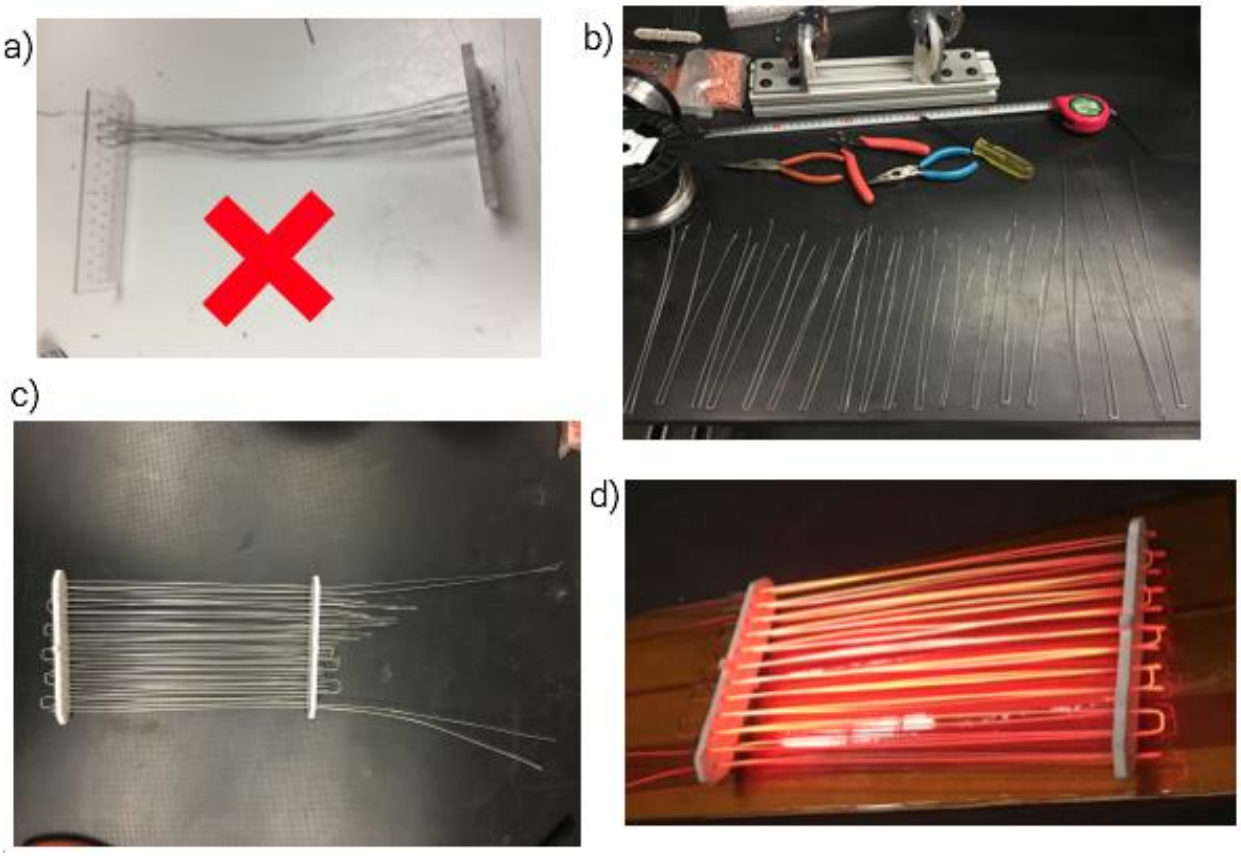

Figure 4.12 Heater wire assembly iterations and final testing.

4.2.1.5 Maximizing experimental data value with effective instrumentation and diagnostic tools

The difficulty of experimentally probing pebble beds stems from the fact that macroscopic responses are accumulated effects of myriad pebble-pebble and pebble-wall interactions. Moreover, many standard instrumentation techniques disrupt pebble beds in such a way that the act of measuring alters the fundamental behavior of the pebble beds. As such a significant effort has been made to consider proper data acquisition and instrumentation techniques in order to

extract the most useful information possible from the experimental campaign without disruption to the natural behavior of the pebble bed. Previous, single-effect experimental studies at UCLA have shown that volumetric compaction from induced thermal stresses are present primarily during the first heat cycle but afterwards are accommodated by a combination of pebbles settling, rearrangement (*i.e.* plastic strain) within the bed, and thermally-induced creep deformation. The accumulation of creep deformation leads to stress relaxation which may reach a state of equilibrium in the pebble bed. These thermomechanical effects are all expected to manifest in synergistic ways in TESOMEX. In this experimental campaign, it is therefore critical to have: (i) temperature measurements which will reflect rearrangement-effects on temperatures in the bed, and (ii) high resolution temporal measurements of stress at specific locations on the pebble bed container, (iii) means of inspecting local and global changes to pebble bed packing structures and topography.

An outcome of volumetric compaction and creep relaxation are global effects such as resettling and local effects such as inter-particle necking. Resettling of packing structures can be revealed in variations of temperatures along the poloidal direction of TESOMEX as well as global increases in temperature distributions after initial heating cycles. However, in past experimental campaigns on solid breeders performed at UCLA, it has become obvious that excessive thermocouple insertions to pebble beds disrupts both packing structures as well as energy transfer due to the metallic sheaths surrounding the thermocouples. Therefore, we plan to insert the minimum number of single-point and multipoint thermocouples that still allow accurate reconstruction of temperature distributions with least disturbance to the bed. We intend to place three pairs of independent thermocouples symmetric about the radial, poloidal, and toroidal axes, temperature profile symmetry and uniformity can be tested as shown in Figure 4.13. The majority

of temperature measurements will occur on a single plane near the center of the pebble bed. Gravity/resettling effects will be determined through temperature measurements at a second plane 5 cm above in the poloidal direction.

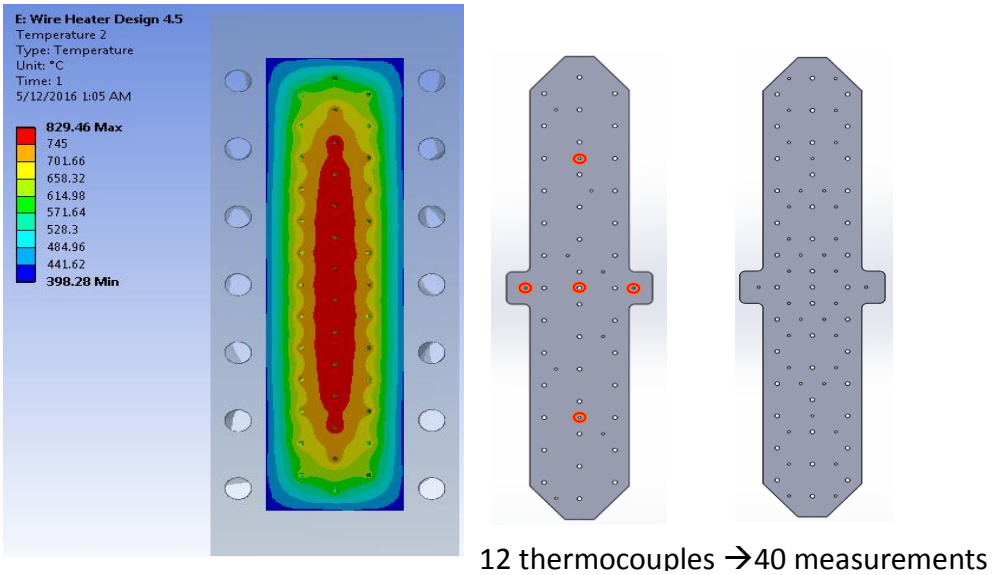

Figure 4.13 Thermocouples distribution for maximizing measurement efficiency

Spatial distribution of temperature measurements will be ensured by securing thermocouple endpoints to the same ceramic spacer frame holding the heater wire matrices. The proposed material for the ceramic spacers which hold the heater/thermocouples assembly is MACOR. This material has many desirable properties that suit the application: low thermal conductivity (1.5 W/m.C), low thermal expansion coefficient, excellent machinability that allows for drilling small holes with high precision, good thermal shock resistance, high operating temperature (1100 °C), and low dielectric strength.

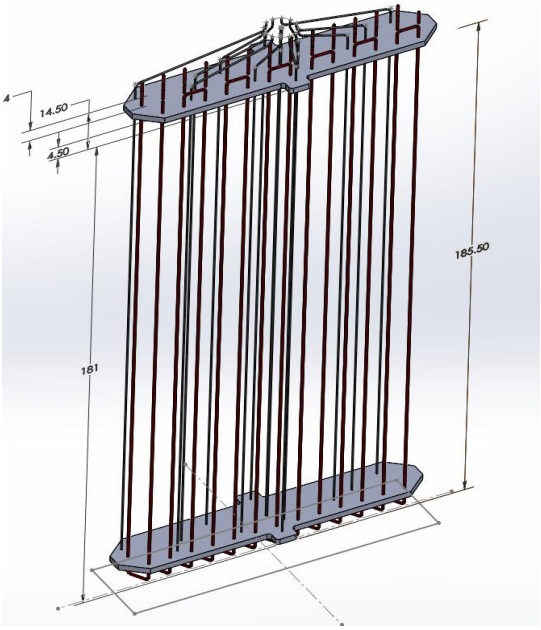

a) CAD drawing of heater matrix with ceramic spacers and thermocouple probes.

b) Assembled heater block with two MACOR spacers for support and position stability.

Figure 4.14: Final heater assembly

4.2.1.6. Summary of heater selection

Nuclear heating profiles are accomplished by means of hexagonal matrix of wire heaters. The wire heaters and thermocouples span the length of the bed and are held in place by ceramic spacers to maintain the wires' geometric stability and accurate placement.

The resistance heating wire selected is a nickel-chromium alloy comprised of 80% Nickel and 20% Chromium, commercially known as NiChrome 80/20. This alloy is suitable for use at temperatures up to 1200°C and is characterized by high resistivity, good oxidation resistance, very good form stability, and excellent ductility after use. A particular crucial point for this wire is its stable resistance (with a temperature coefficient of resistance of 0.00008) over a wide range of temperatures to minimize power level fluctuations. Wire size and geometric distribution were selected based on several factors, including: temperature profile, packing disruption, power requirements, and ease of assembly. The heater assembly with ceramic stiffening ribs is shown in the detailed heater matrix of Figure 4.14 (b). Also shown in Figure 4.14 (a) are the thermocouples with leads bundled toward a single connection point at the top of the assembly.

After consideration of temperature profiles, packing disruption, power requirements, and ease of assembly, we conclude that a wire matrix of 0.8 mm wires, with 7.5 mm spacing, arranged in wire matrix configuration #4.5 is the optimum balance satisfying all the requirements. Figure 4.15 shows a spider plot highlighting the relative scores of each of the wire configurations discussed above.

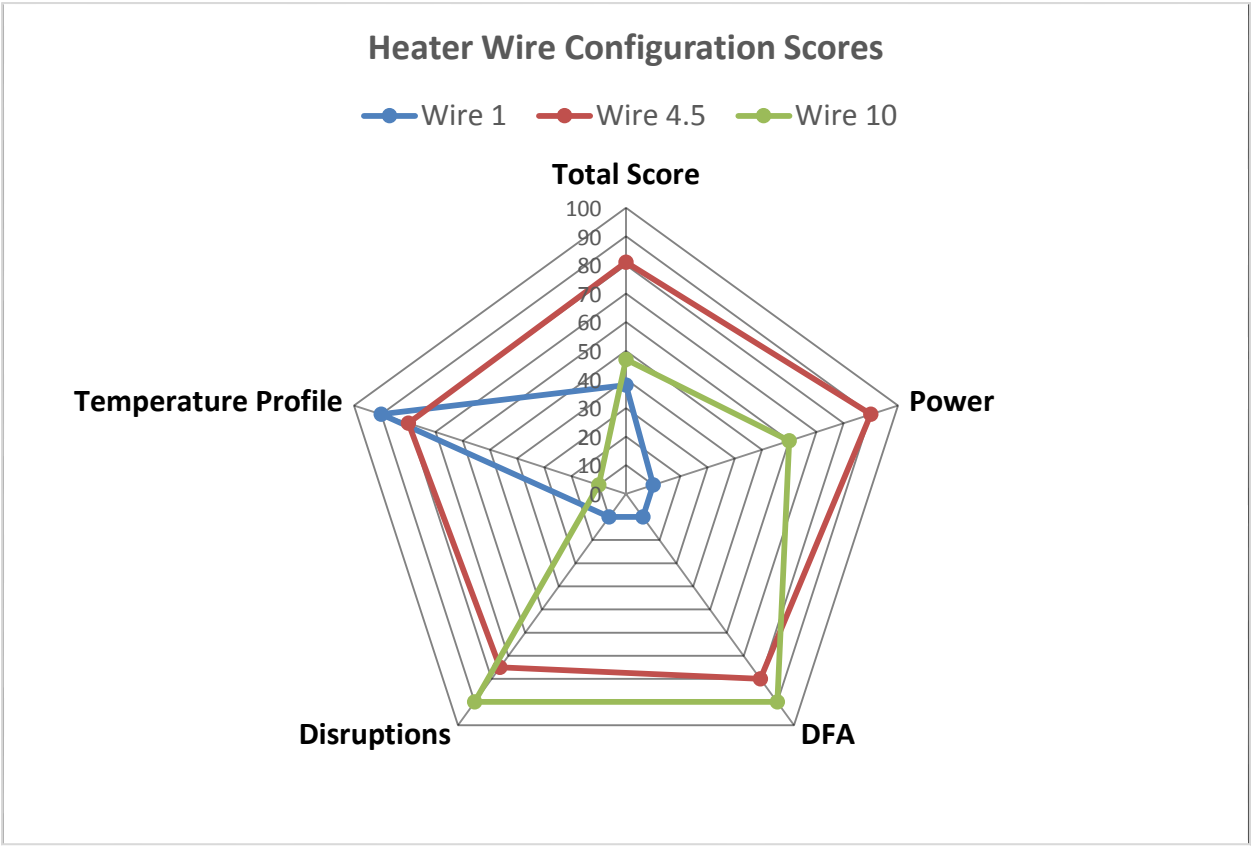

Figure 4.15: heater selection scoring chart showing highest rating for configuration #4.5

The selected heater assembly is divided into two independently powered heater blocks to allow flexibility for simulating asymmetric nuclear heating temperature profiles. For a NiChrome 80/20 wire of the specified dimensions, each heater block can deploy up to 1000 W without exceeding the surface loading requirements, and create a temperature distribution that fairly matches the volumetric heating profile.

4.2.2 Test article and coolant manifold design optimization and CFD modeling

The preliminary setup consists of a test-box with inner pebble bed volume dimensions of 22x10x2.5 cm^3. Nuclear heating profiles are accomplished by means of hexagonal matrix of wire heaters. The wire heaters and thermocouples span the length of the bed and are held in place by ceramic spacers to maintain the wires' geometric stability and accurate placement. Two cooling plates on opposite faces of the box to provide adequate heat rejection and impose the desired temperature boundary conditions. The container flanges are equipped with vacuum-sealed connections for wire terminals, thermocouples bundles and tubes for Helium purge flow inside the pebble bed volume. The bed geometry/dimensions were chosen in such a way that conclusions for the typical Ceramic breeder modules such as HCCR (Helium Cooled Ceramic Reflector) relevant cavities could be drawn including a prototypical width for reproducing a bed temperature gradient with an adequate height where pebble rearrangements due to gravity settling can be observed. However, engineering scaling had to be performed to ensure blanket relevant compressive loads can be generated in the bed if additional structural constraints would have to be imposed. Further analysis of the manifold design is presented below.

4.2.2.1. TESOMEX 1.0 CFD Analysis

Several manifold configurations, of which four cases are presented in Figure 4.16, were modeled via the commercial code ANSYS CFX under the following physical models, flow conditions, and parameterization:

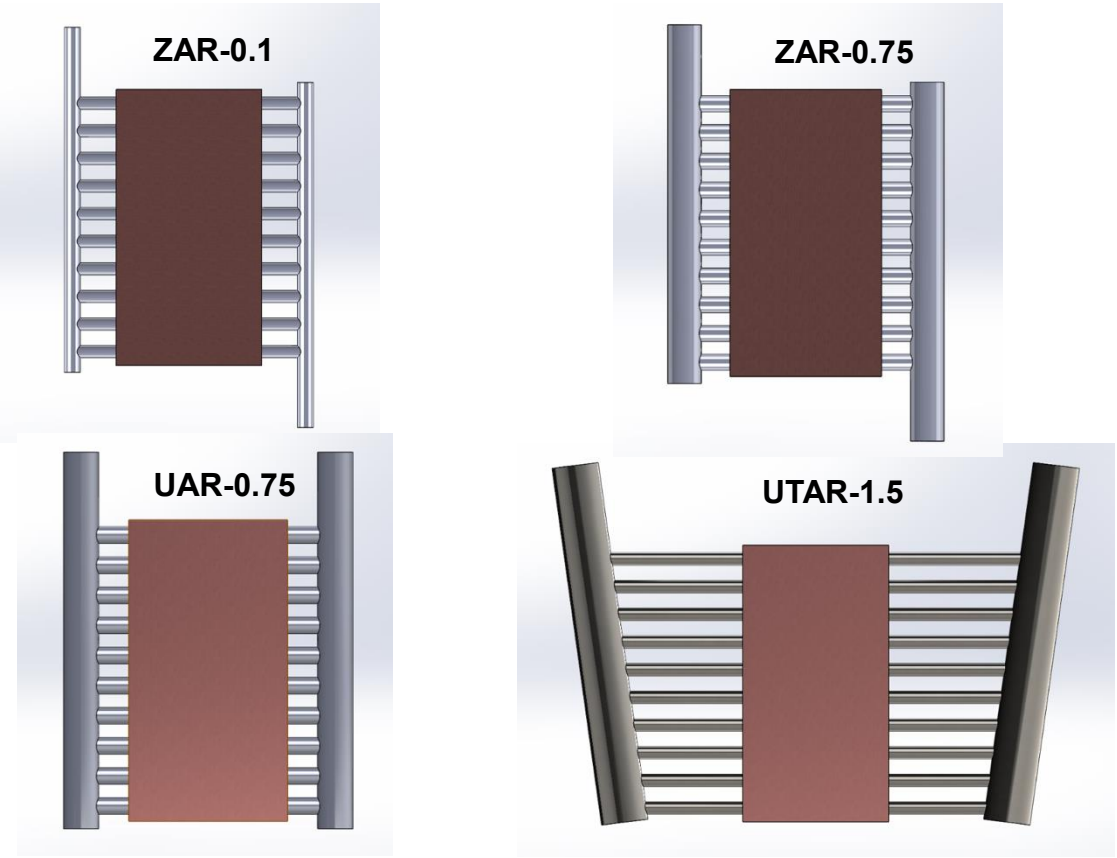

AR→ the ratio of the cross-sectional area of the manifold header to the total cross-sectional area of individual channels

Z→Parallel flow (same inlet/outlet flow directions)

U→Reverse flow (opposite inlet/outlet flow directions)

T→tapered

UTAR-1.5 → Reverse flow, tapered manifold with an area ratio of 1.5.

Figure 4.16. Highlighting four of the analyzed test article manifold configurations

- **Employed physical models: Turbulence, Full buoyancy.**

  Shear Stress Transport Turbulence (SST) Model

  - overcomes the shortcomings of k-ε and k-ω models.
  - blends between the two models according to the distance from the wall.
  - accounts for transport of turbulent shear stress.
  - Prevents over-prediction of eddy viscosity.
  - Improves prediction of onset & degree of separation from smooth surfaces.

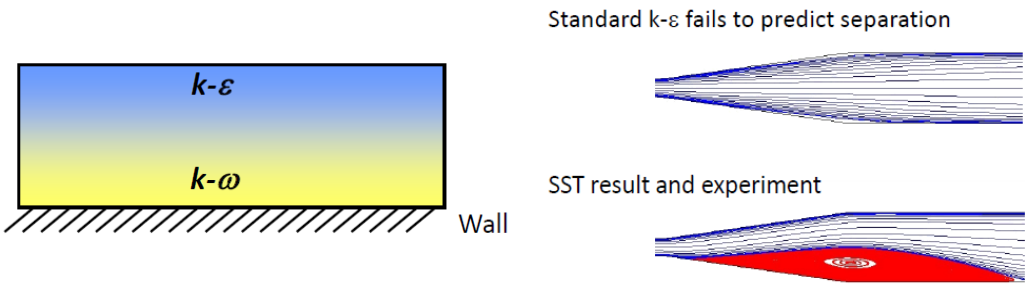

Figure 4.17 Shear Stress Transport Model illustration

- **Simulation parameters and flow boundary conditions:**

  - Uniform velocity of 1 m/s at the inlet, and static pressure at the outlet.
  - Mass flow rate= 0.47 kg/s =7.5 gpm per plate.
  - Re_manifold = 24,000. Re_Channel = 12,000
  - Pressure drop across the plate =2.9KPa
  - Coolant inlet temperature is 350 ℃
  - Fluid temperature rise = 1 ℃
  - Heat generation rate in pebble bed = 5 MW/m^3 =2KW.
  - Maximum bed temperature is 850 ℃

- **Mesh sensitivity**

  Highly-refined mesh with 15,395,173 elements. Very fine grid near the wall to capture turbulence and flow separation. Final results are grid-independent. Convergence controls: RMS 1E-6, and 0.001 Imbalances.

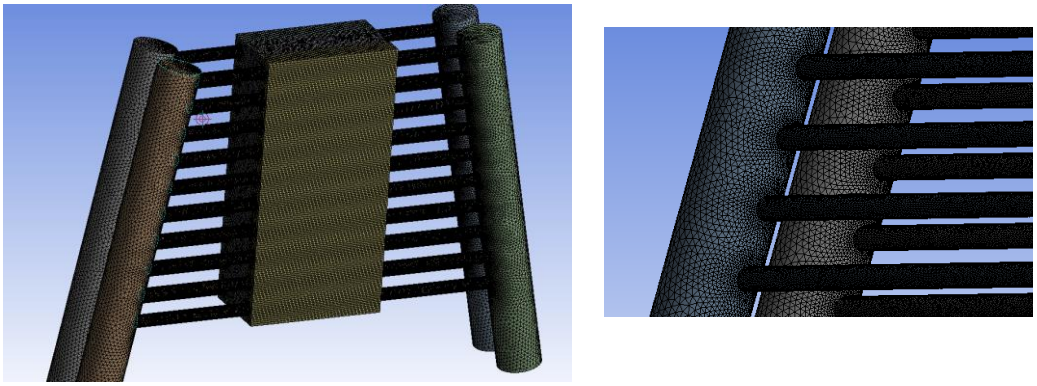

Figure 4.18: Fine mesh resolution of the CFD model

- **Material properties**

Temperature dependent fluid properties (thermal conductivity, density, viscosity, specific heat), in addition to temperature dependent effective bed thermal properties were accounted for using CEL (CFX Expression Language).

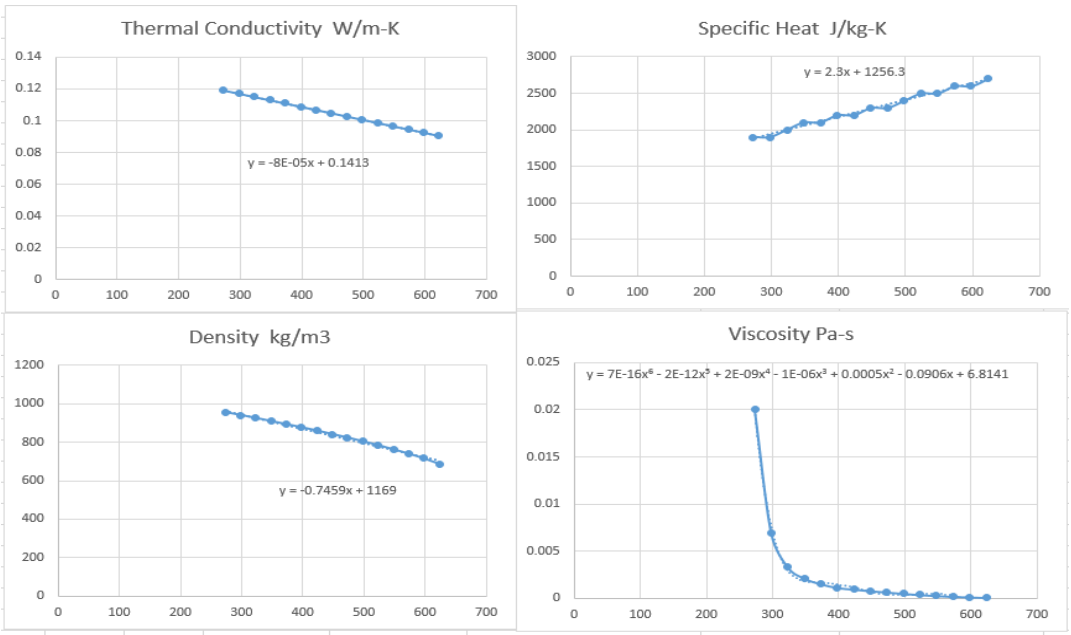

Figure 4.19: Highly temperature dependent coolant properties used in CFD model

- **Solved equations**

Equation	Φ
Continuity	1
X momentum	u
Y momentum	v
Z momentum	w
Energy	h

$$\underbrace{\frac{\partial}{\partial t}\int_V \rho\phi dV}_{\text{Unsteady}} + \underbrace{\oint_A \rho\phi V.dA}_{\text{Convection}} = \underbrace{\oint_A \Gamma_\phi \nabla\phi.dA}_{\text{Diffusion}} + \underbrace{\int_V S_\phi dV}_{\text{Generation}}$$

Heat transfer in the fluid domain is modeled using the following total energy equation:

$$\underbrace{\frac{\partial(\rho h_{tot})}{\partial t} - \frac{\partial p}{\partial t}} + \nabla.(\rho U h_{tot}) = \nabla.(\lambda \nabla T) + \nabla.(U.\tau) + S_E \quad (4.17)$$

Transient Advection Conduction Viscous work Sources

Heat transfer in the solid domain is modeled using the following conduction equation:

$$\frac{\partial(\rho h)}{\partial t} + \nabla.(\rho U_s h) = \nabla.(\lambda \nabla T) + S_E \quad (4.18)$$

Transient Solid motion Conduction Source (internal heat generation q’’’)

In order to quantify the flow uniformity, unified parameters are necessary for the different configurations and optimization strategies. The dimensionless parameter λ_i is used to represent the flow distribution for individual parallel tubes, and it is defined as follows:

$$\lambda_i = \frac{\dot{m}_i}{\dot{m}_T} \quad (4.19)$$

Where $\dot{m}_i$ represents the mass flow rate of the i-th channel (kg s–1), and $\dot{m}_T$ is the total mass flow rate (kg/s); thus, λ_i means the ratio of the flow rate for the i-th channel to the total flow rate.

The standard deviation of the flow rate ratios of the parallel tubes gives a general definition for the non-uniformity φ as:

$$\varphi = \sqrt{\frac{\sum_{i=1}^{N}(\lambda_i - \bar{\lambda})^2}{N}} \quad (4.20)$$

Where $\bar{\lambda} = \frac{\sum_{i=1}^{N} \lambda_i}{N}$ represents the average flow ratio. In the following flow distribution plot shown in Figure 4.20, a larger value of φ reveals a more non-uniform flow distribution.

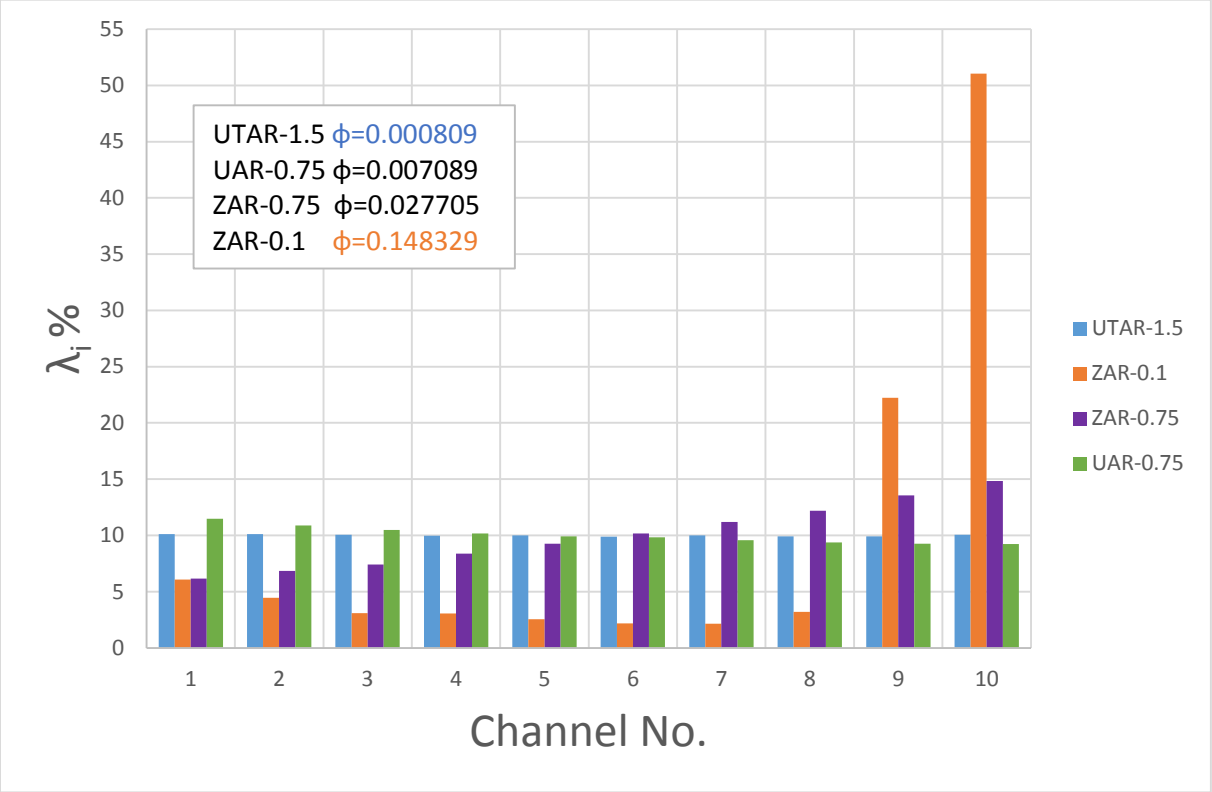

Figure 4.20: Mass flow distribution in the 10 lateral channels for different manifold geometries.

Since the main focus of the first design iteration is to recreate and verify nuclear heating temperature profiles, it is necessary to minimize the cooling plates' surface temperature variation and asymmetry in order to compare with ideal thermal models. For that reason, the uniformity of the coolant flow distribution across the channels has to be near-perfect. After performing several design optimization cases with different geometrical features and flow conditions, the angled U-shaped (parallel flow) manifold with an optimum Area Ratio (AR) of 1.5, defined as the ratio of the wet cross-sectional area of the manifold to the sum total cross-sectional area of individual channels, was found to have the best flow uniformity with a deviation of less than 0.1% across all channels. Additionally, the angled manifold equalizes the flow resistance across the channels

enabling the flow to reach the upper most channels with near-equal mass flow rates, which maintains the surface temperature within ΔT of only 1.9 °C compared to 28 °C for the base case.

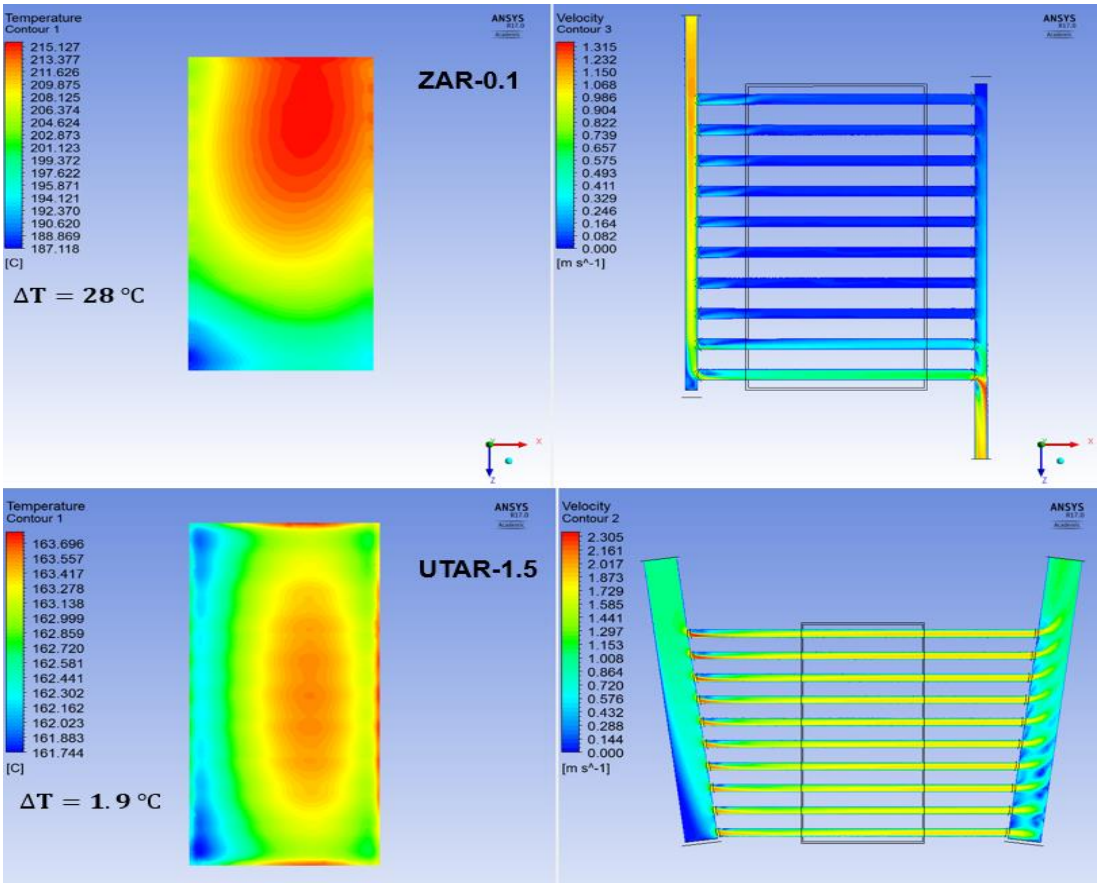

Figure 4.21: Surface temperature and velocity distribution comparison between the original design (top) and the optimized design (bottom) showing substantial improvements in flow uniformity and plate surface temperature deviation.

4.2.3. Test box construction/fabrication and assembly

TESOMEX 1.0 design consists of 1.5 cm thick copper plates with 20 gun-drilled 7 mm circular channels (Figure 4.22). The plates are vacuum brazed onto the 1.5 mm wall thick steel

box which contains the pebbles. Varying-length steel pipes are welded to the 7.5 degrees angled manifold of ID 26.6 mm.

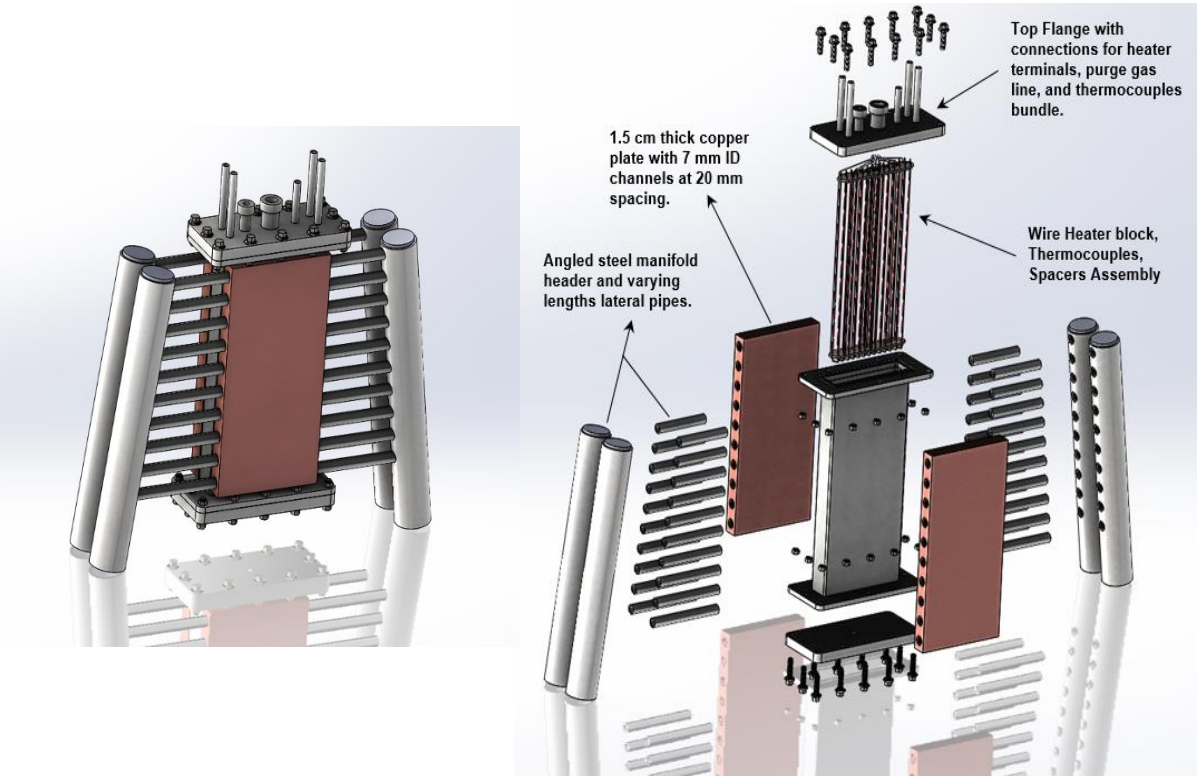

Figure 4.22: CAD illustration of TESOMEX 1.0 Assembly (left) and components break down (right).

12 single-point and one multi-point type-K thermocouple bundles are inserted from the top flange and passed through the ceramic spacer for accurate placement of measurement points. The NiChrome heater terminals are crimped on a steel tube to make the cold ends, and covered by Alumina ceramic tubing for electrical insulation. All tube connections are equipped with ultra torr fittings for vacuum sealing. Two Y-shaped connections are welded onto the manifolds to make one inlet/outlet lines for cooling loop assembly.

Heater block/Thermocouples/Flange Assembly

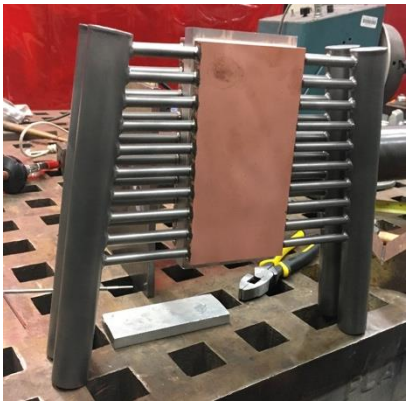

Manifolds welding and final assembly

Figure 4.23: Test box welding and assembly of internal components.

4.2.4 Ancillary systems and cooling loop design

- **Thermal fluid loop**

A Paratherm hot and cold oil loops are connected to the test article to provide adequate boundary conditions. The maximum operating temperature of the oil is 371 °C. Ceramic plates of appropriate thickness and thermal conductivity should be considered if higher temperature boundary conditions are needed. The thermal fluid system consists of the following basic components:

(1) A pump that circulates the (2) heat transfer fluid though an (3) insulated piping system to a (4) heater that raises the fluid's temperature to a desired value to provide adequate boundary conditions at the test article or process equipment. An (5) expansion tank is needed to allow for the expansion and contraction of the fluid during heating and cooling cycles respectively. In addition to Pressure Safety Valves, Control Valves, Catch Tanks, drains and vents.

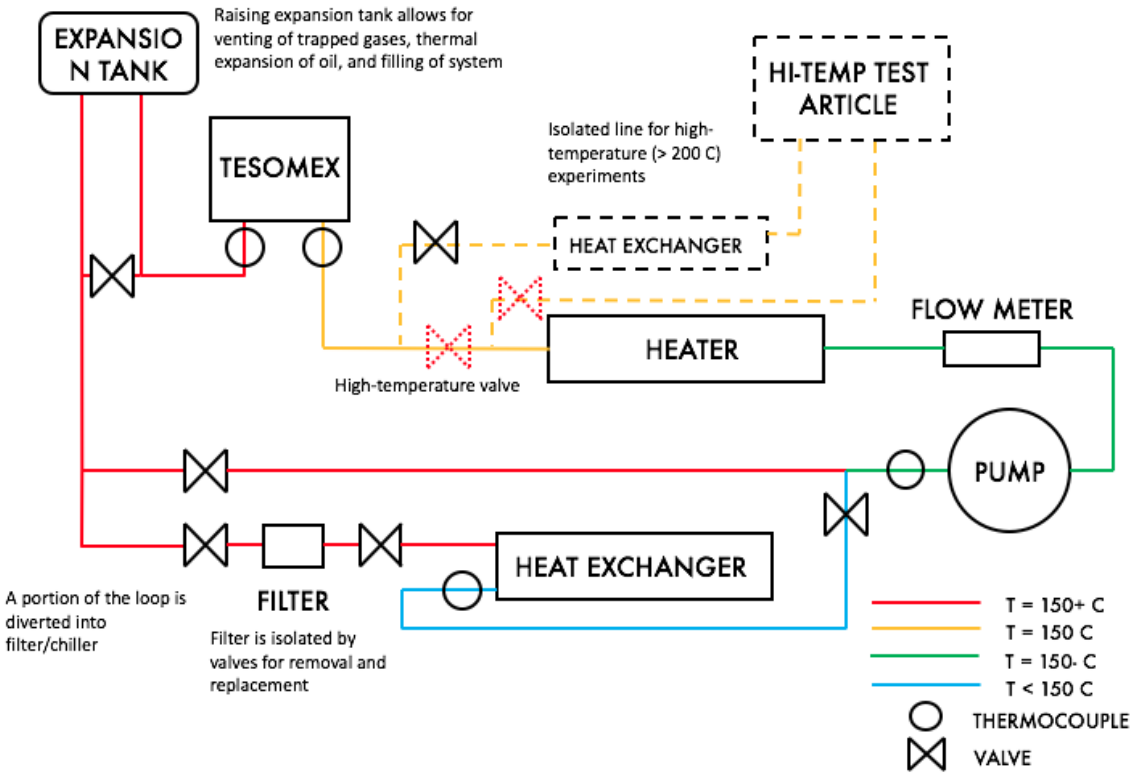

Figure 4.24: Cooling loop design showing the main components and pipes routing.

Appendix E provides further details on the cooling loop design considerations, start-up/shut-down, and safety procedures.

- **Control tool**

LabVIEW data monitoring and acquisition, as well as power and flow control algorithms will be developed for the test setup and ancillary system components. The control tool aids in taking accurate measurements, efficiently controlling operating parameters, and designing power cycles that reproduce ITER pulses.

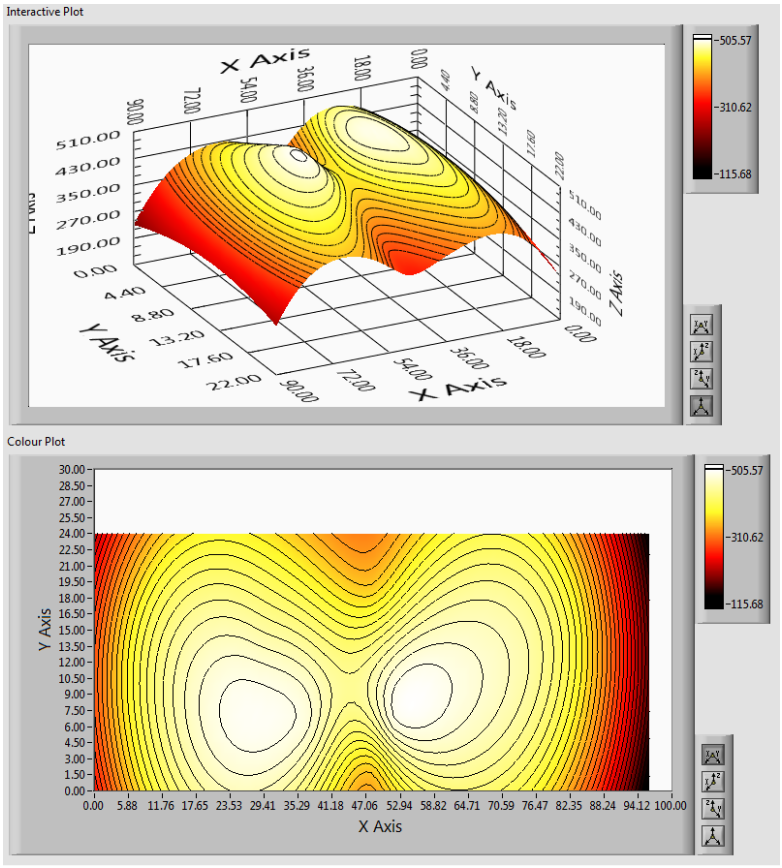

Figure 4.25: Interactive interpolation temperature contour plots incorporated in LabVIEW code.

4.2.5 TESOMEX 1.0 analysis of preliminary thermal map results

After fully assembling the test article, connecting the thermocouples, and wiring the heater terminals to the two power supply units for idependent heater blocks power control, the internals were inserted into the box cavity. Next, the pebbles filling procedure consisted of pouring the

pebbles from the top filling hole and using mechanically assisted vibration table to reach the theoretical packing fraction of 62%.

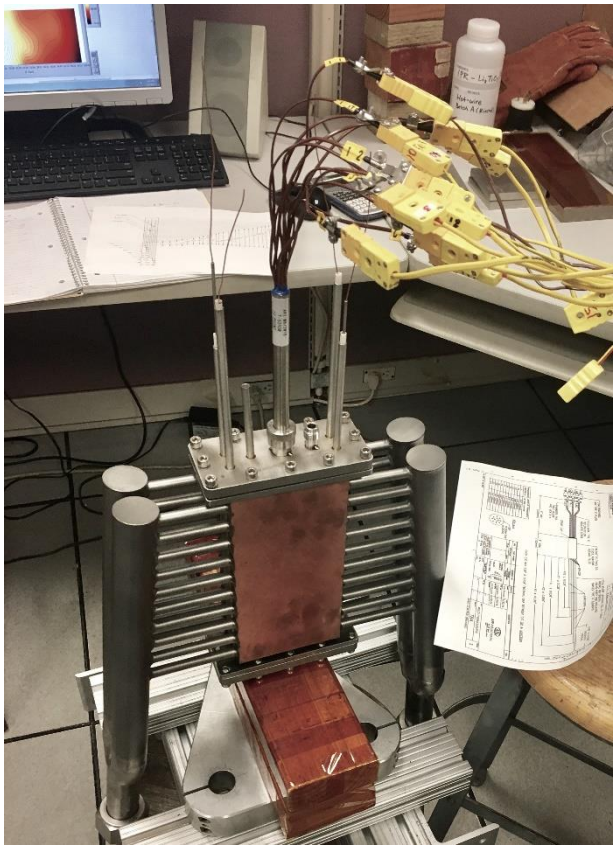

Figure 4.26: Assembled test article 1st run with Pebble bed packing 62%.

The power units were turned on at 150 W starting power, then increased gradually to reach a total power of 920 W, which corresponds to a maximum bed temperature of 580 °C. It is evident from Figure 4.27 how the slopes of the temperature curves follow the heating power levels adjustment pattern. During the first run, only air cooling and active fan cooling were used since the goal was not to reach the highest temperatures possible, but to test the integrity of the heater blocks and

circuits wiring, practice the assembly and operation procedure, as well as observe the behavior of the pebbles and search for any signs of degradation.

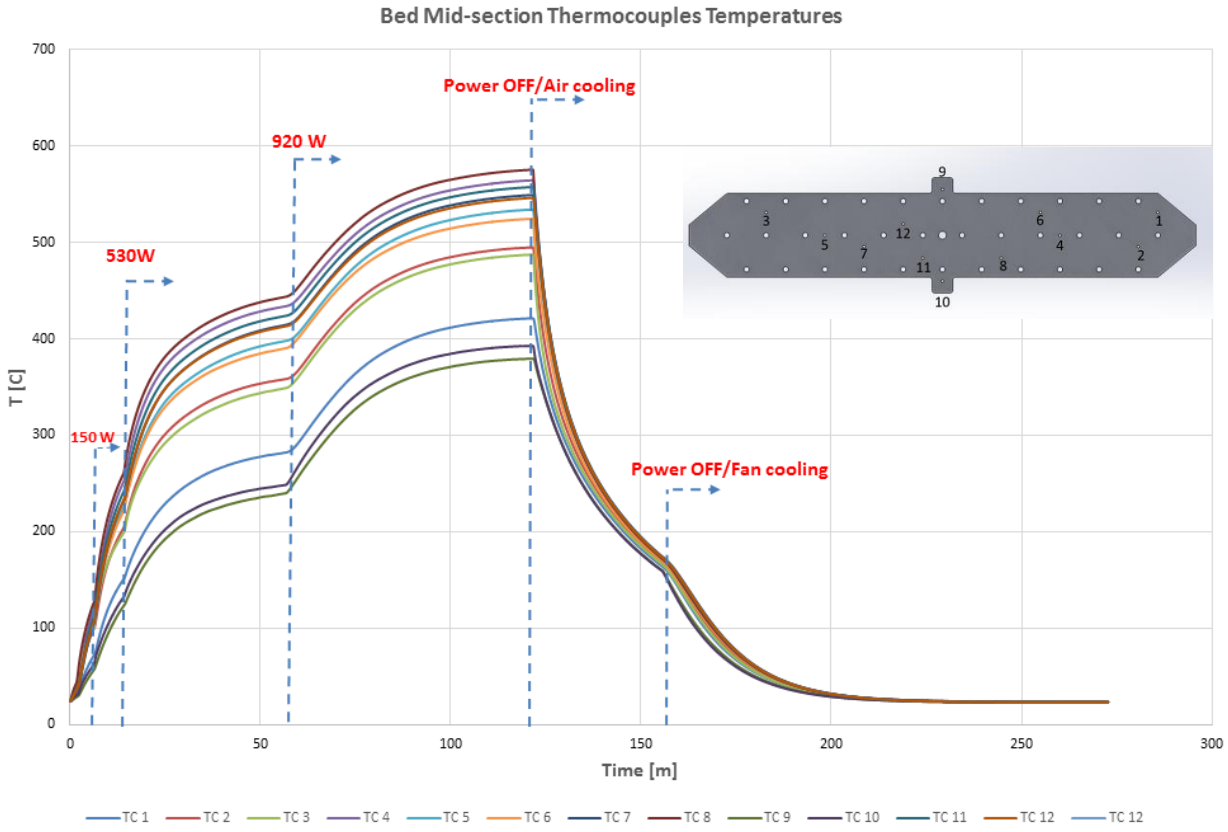

Figure 4.27. 1st run thermocouples temperature evolution showing matching patterns of active heating/cooling.

The final temperature contours of the 1st run shown in Figure 4.28 reflect promising results of recreating the volumetirc heating temperature profile representative of the narrow breeder cells in ceramic breeder blanket modules. The minimum and maximum temperatures reached without connecting the thermal fluid loop were 250 and 580 C, respectively. The next step is to test the oil loop to incorporate the relevant temperature boundary conditions and continue to investigate

temperature profiles and evolution under various flow conditions, before proceeding to TESOMEX 2.0.

Figure 4.28: final 2D and 3D temperature contours of the 1st TESOMEX 1.0 run, before turning off the power, indicating promising recreation of nuclear heating temperature distribution.

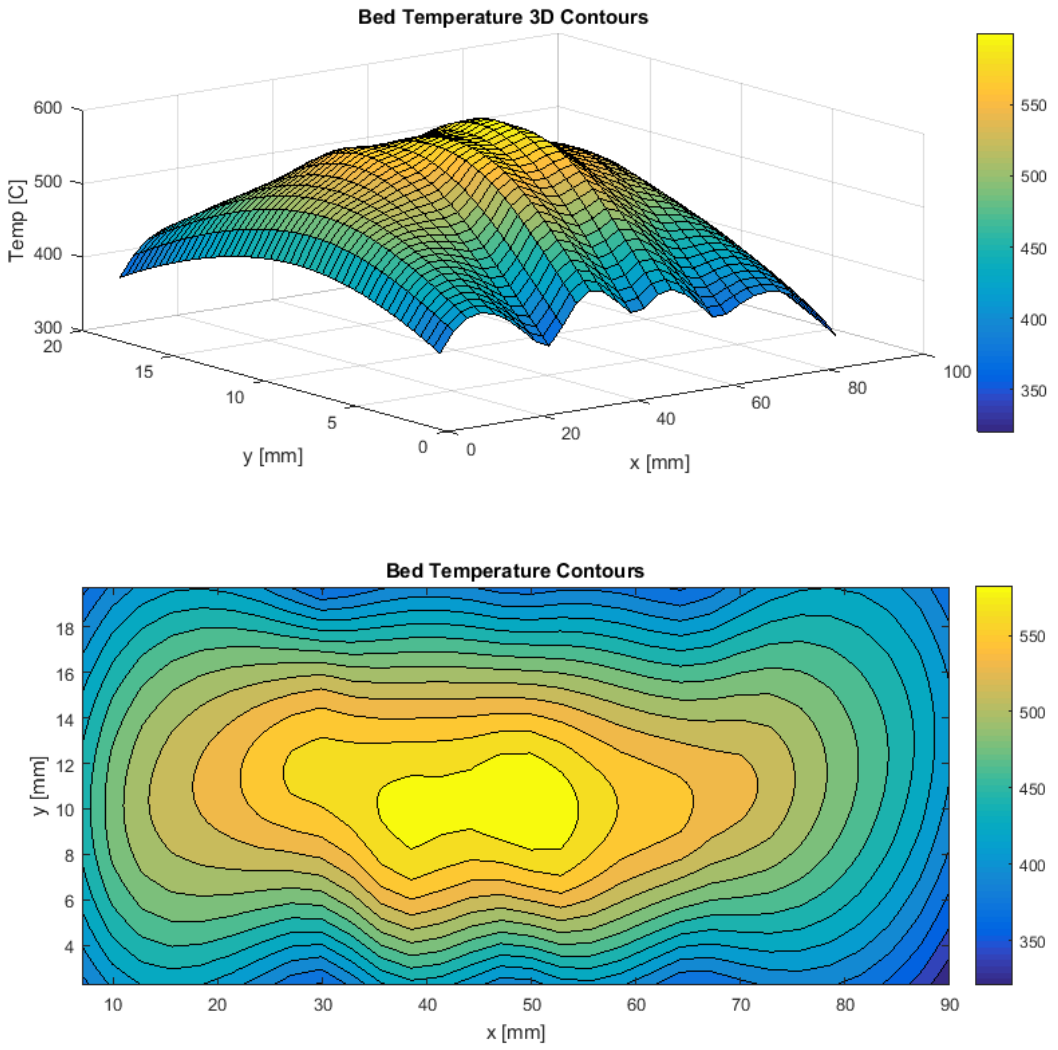

The interactive LabVIEW code utilizes a MATLAB-based interpolation scheme to represent the intermeidate temperatures between the thermocouples measurment points at the mid-section of the pebble bed.

4.3. TESOMEX 2.0 thermo-mechanical relevance to prototypical solid breeder blankets

To reiterate, the main objectives of the 2nd design iteration is to: a) reproduce a more relevant thermo-mechanical behavior characteristic of the interaction between the pebbles and the structural material under prototypical mechanical and thermal boundary conditions. b) Benchmark the most up-to-date FEM models that can then be extrapolated to add more complexities. c) Investigate the effects of pre-compaction/pre-conditioning on thermo-mechanical evolution. Therefore, the test article and manifold design have been upgraded to reflect a more relevant design mimicking the operation of a ceramic breeder unit cell. Moreover, state-of-the-art stress measurement techniques were investigated in order to be able to collect stress distribution maps that capture the effects and evolution of all the thermo-mechanical modes discussed in previous chapters.

4.3.1 Coolant manifold and testbox design upgrade

After finalizing the proof of volumetric heating stage, more emphasis is laid on the realistic thermomechanical response of prototypical solid breeder fusion blankets. To that end, additional materials selection and space restrictions were taken into consideration throughout the design process of TESOMEX 2.0. Nonetheless, the manifold design was optimized (see Figure 4.29) to have a highly uniform/symmetric flow distribution in order to avoid no-flow situations in certain channels that may lead to undesirable effects such as the formation of hot spots exceeding the temperature limit of the structural material and/or the sintering temperature of the pebbles.

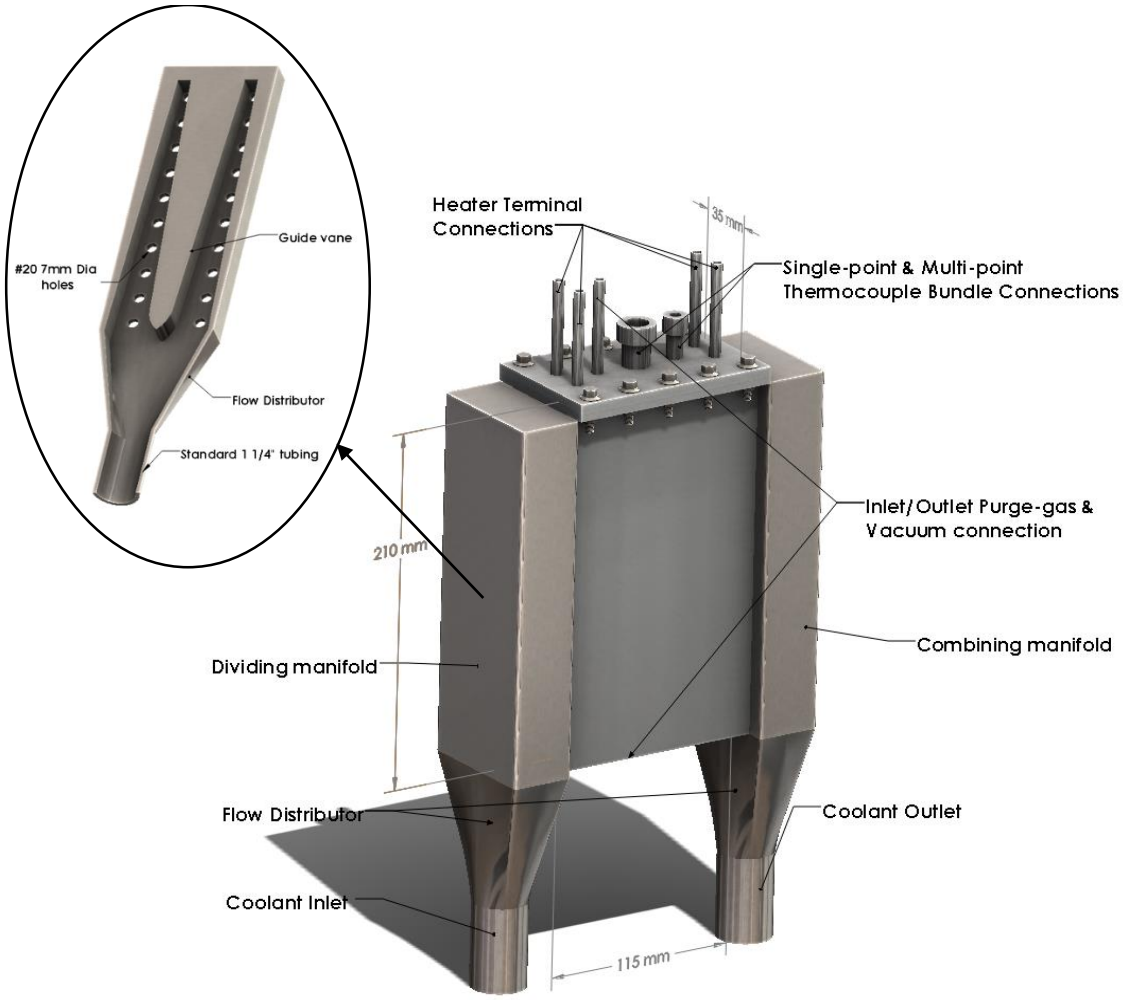

Figure 4.29 Construction of TESOMEX 2.0 with the tapered manifold

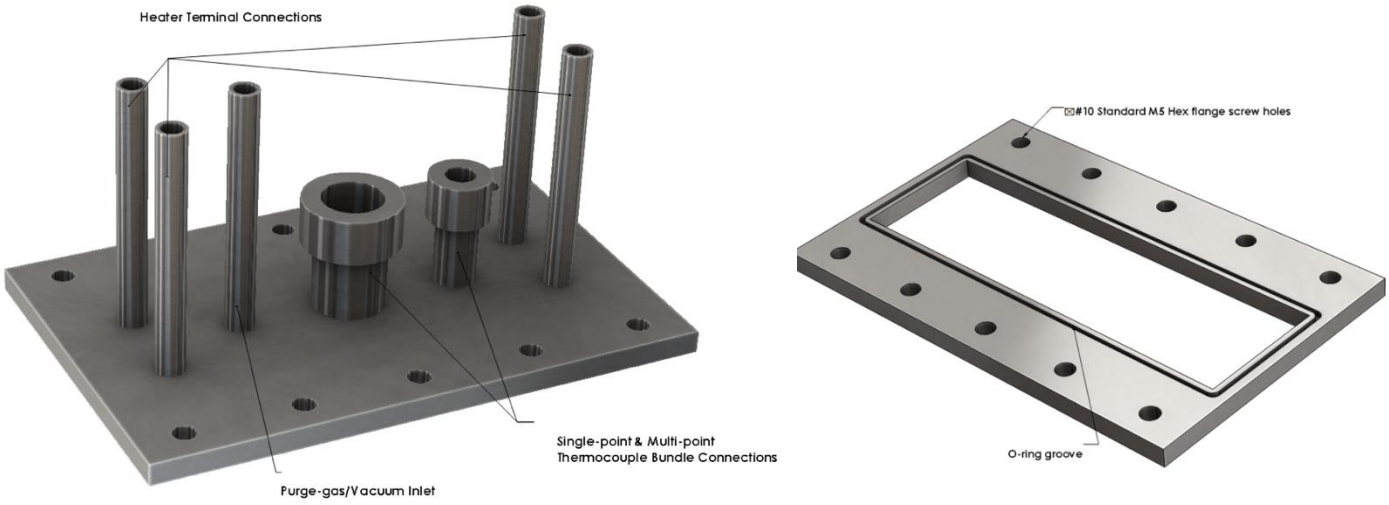

Figure 4.30: Top flange design showing the vacuum-sealed connection and O-ring groove.

- The top flange consists of two parts. A welded part, and a bolted part for the thermocouples, heater terminals, and purge-gas line connections.
- The welded part of the flange will be welded on the top of the box with the O-ring groove facing upwards.
- The dimensions of the connections are finalized based on the available thermocouple bundle sizes, and the ceramic heater wire insulators.

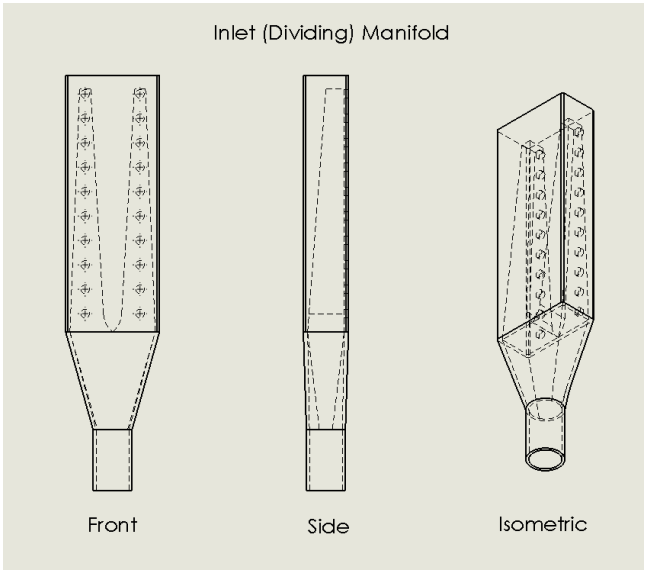

Figure 4.31: engineering drawing and mid-sectional view of the test box showing the internal design of the manifold and flow channel paths.

- The tapered manifold gradually increases the fluid velocity in the flow direction in order to:
  - Compensate for the reduction in momentum due to friction and gravity, allowing the fluid to reach the upper channels more evenly.
  - Reduce localized eddies and unsteady flow patterns in the manifold allowing a more uniform flow distribution among the channels as show in Figure 4.32.
  - Balance the increase in static pressure in the flow direction (pressure recovery).
- The increaser/distributor avoids the formation of karman vortex street caused by the sudden transition from circular to rectangular cross-section, hence significantly reduces entrance region effects and vortex shedding (a repeating pattern of swirling vortices caused by the unsteady separation of flow).

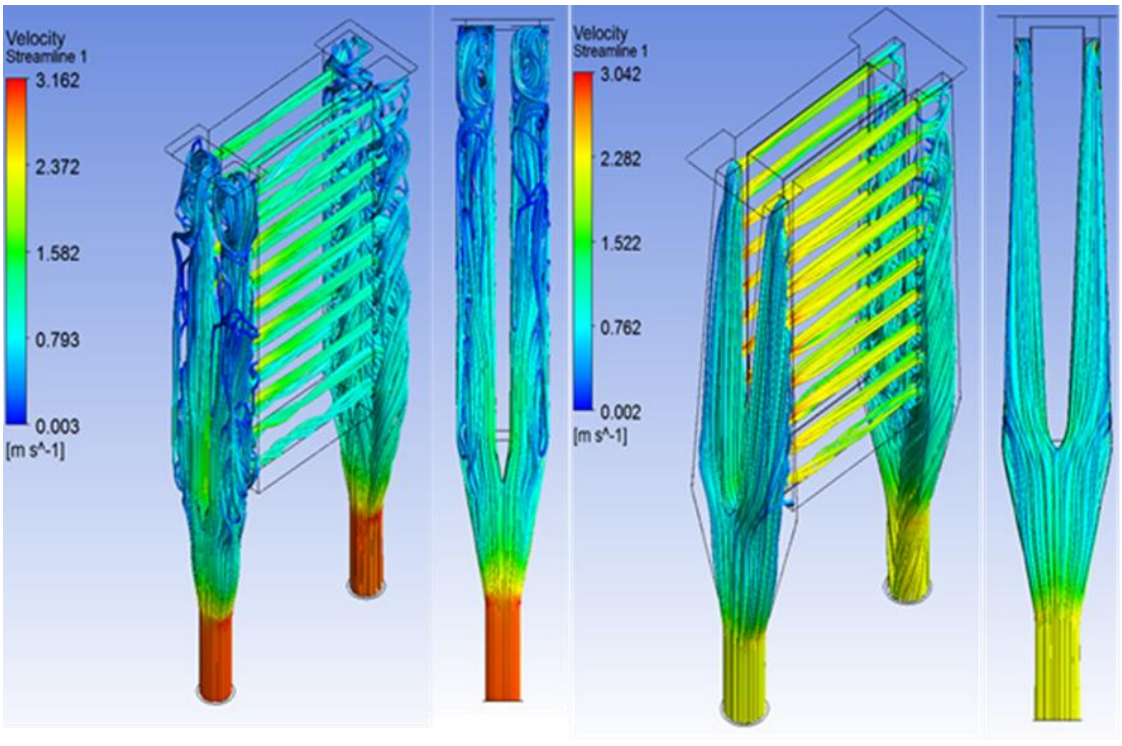

Figure 4.32: TESOMEX 2.0 velocity streamlines of basic design (left) and enhanced design (right) showing more uniform flow patterns for the flow

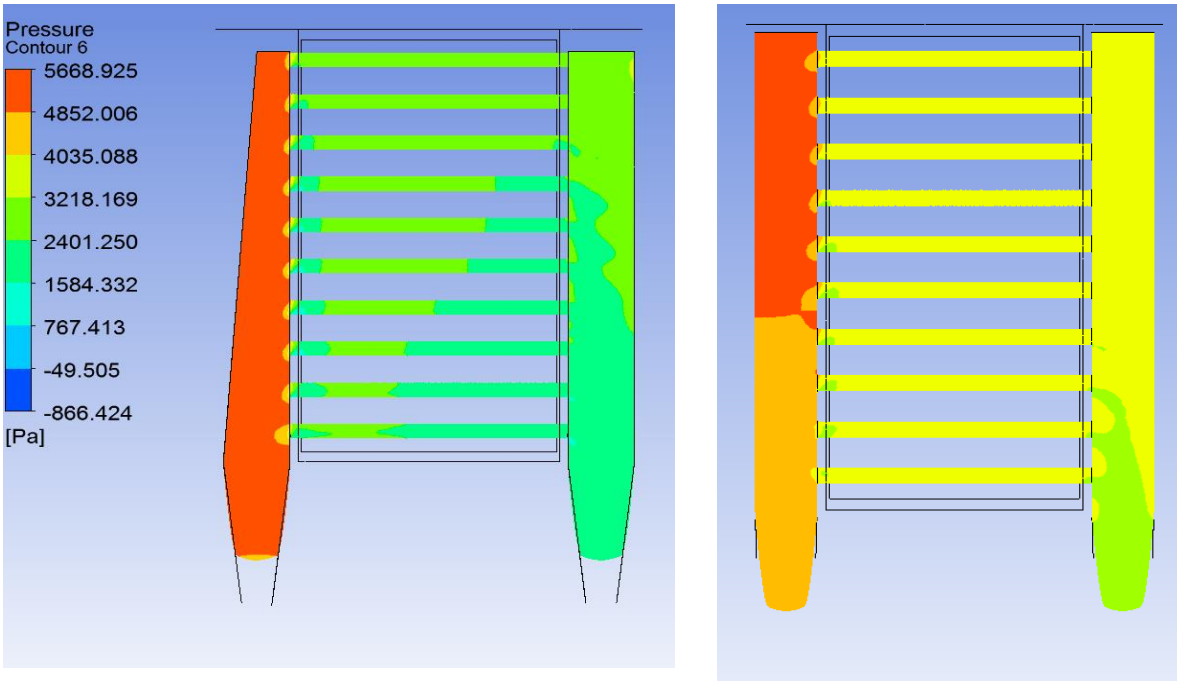

Figure 4.33: Static pressure contours of optimized design (left) and original design (right) showing more uniform flow distribution for the optimized design.

An important feature of TESOMEX 2.0 is to make sure that the percentage of pebbles above creep temperature is close enough to what is expected to occur in a real blanket. The CFD temperature results highlighted in Figure 4.34 illustrate an acceptable volume of pebbles sitting at creep relevant temperatures, which will allow for analyzing the effect of this particular mode of bed deformation on the thermomechanical stability and evolution of the pebble bed operation.

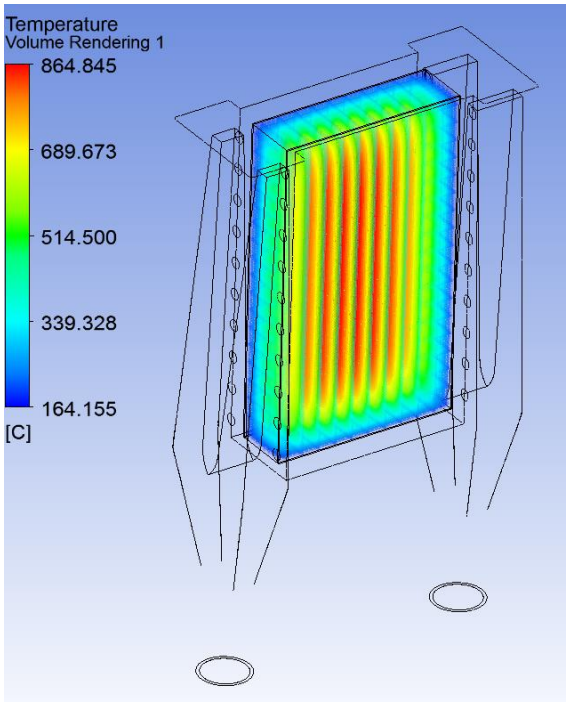

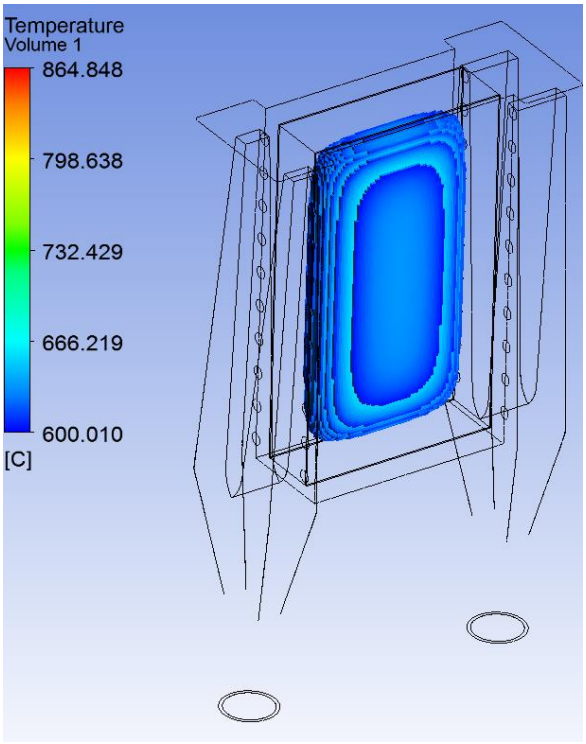

Volume rendering of the temperature distribution in the pebble bed.

Volume % of pebbles within 600 ℃ - 860 ℃ = 45%

Figure 4.34: emphasizing the importance of simulating the relevant volumetric temperature profiles and high volume of pebbles at creep relevant temperatures.

In a similar fashion to the flow distribution analysis employed in the first version of the design, TESOMEX 2.0 CFD analysis shows high levels of flow uniformity as illustrated in Figure 4.35. This will aid in avoiding temperature abnormalities, such as the formation of localized hot zones that do not represent the real behavior under prototypical nuclear heating.

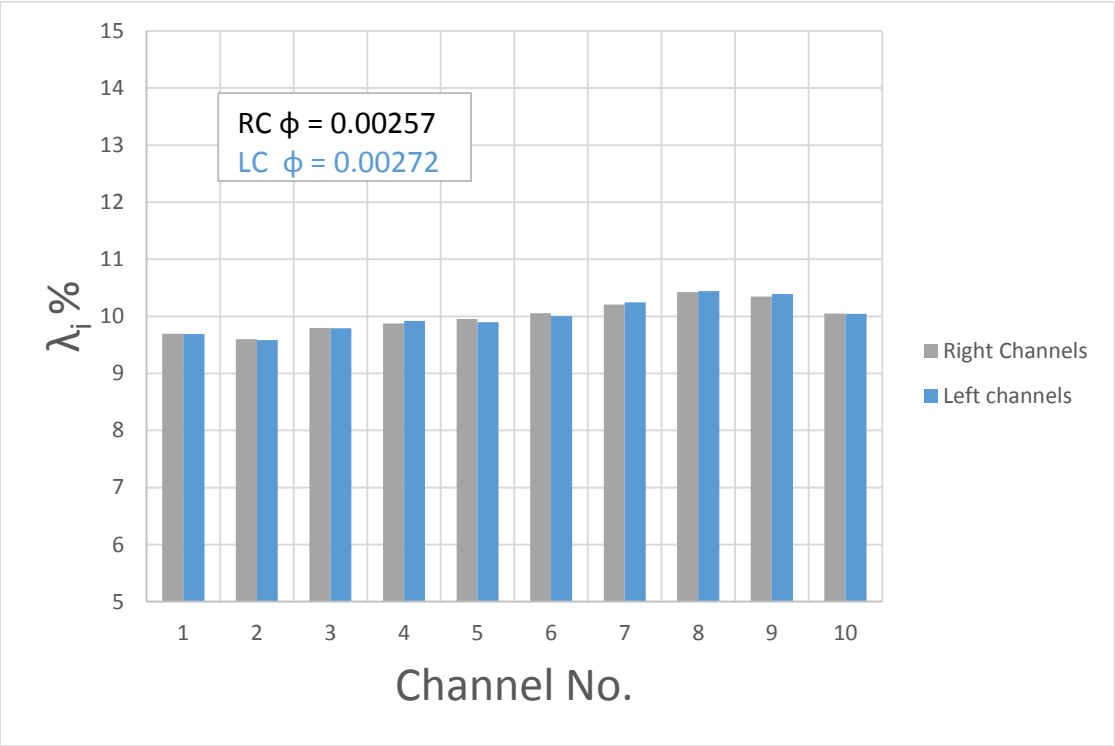

Figure 4.35: CFD results of mass flow channels distribution showing high uniformity

4.3.2 Heating technique updated approach

Wire heater drawbacks**:**

Although the wire heating technique successfully reproduced the relevant volumetric heating profiles that it was designed to mimic, it was rendered unsuitable for the purposes of our experiment for the following reasons:

1- In order to keep packing disturbance to a minimum, we had to use fine wires, which were not able to withstand the high stresses and rapid heat transients for a long enough period of time that would allow us to reliably study the thermo-mechanical evolution.
2- Minimizing disturbance also prevented us from using an additional layer of insulation around the wires, which significantly increases the risk of short circuits.
3- To reach the desired temperatures, a large amount of power needs to be dissipated in wires with small surface area. This causes the surface heat flux to go over the safe limits and creates zones of localized heat that causes the pebble to sinter into solid blocks as shown in Figure 4.36.
4- Due to the chemical composition of the wires (Nickel/Chromium), there is evidence of chemical reactions taking place at the higher bed temperatures which ends up closing the interconnected porosity and inhibiting Tritium release.
5- To simulate the relevant temperature profiles, the wires have to be distributed in a hexagonal structure all over the bed. This prevents us from reaching adequate packing fraction with or without assisted vibration techniques. The highest packing reached with the wires was around 54%.

As a result, this technique has been put on a diagnostic hold as another inherently more reliable alternative is being tested.

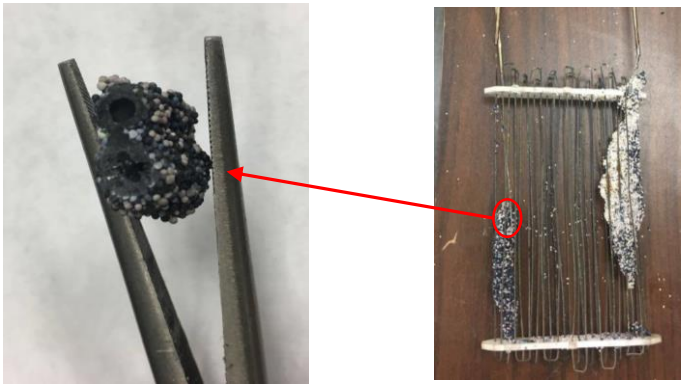

Figure 4.36 Pebbles sintered/melted around the wires at local high-temp zones

New Heating Approach Results and Analysis**:**

The new proposed approach is to use plate or rod heaters to replace the wires and still simulate relevant temperature gradients. The heat direction will still be volumetric in the sense that it is generated in the pebble bed and dissipated at the cooling walls, but the temperature profiles will deviate to an extent from the realistic scenario. The improved reliability of the alternative heating approach allows us to run multiple consecutive cycles while capturing the physics of interest. Moreover, the new heaters are a) chemically inert, which reduces the risks of reacting with the pebbles, b) electrically insulated, which prevents short circuits, c) placed in a limited space in the bed, which allows us to reach theoretical packing fractions, and d) allow for reliable high-temperature operation thanks to their larger surface area. Figure 4.37 presents various heating alternatives that allow for much better bed packing relative to the wires case, more reliable/safe operation, while achieving relevant temperature profiles and safely extracting useful contact pressure data.

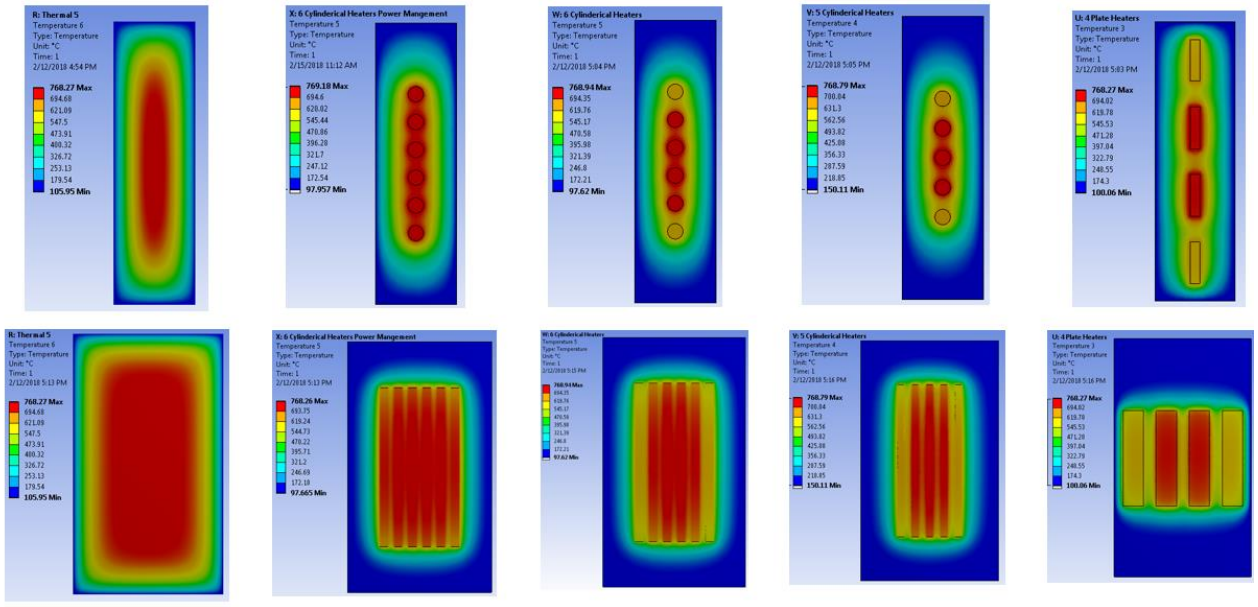

Figure 4.37. Temperature profile comparison for different design cases showing the configuration with 6 rod heaters of 6 mm diameter and 5 mm spacing resulting in the closest match to that of the nuclear profile

In order to reach the simulated temperature profile experimentally, a power optimization problem had to be solved as shown in Figure 4.38. For the base case, all the heaters were energized at the same power level to reach a maximum bed temperature of 768 ˚C. Scheme A independently controls the center pair and the two top and bottom pairs resulting in two variable power levels. Scheme B, however, adds a third variable power input which allows for a finer resolution of gradually increasing the power to compensate for the temperature drop as the heaters move away from the center of the bed. The three different levels were optimized in an ANSYS iterative parametric study that outputs the heaters power ratio that yields the temperature profile closest to the volumetric distribution without exceeding a specified maximum bed temperature.

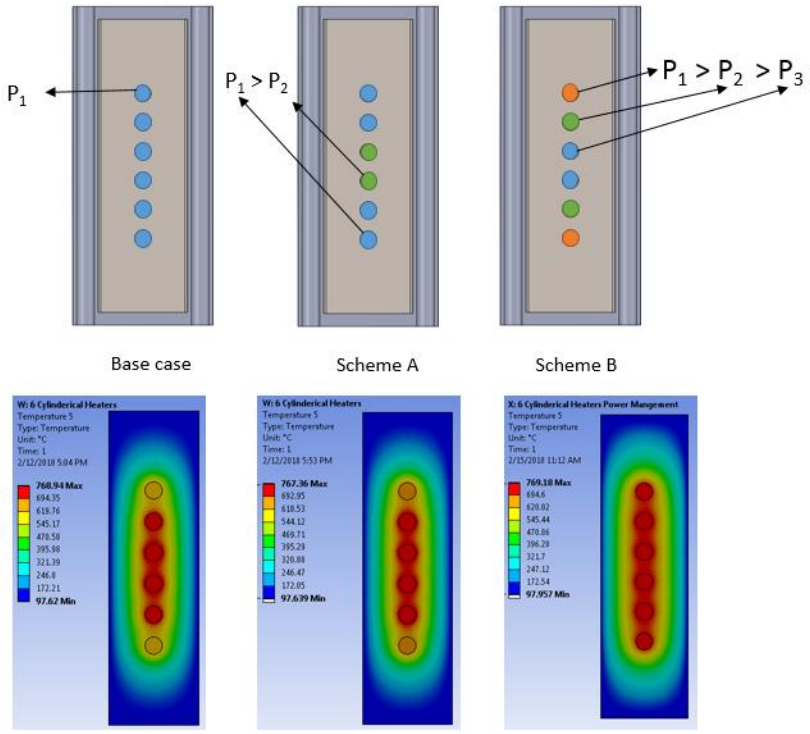

Figure 4.38. Power Optimization Scheme

Multiple thermal simulations were performed to estimate the percentage of deviation from the nuclear heating profile. Figure 4.39 illustrates such the estimated error.

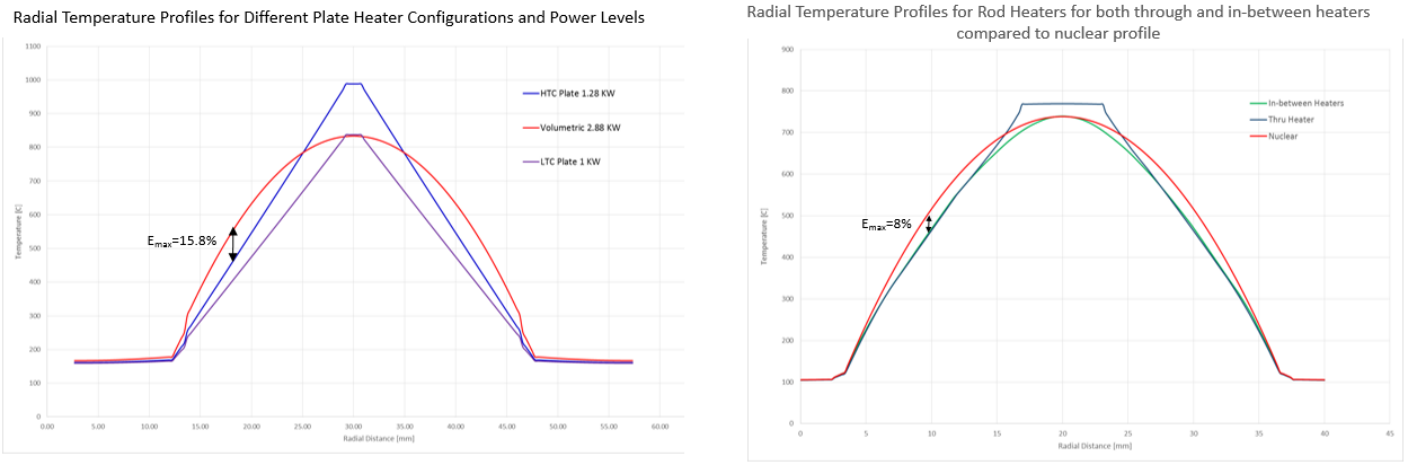

Figure 4.39. Radial temperature profile comparison for rod and plate heaters benchmarked against nuclear heating temperature profile

For the plate configuration, in the effective region, the point at which the maximum temperature deviation from the nuclear profile occurs for the high power case has a E_{max}=15.8% error. All other points have less error. The maximum error in the rod heaters assembly case, however, was reduced to E_{max}= 8% without the need to sacrifice a large percentage of the bed at much higher temperatures.

Heater assemblies and test article preparation:

Both heaters' fixtures were designed and fabricated to accurately position and fix the heaters assembly in the desired location. The packing fraction for both heaters ranged from 61% to 63.5% which is a significant improvement over the wires case 52%. Each configuration had its own pros and cons: The plate heater assembly has the advantage of high operating temperature and wattage (up to 1200 °C). However, the heated length is only 8 cm and the temperature profile deviates from the nuclear temperature profile more than that of the rod heaters. Another disadvantage is that the heaters spacing is restricted due to the top ceramic base protecting the wires. For the rod heater assembly, the length of the heated zone is 17.6 cm which results in a more relevant temperature profile.

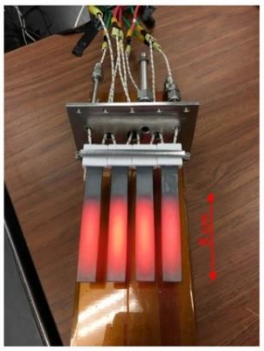

(a)

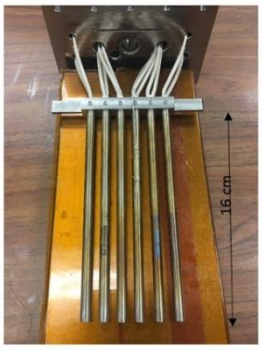

(b)

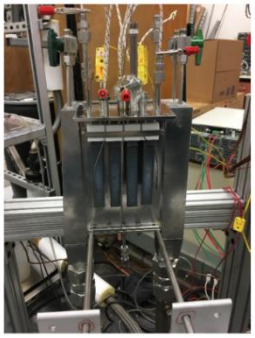

(c)

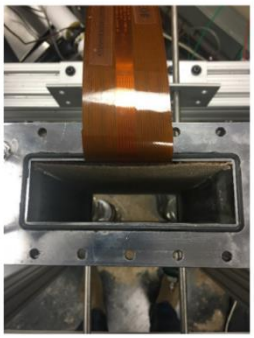

(d)

Figure 4.40 Plate heater testing (a), rod heater assembly and dimensions (b), Setting up the test article and positioning the heaters assembly and wiring (c), and tactile pressure sensor protected by two layers of Silica cloth and taped to the coolant wall using a double-sided Kapton tape with maximum operating temperature up to 260 °C (d).

After testing the plate heaters and rod heaters in the pebble bed sample at a maximum bed temperature of 820 °C, the Silica Nitride plate heaters started reacting with the pebbles and formed black sold blocks that broke the heaters and degraded the pebbles as seen in Figure 4.41 (right). On the other hand, the rod heaters made out of Inconel were able to resist corrosion, oxidation, and reactions with pebbles at elevated temperatures up to 860 °C. Therefore, the rod heaters with the optimized power scheme were chosen as the primary heating configuration.

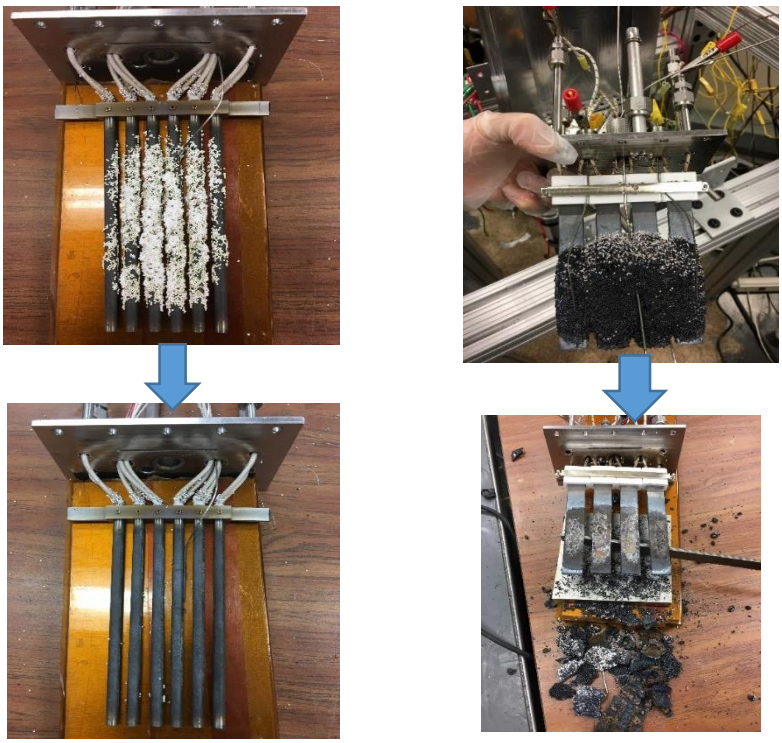

Figure 4.41. Rod heaters: pebbles came off after scraping by hand in less than a minute with no color change (left). Plate heaters: Severe pebbles sintering into large chunks that were only removed by hammering and thermal cycling. Significant damage to the surface of the heaters was observed (right).

4.3.3 Employing state-of-the-art tactile pressure mapping technique for stress analysis

In efforts to obtain a more comprehensive picture of the stress distribution and evolution with time and thermal cycling inside the pebble bed, a Tactile Pressure Mapping system will be utilized (Figure 4.42 and 4.43). The grid-based tactile sensor technology enables stress measurements at a large number of points in close proximity, thus allowing for a realistic normal stress distribution. The technology was originally developed at MIT's Artificial Intelligence Laboratory, stimulated by dental application. A firm by the name of TEKSCAN has enhanced the product and its utilization for engineering applications[35]. The working principle is quite simple: the matrix-based sensors consist of a piezoresistive material sandwiched between two pieces of flexible polyester, with printed silver conductors on each half. The silver traces provide a conductive track for the scanning electronics to transmit a signal through the piezoresistive ink. As pressure is applied to the sensing area, the electrical resistance in the ink changes in inverse proportion to the applied normal force as shown in Figure 4.44. The scanning electronics collects the analog data and converts it into a digital signal, which is then transmitted to a PC.

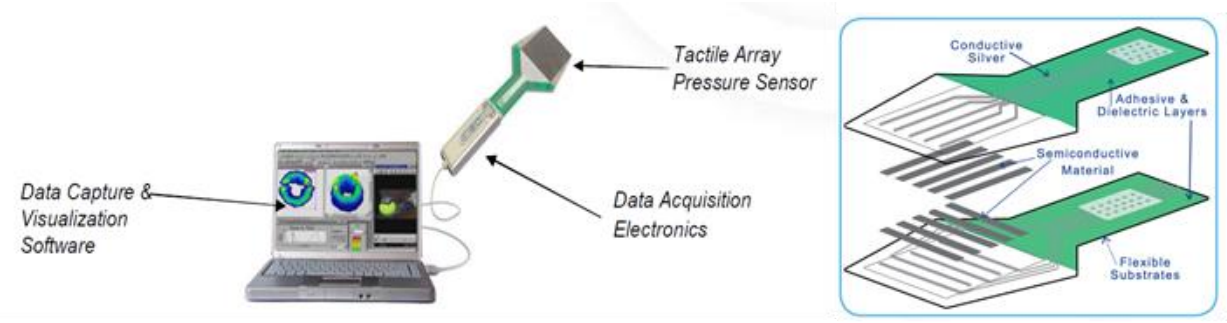

Figure 4.42 Tactile Pressure Sensor Construction

Some of the few advantages that this technology has to offer includes the following:

- The entire sensing area can be scanned at speeds as high as 20 kHz.
- Pressure range up to 207 MPa.
- Sensors are less than 0.1 mm thick, and typically have 2,000 sensing elements.
- The scanning software provides an in-situ real-time window showing the activity in the sensor area while generating various types of graphs showing force, pressure, contact area, and other parameters versus time or position on the sensor.
- Employing this system will allow us to study the stress distribution in the pebble bed and its evolution with time and position, in order to capture the effects of thermal cycling, plastic rearrangement and creep deformation.

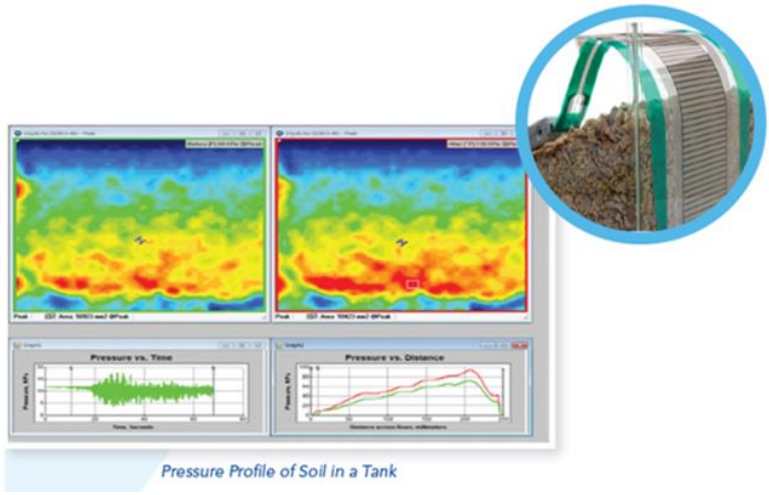

Figure 4.43 Tactile pressure sensor's example stress distribution.

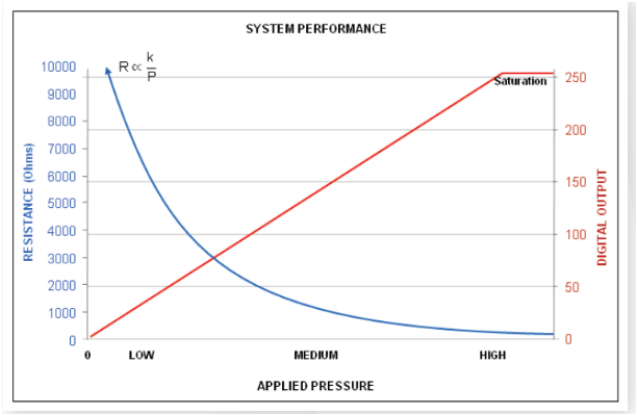

Figure 4.44 Tactile pressure sensor's resistance vs applied pressure dependence

The calibration process was carried out on the uni-axial compression Zwick machine. It was critical to use a relevant pressure loading range, temperature conditions, and materials expected to occur in the experiments. Therefore, a pebble bed sample was prepared along with a flexible Silica sheet for thermal protection, at relevant furnace temperatures and loading conditions. The measured forces/pressures on the sensor's software were compared to the load cell measurements and calibration curves were created with a maximum deviation of 2% error across

the pressure range of 0 to 4 MPa. Figure 4.45 shows an image of the sample setup prepared for calibration.

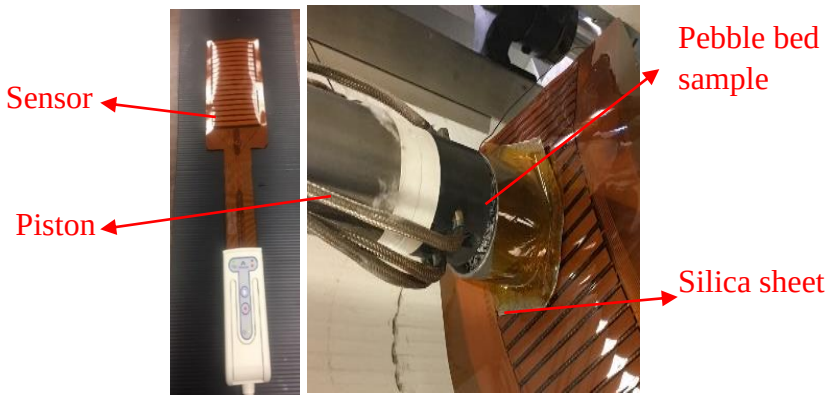

Figure 4.45 Zwick calibration at expected temperatures and stress levels with Silica sheet and pebbles sample

Unlike traditionally used strain gauges which generally provide insignificant information in pebble bed mock-up experiments, the tactile pressure sensor allows for obtaining a complete picture of real-time/in-situ data of stress distribution and evolution with thermal cycling inside the pebble bed.

Chapter 5

5. Experimental Results & Discussion

5.1. Experimental campaigns

After assembling the heaters and thermocouples (at the center of the bed and radial locations at 0,5,10,18 mm away from the heater), the sensor was placed inside the box at the interface between the coolant wall and pebbles and topped with a thin Silica cloth as a thermal shield to protect the sensor from operating above its maximum temperature of 200 °C – which is the major disadvantage of the sensor that only allows normal pressure measurements at the coolant wall where the temperatures are within the safe operating limits. Next, various experimental campaigns were launched. The first series aimed at testing the power levels necessary to reach different maximum bed temperatures and their corresponding wall temperatures that maintain the safe operation of the pressure sensor. The second series of experiments aimed to analyze the thermo-mechanical evolution using the temperature measurements and sensor's real-time output under thermal cycling conditions that mimic ITER pulses. The third campaign was designed to study and isolate the effects of creep under continuous long-term operation. Finally, the fourth wave of experiments tested the effect of adding more pebbles post thermal cycling, or pre-conditioning, in order to improve the packing density and thermo-mechanical stability of the bed.

5.2. Thermal cycling experiments for pulsed operation

Figure 5.1 shows the temperature as well as the stresses cyclical evolution for the first run. The maximum bed temperature reached was 410 °C. As expected, the contact pressure drops after the initial cycle as a result of bed plasticity and pebbles rearrangement. It is worth noting that the peak contact pressure region is shifted towards the bottom of the bed since the bed is more densely packed at the bottom under the effect of gravity.

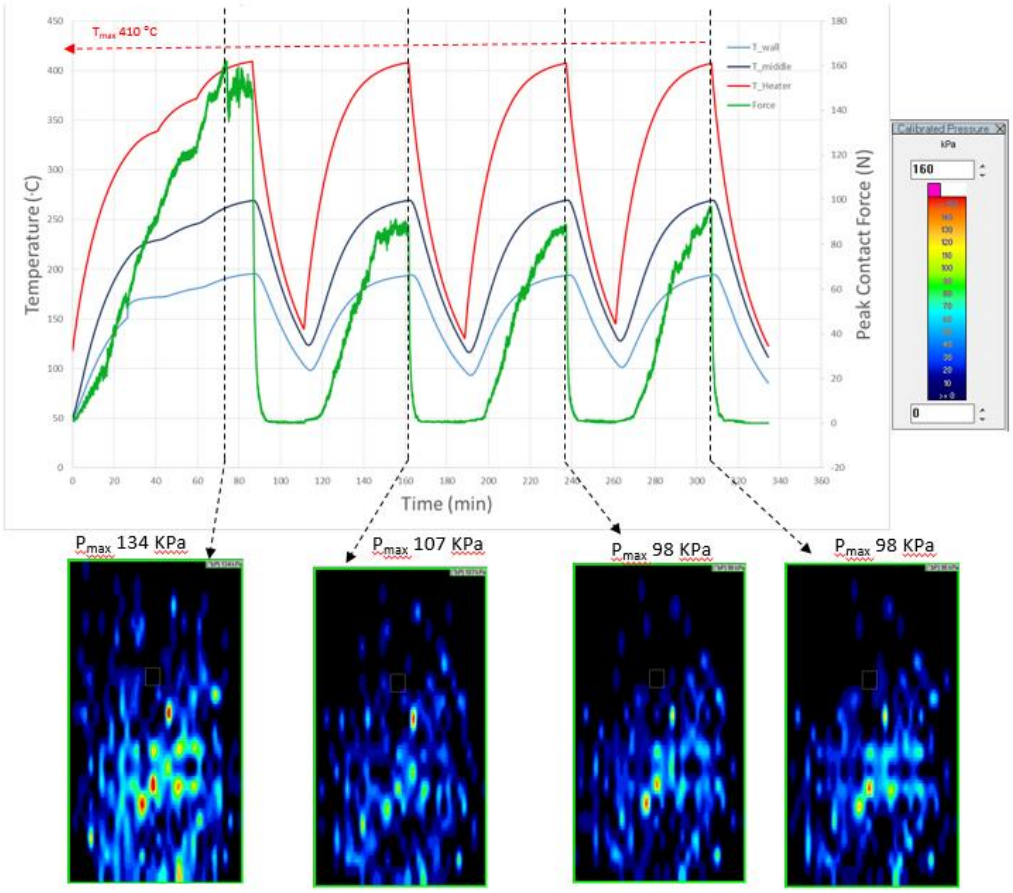

Figure 5.1 Temperature and pressure evolution for T_{max} = 410 ˚C.

The maximum bed temperature reached for the run illustrated in Figure 5.2 was 745 °C. It is clear from the image that the sensor is registering a logical pattern of the thermo-mechanical evolution: first, the contact pressure is very low at the initial conditions, then the pressure starts peaking at the lower central region where the temperature is maximum and the packing is denser due to gravity effects. Next, as predicted by the single effect and precursor experiments in Chapter 3 of this work, the stresses continued to increase until a critical creep temperature of around 720 °C was reached, after which the central region experienced a sharp drop in contact pressure. Finally, the pressure dies down upon turning off the heaters power. On the second heating cycle, the stresses were reduced by 25% as a result of pebbles resettling and plastic rearrangements which creates a gap near the top surface of the bed allowing the pebbles to expand occupying this space first upon reheating before exerting pressure on the walls. The maximum stress recorded for this run was 154 kPa, however, for the run shown in Figure 5.3 with 4.5% higher packing and maximum bed temperature of 800 °C, the maximum stress magnitude reached was 241 kPa. These values are consistent with the precursor experiments for the no pre-compaction runs presented in section 3 of this work.

The critical stress relaxation temperature T_{sr} is defined in this study as the temperature at which the contact stress reaches a peak and begins to drop for a given contact pressure level. For example, a T_{sr} of 720 °C was observed for the first cycle. This is also consistent with the stress-relaxation precursor experiments and modeling which verify the dominant role that the temperature plays in controlling the bed creep phenomenon.

Additionally, since temperature is the more dominant parameter governing creep, the stress relaxation process becomes more significant as soon as the maximum temperature in the bed reaches 800 ˚C, which happens as the majority of the pebbles are still at lower temperatures due

to the low thermal diffusivity of the bed. In other words, the pressure rise as a result of thermal expansion is being balanced and slowed down by the stress-relaxation in the creep zone, as well as the stress reduction associated with thermal cycling due to pebbles resettling as explained earlier (stress self-regulation). Additional stress evolution data was collected (e.g. Figure 5.3) where a consistent pattern of stress saturation after the 3^{rd}- 4^{th} thermal cycle was observed. The stress levels stabilized at around 0.1 MPa similar to the previous 740 ˚C cycle. Moreover, a similar stress relaxation pattern can be noticed at the end of the first cycle.

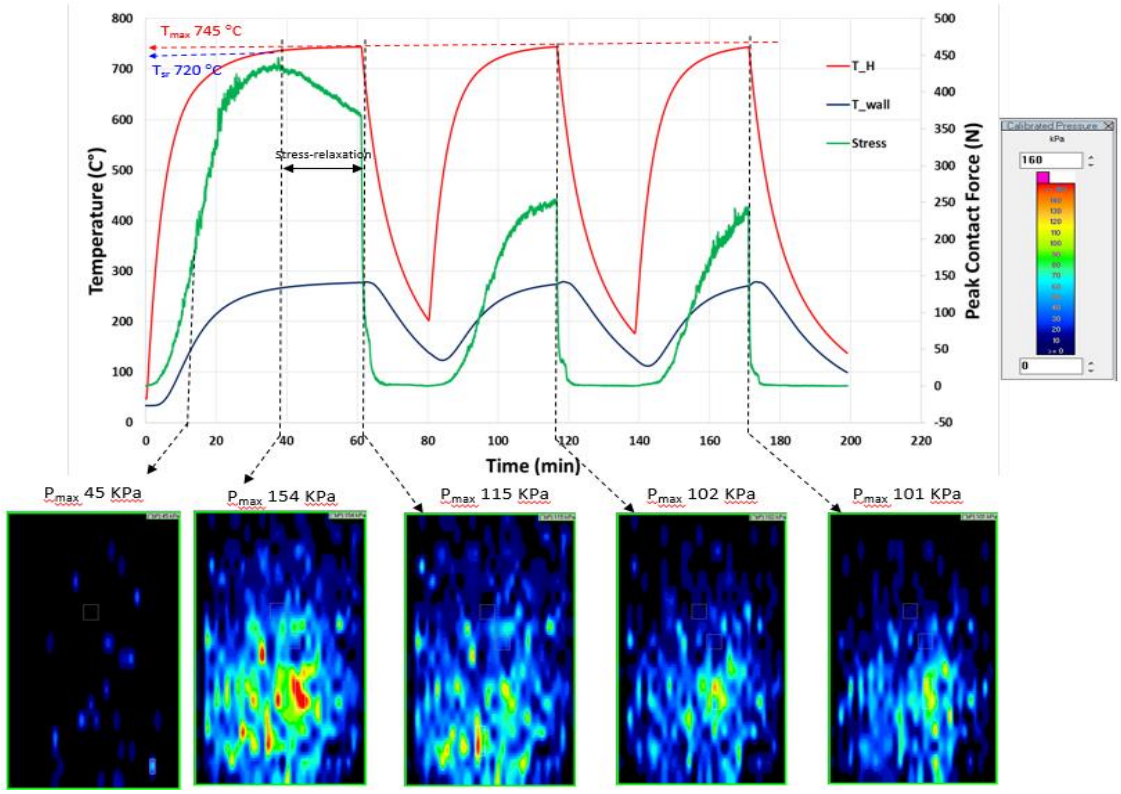

Figure 5.2 Stress/temperature evolution maps capturing stress reduction due to creep and pebbles resettling with cycling

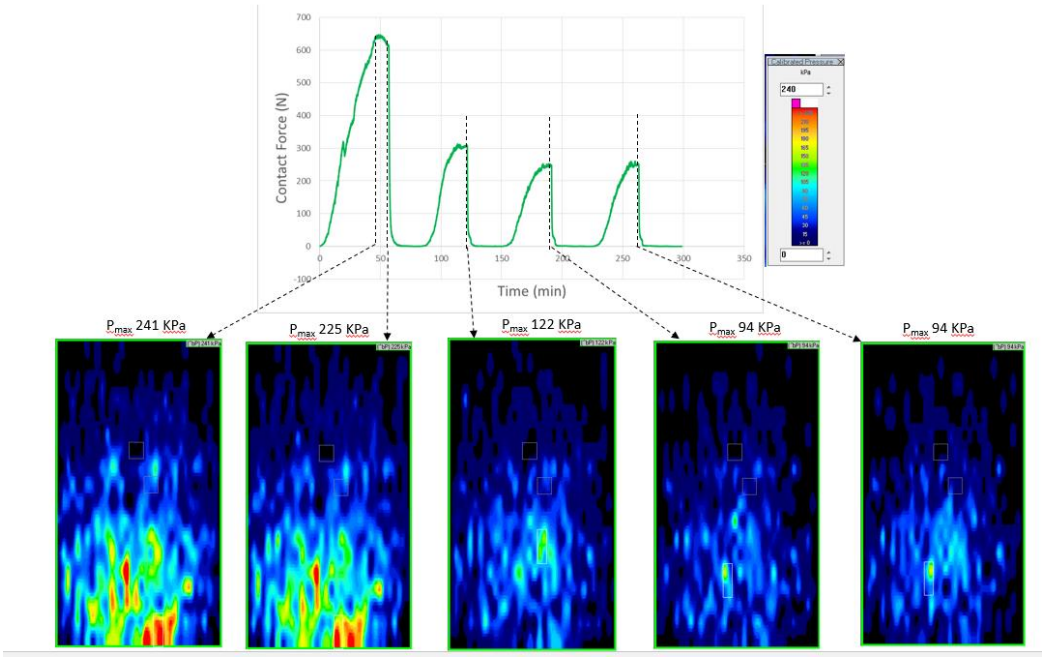

Figure 5.3 Additional pressure evolution data for rod heaters T_{max}=750 ˚C

Due to the temperature limitation of the rod heaters, the plate heaters were used again to reach higher and more relevant bed temperatures (Figure 8). This time, the maximum bed temperature reached was 810 °C but the peak pressure values reached were smaller than the rod heaters experiments because the plate heaters were half the length of that of the rods, and therefore, a much lower percentage of pebbles of pebbles reached the high temperatures. Additionally, since temperature is the more dominant parameter governing creep, the stress relaxation process becomes more severe as soon as the maximum temperature in the bed reaches 800 ˚C, which happens as the majority of the pebbles are still at lower temperatures due to the low thermal diffusivity of the bed. This means that the pressure rise as a result of thermal expansion is being balanced and slowed down by the pressure drop in the creep zone (pressure self-regulation).

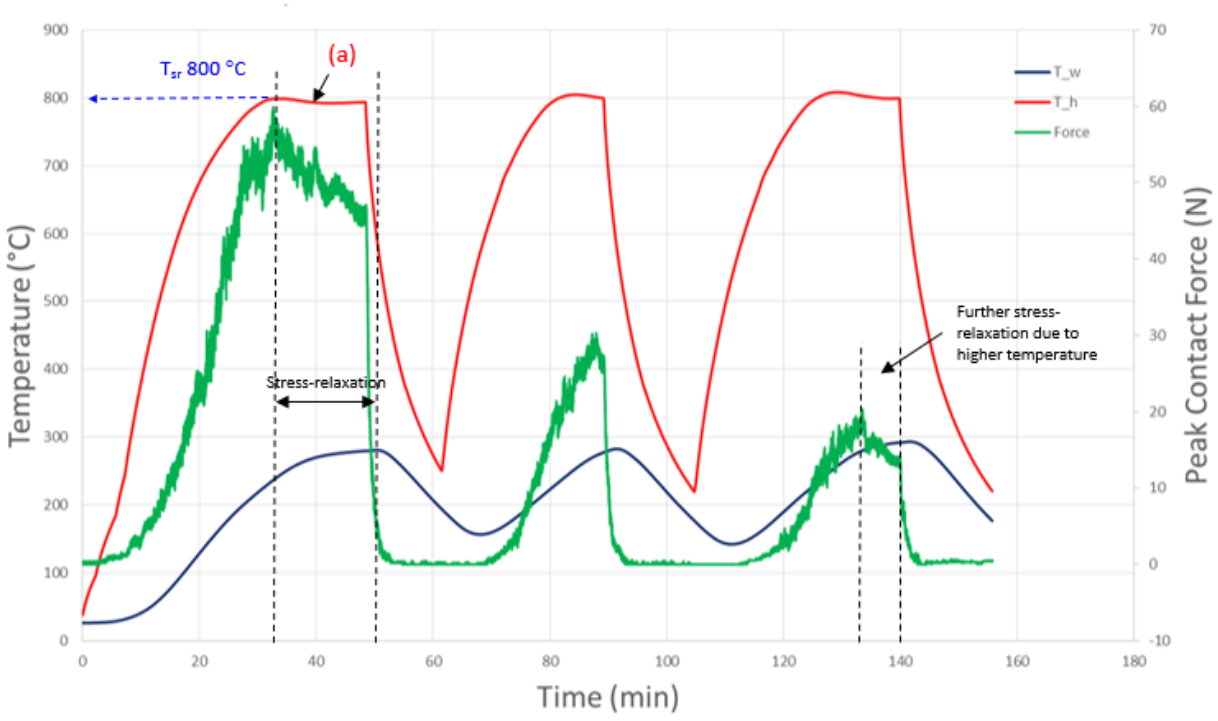

Figure 5.4 Temperature and pressure evolution for T_{max}=810 ˚C with plate heaters

- Interesting temperature observations:

– The hot zone temperature dropped to 10 °C lower than the maximum historic temperature reached as soon as the contact forces began to drop due to creep, point (a). This can be explained by the enhancement of local thermal conductivity in the region above creep temperatures as the pebbles sinter together under high temperature and pressure where the pebble-pebble contact becomes area-contact instead of point-contact. However, this temperature drop quickly stabilized under the mechanism of two effects: (1) Heat transfer from the surrounding pebbles to the sintered zone, and (2) deterioration of heat transfer with the coolant wall due to the drop in contact pressure (temperature self-regulation).

– The critical stress-relaxation temperature, T_{sr} , is higher in this run (800 °C as opposed to 720 °C) since the maximum pressure value did not exceed 60 kPa. That is to say that T_{sr} temperature increased to compensate for the lack of stresses. Nonetheless, temperature effects dominate since it has an exponential dependence on creep rate.

– The maximum bed temperature increased by 11 °C from 799 °C in the 1st cycle to 810 °C in the 3rd. This happens as a result of loss of adequate contact between the pebbles and the coolant walls as the pressure drops with thermal cycling.

For the pulsed experiments, the highest maximum bed temperature recorded was 868 °C after running 6 thermal cycles. Consistent with all previous experiments, a state of thermo-mechanical stability was reached after the 4^{th}-5^{th} cycle. No evidence of chemical reactions or severe pebbles necking, sintering, crushing or discoloration were observed. Figure 5.5 shows the post experiment

high-temperature creep region of the bed with the pebbles sticking together and forming lumps. This explains the stress-relaxation mechanism where under high temperature, stress, and given enough time, the pebbles soften and transition to area-contact from point-contact interaction resulting in reduced stress levels. However, no permanent deformation was found and the pebbles separate with simple tapping on the heaters.

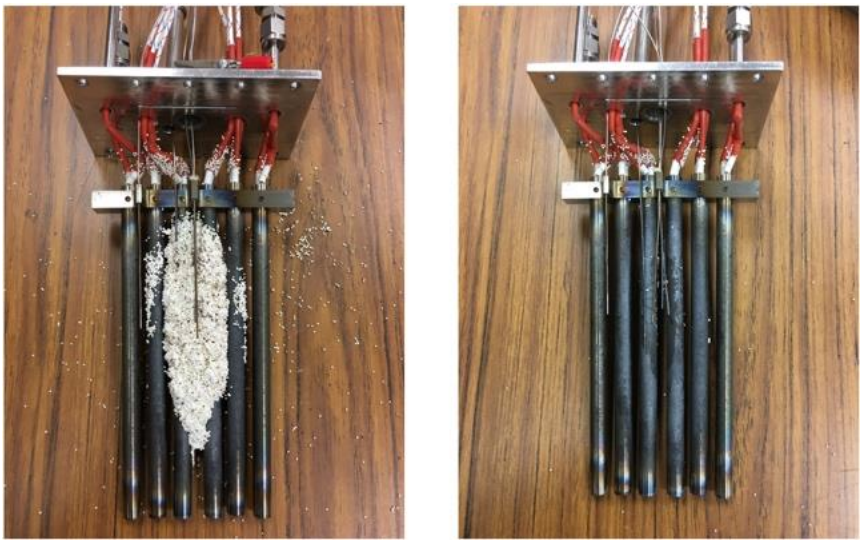

Figure 5.5. Left: after 6 thermal cycles and reaching 870 C. Right: after scrapping the pebbles off the heaters by simple tapping

Another important observation was that a temperature jump of about 25 °C was recorded between the maximum 1st cycle temperature and that of the 4th (from 842 to 867 °C) and remained stable after the 4th cycle as shown in Figure 5.6, and 5.7. The same average temperature increase was observed at all thermocouple measurements for the same wall temperature. The temperature increase was consistent with the stress reduction with thermal cycling and reached a stable level

as the stresses stabilized as well. This can be explained by the deterioration of heat transfer with the coolant wall due to the drop in contact pressure and hence lower effective bed thermal conductivity 'K' and interface thermal conductance 'h'. However, this temperature increase is balanced by a reduction in temperature resulting from the locally enhanced thermal conductivity in the creep region as the pebbles necked together under high temperature and pressure and the pebble-pebble contact becomes area-contact instead of point-contact. The resultant effect of this temperature self-regulating mechanism is consistent temperature stability after the 4th thermal cycle.

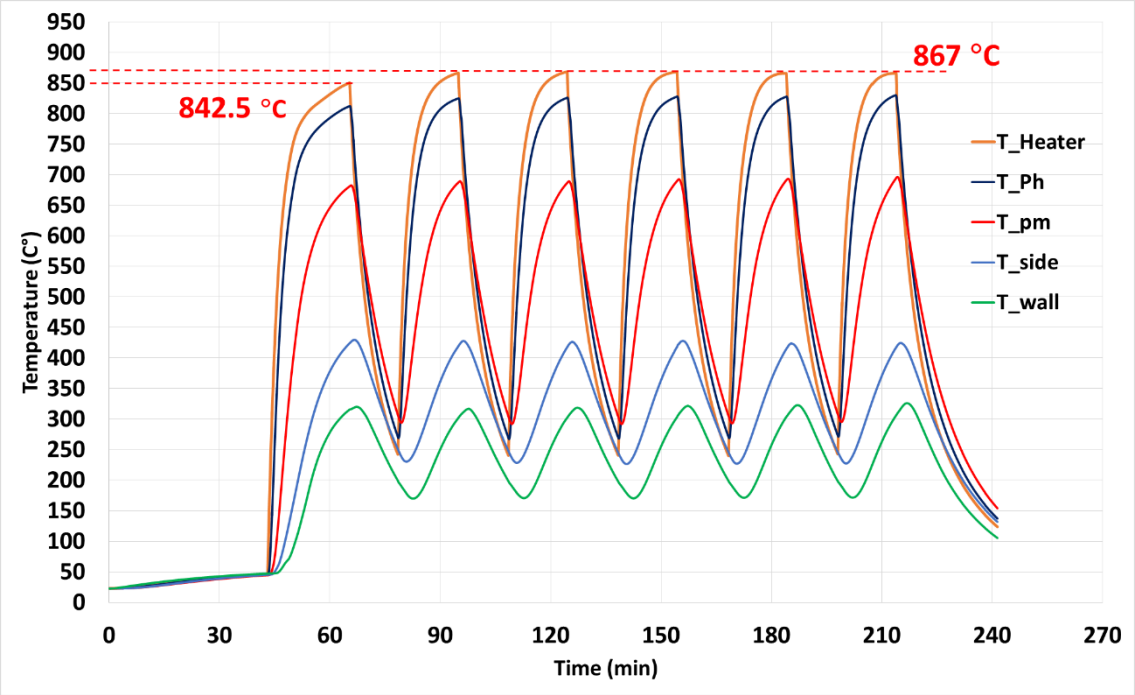

Figure 5.6 Six cycles temperature evolution showing an average 25 °C temperature jump between the 1st and 6th cycle's thermocouple measurements due to deteriorating interface conductance.

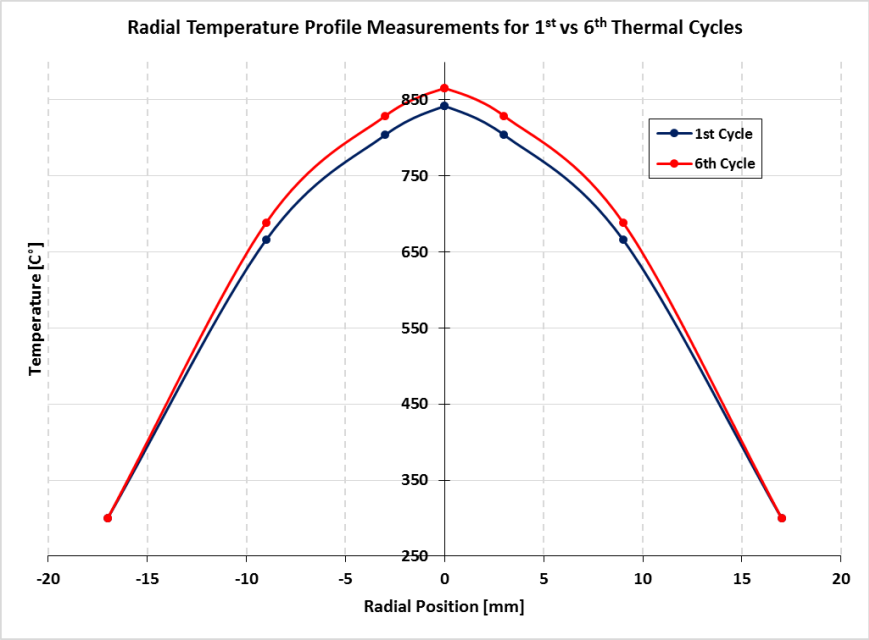

Figure 5.7 Spatial projection for the 6 cycles' peak temperatures at the radial thermocouple locations

One additional note-worthy observation shown in Figure 5.8 is the steeper slope of the cooling rate in the zone closest to the heater relative to the thermocouple measurements near the coolant wall region which causes the intersection of the temperature profiles during the cooling cycles and a delayed response of the near-wall pebbles temperatures to the heaters shut down. That is to say that for the larger portion of the cooling cycle, a heat gradient reversal effect occurs at a point between the heaters and the cooling wall causing the peak temperature in the bed to shift away from the heaters which results in a wave-like temperature profile characterized by gradient inversion as shown in the spatial projection comparison between the peak heater temperature timestamp (A) and the end of the cooling cycle at point (B) of Figure 5.8. This effect is attributed to the low thermal diffusivity of the pebble bed which is regarded as the ratio of the thermal conductivity of a material to its specific heat capacity ($\frac{k}{\rho C_p}$) and has physical significance in the context of transient conduction processes. Thus, since the pebbles have a low conduction

rate relative to their heat storage capacity, they are considered to have high thermal inertia and tend to exhibit a slow response to changes in temperature.

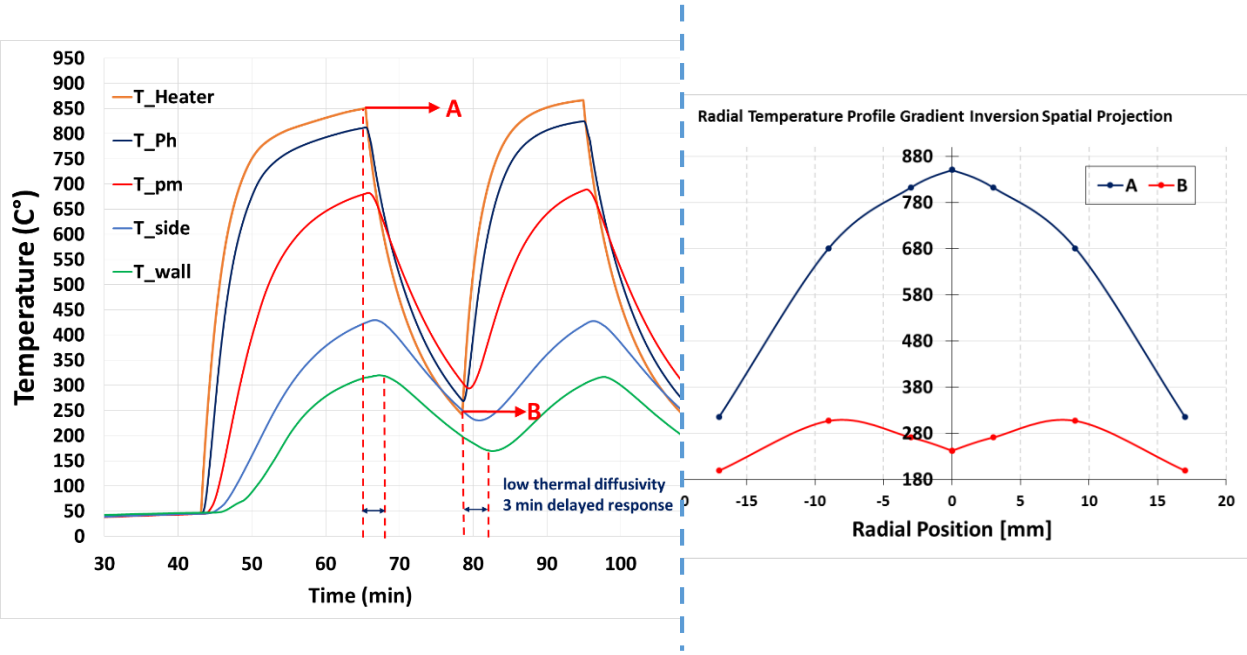

Figure 5.8 Spatial projection of the radial thermocouple measurements showing the effect of low thermal diffusivity of the pebbles on the delayed response and gradient inversion

5.3. Continuous operation experiments

In order to isolate the effects of creep without introducing thermal cycling and effects of plasticity, a 24-hr experiment was carried out and the temperature/stress evolution was recorded. Figure 5.9 illustrates some key observations:

(1) Contact stress levels rose to 120 kPa then dropped to negligible values due to creep after the first 2 hours of operation – agreeing with precursor experiments.

(2) Significant sintering took place in the core region of the bed resulting in local thermal conductivity enhancement which reduced the creep zone temperatures by over 40 ˚C over 24 hrs.

(3) The temperature remained stable in the non-creep region of the bed with a slight 4 ˚C rise at the wall.

(4) The heater surface thermocouple broke after 7 hours of operation due to excessive pebbles stress/sintering.

The observations emphasize the desirable effects of creep in solid breeder pebble beds as it:

(1) Mitigates the risks of pebbles crushing/fragmenting and structural materials failure associated with excessive stress build-up under confined thermal expansion and irradiation-induced swelling.

(2) Flattens out the temperature profile by locally enhancing thermal conductivity at the hottest core region (gradient smoothing) which reduces chances of thermal runaway by staying within design temperature window as demonstrated in Figure 5.10.

(3) May allow the possibility of operating at higher Neutron Wall Load (NWL) after the first 24 hrs of operation which could yield tremendous benefits for power extraction.

However, since pebbles necking could also increase the risks of inhibiting tritium release, care must be taken to how much necking is tolerated before tritium release is significantly reduced.

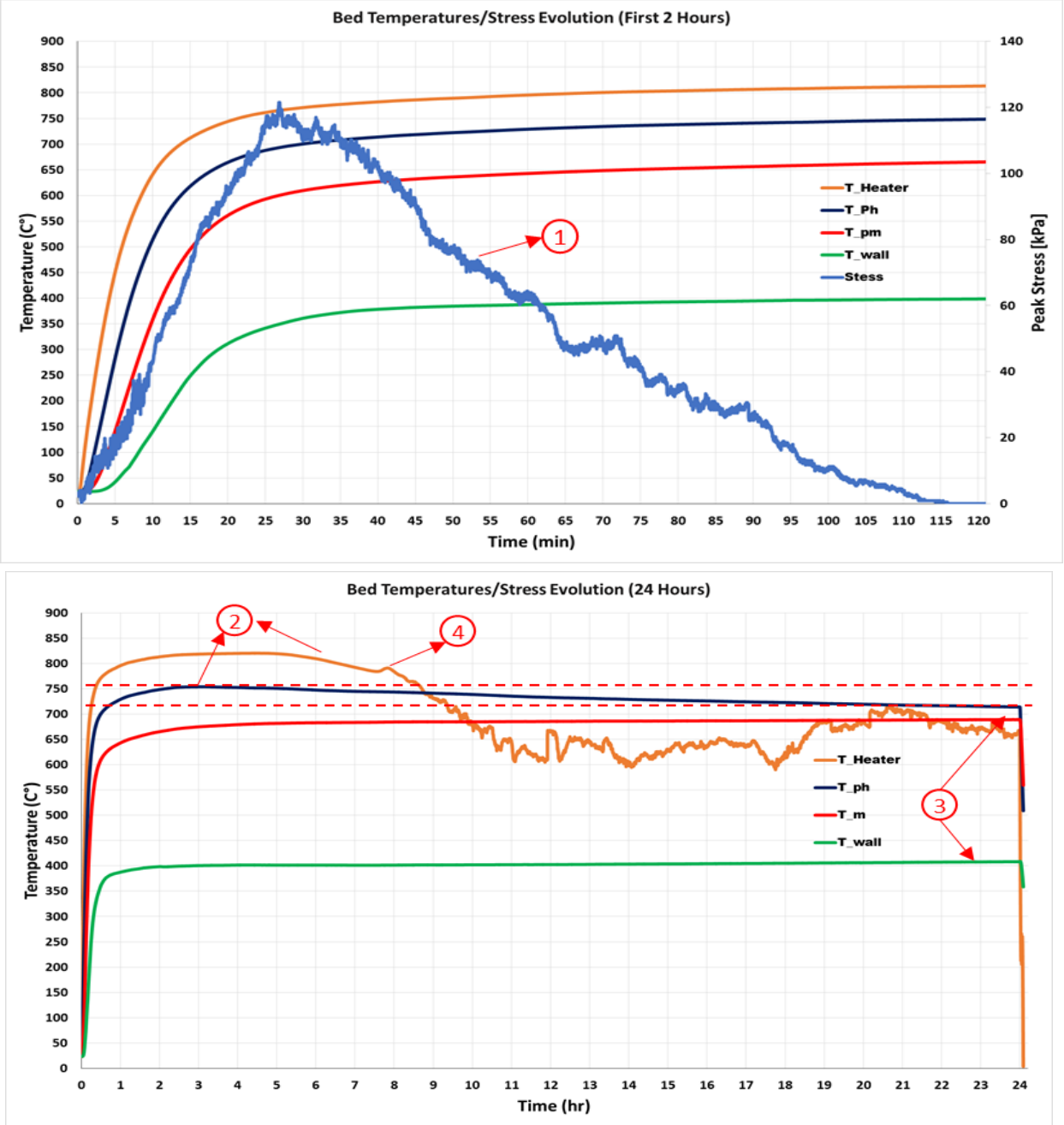

Fig. 5.9 Temperature and stress evolution of the first 2 hours showing the stress reducing to negligible values (top). Temperatures evolution over 24 hours (bottom)

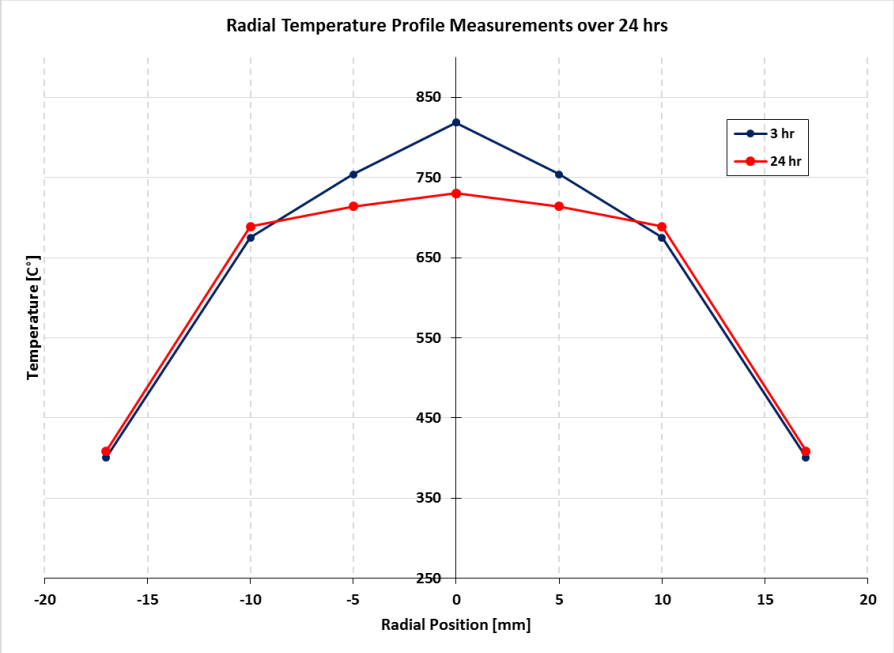

Figure 5.10 Temperatures/Stress evolution over 24 hours demonstrating the gradient smoothing effect after 24 hours of operation under creep relevant temperatures

Figure 5.11 Aggressive pebbles sintering into solid blocks at the creep region extending up to 1 cm away from the heaters

Figure 5.12 sintered chunks of pebbles collapsed after hammering on the heaters with sharp tool

Figures 5.11, and 5.12 demonstrate the strong dependence of creep/sintering on time (24 hrs) under high temperatures (820 °C) and fixed boundary confinement. That is to say that for previous thermal cycling runs which usually stabilize by the 6th cycle corresponding to 4-5 hrs of operation, the pebbles did not show the same severe sintering behavior that was shown in the 24 hr run. Instead, even for the 6-cycle pulsed operation run that reached 869 °C, no aggressive sintering was found and the pebbles separated from the heaters' surface easily with simple tapping, which means that this type of sintering is considered "elastic (reversible/temporary) sintering".

For all the experiments conducted in this work, the creep activation or sintering temperature at which the generated stresses started to drop rapidly was recorded around 750 °C. However, temperature alone is not the sole governing parameter that marks the onset of sintering; it is the combination of the high temperature (>750 °C), fixed mechanical confinement, thermally-induced

stress, and more importantly, time. This was evidenced by the excessive sintering when the experiment's cycle time was 24 hours at 800 – 819 °C as opposed to minimal sintering for the pulsed experiment with total duration of about 4 hours of which half of this time was heating. Since the pebbles were not subjected to the high temperatures long enough, even though the peak temperature was 869 °C (100 °C higher than the stress relaxation temperature), no sintering complications were observed. Conversely, when the temperature was held at around 800 °C for 7 hours in the continuous run experiment, the creep zone temperatures started dropping rapidly indicating the significant local thermal conductivity enhancement due to excessive sintering. This type of sintering which extended over 1 cm beyond the heaters surface and can only be removed by hammering with a sharp tool is considered "excessive plastic (irreversible) sintering". Therefore, for TESOMEX operating conditions and configuration, the sintering conditions at which the pebbles start sintering into irreversible solid blocks was defined as a combination of running at temperatures >750 °C under confined mechanical boundary for 7 hours or longer.

Although creep enables the bed to reach stable temperatures and alleviates the pressures that could otherwise exceed the pebbles' mechanical strength limits, the effect of having a percentage of pebbles sintering on tritium release should be evaluated. If proven detrimental to tritium release, the pebbles need to be enhanced to sinter at a higher temperature than those expected in the core region of the bed.

5.4. Pebble bed pre-conditioning for thermo-mechanical stability

Even though experiments have shown that the pebble bed reaches a state of thermo-mechanical equilibrium, the 5% average bed temperature increase over the initial 4-5 thermal cycles for the pulsed operation could force the bed to operate outside the allowed temperature window. Therefore, a pre-conditioning control mechanism has been investigated with the goal of reaching an optimal initial packing configuration that maximizes thermo-mechanical stability.

After each experimental campaign, the bed was cooled down to room temperature and additional pebbles were added. Contrary to the initial bed packing state (63% packing fraction for all runs on average) where no additional pebbles could be poured past the packing limit, an average of 5% more pebbles were successfully added at the end of the experiments after cool-down. This confirms the pebbles' irreversible rearrangement and resettling that creates a gap at the top enabling us to add more pebbles and reach higher packing density. Moreover, after adding pebbles, the heaters were turned on once again and the stresses were measured to be more than double that of the initial cycle of the first experiment as shown in Figure 5.13. It is also worth noting that the temperature evolution was identical for the 3 cycles of the second experiment, showing much higher levels of thermo-mechanical stability. Therefore, this technique can be used to improve (1) the packing density of pebble beds which yields higher TBR, and (2) the thermo-mechanical stability and predictability.

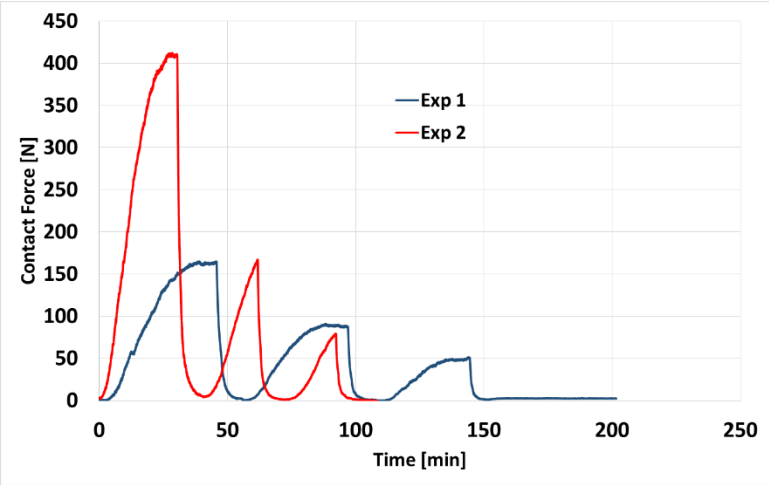

Figure 5.13 Stress evolution after re-packing. Stress levels more than doubled after adding 5% more pebbles post cool down proving the resettling and compaction effects.

A few mechanisms contributed to better stability with re-packing:

1- More pebbles packed in the same volume lead to higher bed effective thermal conductivity.

2- Higher stresses result in more inter-pebble and pebble-wall surface contact, which lead to higher thermal conductivity and interface conductance, and therefore lowering bed temperatures and improving their stability.

Given the usefulness of the effects discussed above, the following pre-conditioning procedure is proposed:

Due to the difficulty of re-packing after placing the breeder in the equatorial port, the following pre-conditioning procedure has to be carried out prior to installation:

1. Insert the breeder inside a furnace where the pebbles can be heated to the specified uniform temperature.
2. Apply an adequate number of thermal cycles at the specified maximum temperature to induce pebbles re-arrangement and settling.
3. Add pebbles to refill the formed gap and measure the incremental percent increase in packing fraction.
4. Repeat steps 1 – 3 until no further filling can be achieved.

5.5. Experimental limitations

TESOMEX results proved our hypothesis regarding interacting physics between creep, plastic rearrangements, pebbles resettling, and thermal cycling, besides capturing, with high granularity, the desirable self-regulation mechanisms and steep temperature gradient smoothing. However, TESOMEX was designed to accommodate discrete thin wire heaters for volumetric heating simulations. The fabricated test article's dimension along the heat path direction reproduced the HCCR single breeder layer dimension considering the volume occupied by the wire heaters is insignificant. When wire heaters became practically unfeasible, the rod heaters were adopted to produce prototypical temperature magnitude and gradient, which came at the cost of further deviation from the nuclear heating profile as well as additional packing disturbance as illustrated in Section 4 of this work. The new heating approach may have also contributed to heat flow asymmetries in addition to undesirable packing effects resulting from the heater connections at the top region of the bed. Although this region is of little interest to our analyses, it may have introduced unnecessary disturbances to the core region where interesting phenomena are expected to occur.

The total volume of the 6 rod heaters is about 9% of the volume of the pebble bed, which can introduce structured packing regions. Optimization analyses were run to come up with the optimal spacing between the heaters that results in the temperature profile closest to that of the nuclear heating. However, the packing disturbances have not been quantified. On the plus side, unlike the dense wire mesh, the smooth surface of the heaters and their optimal spacing contributed to reaching packing fractions of 61% before pre-conditioning and 65% after. Therefore, any negative effects on packing, if any, were kept to at a minimum.

Another major limitation was that the maximum operating temperature that the tactile pressure sensor can tolerate before being severely damaged is 200 °C without further thermal protection and 300 °C with a thin flexible Silica sheet. This created a major restriction on the allowed thermal cycle time at the high temperatures as well as the coolant wall temperature, which alters the overall thermal gradient. Since the goal was to recreate the prototypical nuclear temperature gradient, almost all conducted experiments reached 300 °C. Unfortunately, this came at the expense of losing five expensive sensors in order to obtain necessary data. Also, the sensor cannot be used in the bulk region where it would be subjected to different multi-directional forces and stress invariants which may lead to difficult interpretation of the results. However, one of the main purposes of the sensor in the TESOMEX campaigns context was to obtain 2D normal pressure maps at the interface where the temperature is within the 300 °C maximum range and validate the numerical model which can then be used to extrapolate the stresses in the bulk region of the bed. Consequently, a sensor that can continuously operate safely at 400 °C would be sufficient.

The average bed temperature jump of about 25 °C observed during the thermal cycling experiments' which was ascribed to the deterioration of the wall/bed contact is considered to be under worst conditions since the experiment has been conducted under non-flowing air which has a lower thermal conductivity and thermal transport capabilities than flowing Helium purge. Although, prior experimental efforts have shown a strong dependence of the interface conductance on contact pressure regardless of the bed atmosphere, the bed atmosphere is expected to lower this temperature jump. Due to experimental limitations and the design of the test article box and flange connections, it was increasingly difficult to create a vacuum to run experiments under flowing

helium conditions and at the same time accommodate the thermocouples, heaters, and pebble filling hole connections.

Therefore, even though the temperature deviation was less than 8% at the maximum error point and experiments reached packing densities of 61%, TESOMEX individual pebble rearrangement/resettling after thermal cycling, plastic and creep deformation may not directly generalize to accurate magnitudes for blanket prototypical bed behavior. Accordingly, modeling efforts presented in the next section aim to compliment the experimental limitations by validating the results under TESOMEX operating conditions, after which adequate extrapolations can be made to accommodate various operating scenarios. Finally, Chapter 7.2 provides guidelines and recommendations to overcome most experimental limitations in future mock-up breeder experimental efforts.

Chapter 6

6. Application of Thermo-mechanical Finite Element Model (FEM) and Comparison with Multiple-Effects Experiments

6.1. FEM methodology/modeling Improvement

For a reliable design of fusion blankets with solid breeder and beryllium pebble beds, it is critical to have validated computational tools for predicting thermo-mechanical conditions and evolution over blanket lifetime. The material models currently in use at UCLA to capture pebble bed synergistic effects are: (1) non-linear elasticity, (2) temperature-dependent Extended-Drucker-Prager plasticity model combined with the (3) Cap creep model, in addition to, (4) temperature-dependent thermal properties (thermal conductivity, thermal expansion coefficient, specific heat). Many of the models have had their constitutive equations verified with single-effect experiments.

A 3D, fully-coupled thermo-mechanical volumetrically-heated, transient breeder cell Finite Element Model capable of simulating continuous thermal cycles to reach stress-saturation levels has been developed and validated against multiple effects experiments. The model incorporates all previously validated single-effect material models, permitting the analysis of many synergistic effects of a solid breeder in a typical fusion environment.

The effects include thermally-induced stresses accompanied with creep deformation/stress relaxation and non-idealistic interface contact behavior. The material model parameters of single-

effect experiments were, by definition, derived by testing the pebble bed behavior for a matrix of constant bed temperatures and stress states. Therefore, in order to utilize previous experimental efforts from an FEM simulation perspective, the effect of volumetric heating can be analyzed by discretizing the pebble bed into a fine-mesh of thousands of inter-connected local elements each representing a different temperature/stress state governed by the single effect model correlations to reconstruct the global continuous picture of the pebble bed thermo-mechanical behavior using the appropriate interpolations and material models. Nevertheless, there has always been uncertainty in the predictive capability of FEM simulations until validation against multiple-effect experiments TESOMEX presented at the end of this section.

The non-linear elasticity was modeled by defining Young's modulus as a function of two stress invariants, I_1 and J_2, and temperature, T. The material parameters of Ae(T) and s were curve-fitted to experimental data.

$$E = A_e(T)[(1+\nu)J_2 + \frac{1-\nu}{3}I_1^2]^{s/2} + E_0 \tag{6.1}$$

The plasticity cap hardening law was defined through a function of volumetric plastic strain (ε_v^p) and (I_1), which has the exponential form in Eq. (6.2).

$$\varepsilon_v^p = W(T)\{e^{[D_1 - D_2(X - X_0)](X - X_0)} - 1\} \tag{6.2}$$

A strain-hardening cap-creep model was used to simulate the stress relaxation experiments, in which the volumetric creep strain rate ($\dot{\epsilon}_{v,cr}$) is expressed as a function of equivalent creep stress ($\bar{\sigma}_{cr}$), volumetric creep strain ($\epsilon_{v,cr}$) and temperature (T), shown in Eq. (6.3). C1-C4 are recalibrated material constants derived from past creep tests to fit stress relaxation data.

$$\dot{\varepsilon}_{v,cr} = C_1 \sigma_{cr}^{C_2} \varepsilon_{v,cr}^{C_3} e^{-C_4/T} \tag{6.3}$$

6.2. Identification of non-linear elastic and Cap-Creep constitutive equations and correlations for NFRI Li_2TIO_3 pebble beds for FEM thermo-mechanical analysis

Understanding the thermo-mechanical behavior of ceramic breeder pebble bed during operation is critical for blanket design and optimization. Since the pebble bed can be deformed under thermally-induced mechanical loads, its permanent volume reduction changes the contact condition of pebble bed/structural wall and also reduces the heat transfer at the interface due to gap generation. To predict and optimize the pebble bed behavior, especially the maintaining or controlling of pebble bed dimension, the FEM simulation of ceramic breeder unit with the CAP models embedded in ANSYS has been used. Because in the FEM model parameters need to be identified by the experimental data, UCLA has completed a series of experiments, including the uniaxial compaction, creep, and CTE tests, on the Li_2TiO_3 pebbles (D=1.0mm) provided by NFRI with UCLA's facilities. The experimentally obtained stress-strain curves are used to derive both an elastic modulus and a hardening law for Li2TiO3 pebble beds. The creep rate as a function of temperature and stress is obtained through creep tests.

6.2.1 Experimental results

Uniaxial compaction tests

The Li_2TiO_3 pebbles are packed in a cup (D=46.5mm) with an average initial P.F. of 63.2%, and then the uniaxial compaction tests are conducted for the conditions of 6MPa (peak stress) and R.T./550/650/750^oC in a vacuum environment. The loading/unloading rate of 1MPa/min is used. The axial pressure and bed deformation are recorded and plotted in Figure 6.1.

It's seen that higher temperature results in a softer bed behavior indicated by the loading path, and larger volumetric plastic deformation (or bed volume reduction) indicated by the intersection of the unloading path and strain axis. The obtained stress-strain data have been applied to derive the non-linear elasticity and CAP hardening FEM model parameters. It is also observed that the 2nd cycle results in a much smaller plastic strain compared with the 1st cycle for the whole temperature range. This plastic strain increment will reduce with cycle's number, and finally a nearly repeated loading-unloading path can be achieved. Therefore, the method of cyclic pressurized pebbles packing is suggested and believed to be much helpful for minimizing the bed volume reduction and improving the pebble bed dimensional stability during reactor operation.

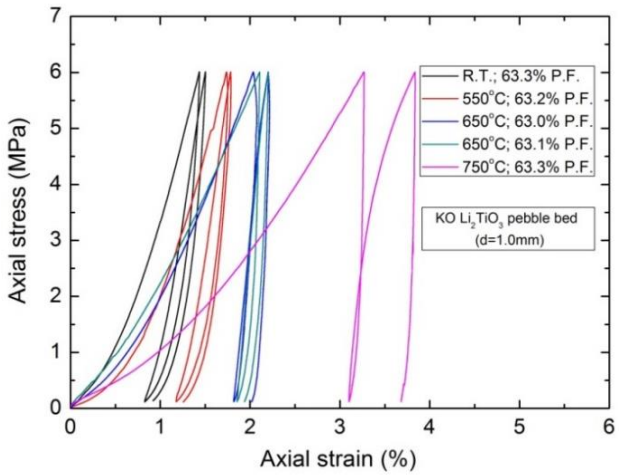

Figure 6.1. Stress-strain relation of KO Li_2TiO_3 pebble bed.

Creep tests

To explore the responses of pebble bed to the long-term pressurized condition at elevated temperatures, six creep tests are conducted at 1.0/2.5/4.0MPa (750°C) and 2.0/4.0MPa (650°C). With the same experimental setup as uniaxial compaction tests, the pebble bed is heated to the

target temperature first and then loaded to the target pressure, and this pressure is held constant for a certain time period. The axial bed deformation is recorded after the target pressure is reached and recorded as the bed volumetric creep strain. Figure 6.2 illustrates the creep strain evolution, which has been used to derive the FEM creep model parameters. It's found that higher temperature and larger pressure generate more creep strain. A significant creep strain (5.5%) results under the condition of 750^{o}C/4MPa and continues to increase after 15h. For 750^{o}C, under a load of 1 MPa, the creep strain tends to saturate at 1.0% after 13h. For 650^{o}C, the creep strain saturates much faster at lower strain levels: 3h at 1MPa and 8h at 4MPa. The obtained creep strain data have clearly shown that the influence of temperature on creep strain is more significant than applied pressure. Besides the plastic deformation of pebble bed, the creep strain is another major factor contributing to the bed volume permanent reduction. Therefore, the temperature distributions among pebble bed and its peak value should be well controlled. The dimensional design of ceramic breeder unit needs to make the pebble bed work in its saturated creep state so that the bed geometry can be maintained. Concurrently, the total bed volume reduction caused by plastic and creep deformations should be minimized considering the pebble bed/wall gap generation and its consequences.

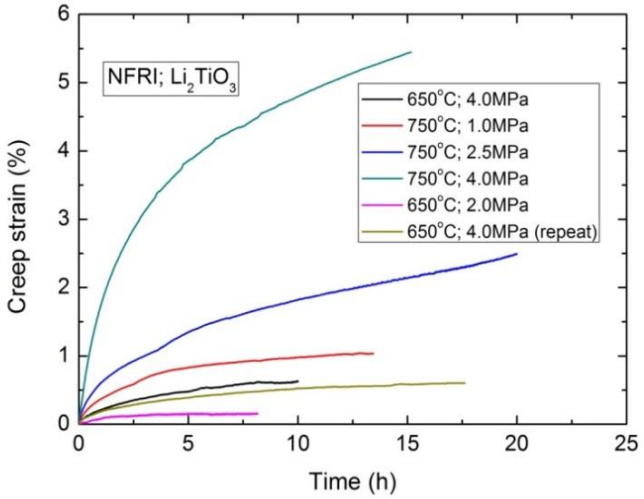

Figure 6.2 Creep strain evolution of KO Li_2TiO_3 pebble bed.

6.2.2. Identification of FEM material model parameters

FEM modeling is able to efficiently predict the bulk thermomechanical behavior of pebble bed and its interactions with structural wall for different blanket designs. A fundamental assumption for FEM modeling is to treat pebble bed as a continuous media by using effective material properties of pebble beds, which can be experimentally identified. The FEM pebble bed material models of the non-linear elasticity, CAP yielding/hardening and strain-hardening creep models are needed for the KO HCCR TBM simulation. Their parameters have been identified using the obtained experimental data from uniaxial compaction and creep tests.

Non-linear elasticity

The isotropic non-linear elasticity, defined by Equation 6.4, has been used to describe pebble bed elastic behavior as outlined in section 2. Young's modulus is a function of two stress invariants (I_1 and J_2) and temperature ($A_e(T)$). For the case of the uniaxial compaction test, the Young's modulus

is defined as the function of axial stress (σ_y), shown in Equation 6.5, and the relation of axial stress and strain is shown in Equation 6.6. Thus, the material parameters of $A_e(T)$ and s can be identified by experimental data. The unloading path of the 1st cycle in the stress-strain relation plot (see Figure 6.3) reflects the elastic volume recovery of the pebble bed, and its slope is evaluated as the bed modulus varying with temperature and applied stress, shown in Figure 6.3. The bed modulus increases with pressure and temperature for Li_2TiO_3 pebble beds.

$$E = A_e(T)[(1+\nu)J_2 + \frac{1-\nu}{3}I_1^2]^{s/2} + E_0 \tag{6.4}$$

$$E = E_0 + A_e\left[\frac{2(1-\nu)}{(1+\nu)(1-2\nu)}\right]^{-s/2}(\sigma_y)^s \tag{6.5}$$

$$\sigma_y = \frac{1-\nu}{(1+\nu)(1-2\nu)}E\varepsilon_y \tag{6.6}$$

The stress invariants, $I_1 = \sigma_1 + \sigma_2 + \sigma_3 = 3\sigma_{mean}$, and,

$J_2 = \frac{1}{6}[(\sigma_1 - \sigma_2)^2 + (\sigma_2 - \sigma_3)^2 + (\sigma_3 - \sigma_1)^2)] = \frac{\sigma_{von}^2}{3}$, where σ_{1-3} are principal stresses,

σ_{mean} is mean stress, and σ_{von} is Von Misses stress.

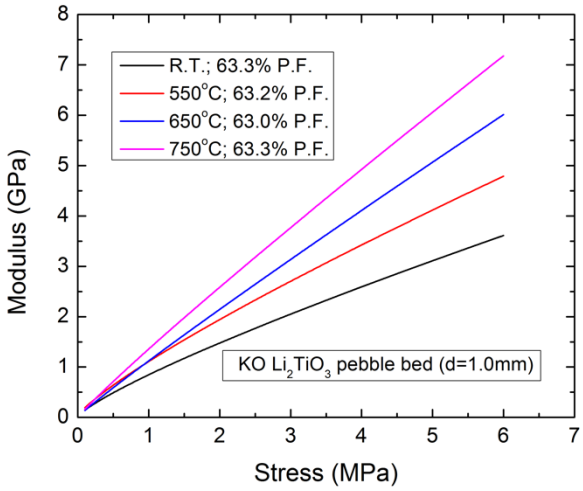

Figure 6.3 Stress-dependent pebble bed modulus at different temperatures.

To demonstrate the derivation procedures, the R.T. data of pebble bed testing has been used as an example to show the procedures of identifying A_e and s as follows:

1) With the power-law curve fitting of unloading path ($y = A * |x - x_c|^P$, Figure 6.4), the pebble bed modulus (E) can be obtained as the function of axial stress (Figure 6.5) using Equation 6.7.

$$E = \frac{(1+v)(1-2v)}{(1-v)} \cdot \frac{d\sigma_y}{d\varepsilon_y} = \frac{(1+v)(1-2v)}{(1-v)} \cdot \frac{\sigma_y p}{|\varepsilon_y - x_c|} \quad (6.7)$$

2) Based on the plot in Figure 6.5 and Equation 6.4, the values of A_e and s can be identified with the power-law curve fitting ($y = a + b * x^c$, Figure 6.6.)
3) Following the same procedure, find all the "s" values for other temperatures and properly choose one.
4) Different Ae values for other temperatures can be determined by keeping the "s" value the same. Then the equation of A_e can be properly formulated based on the distribution of A_e with temperature.

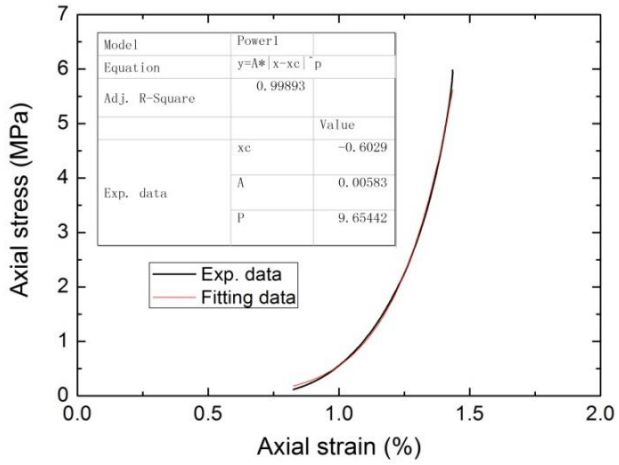

Figure 6.4. Curve fitting of the 1st unloading path.

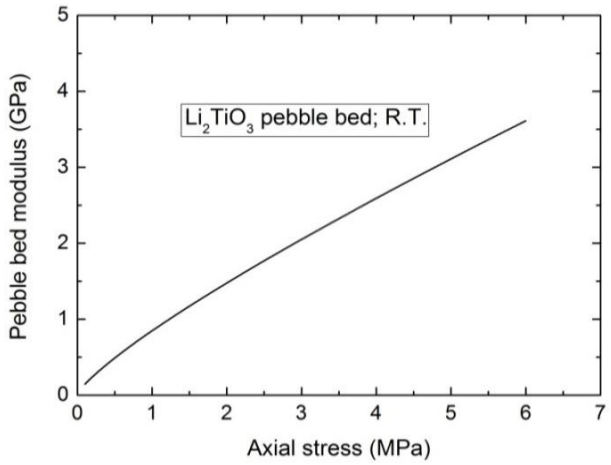

Figure 6.5. Pebble bed modulus vs. applied axial stress.

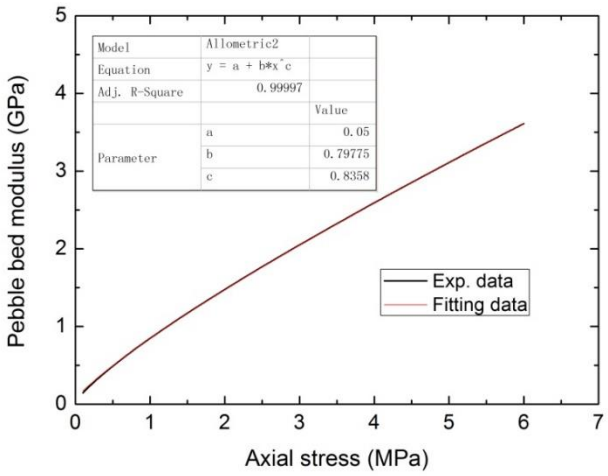

Figure 6.6. Curve fitting of pebble bed modulus.

CAP plasticity and hardening models

The cap model embedded in ANSYS is employed to simulate the permanent volume reduction of the pebble bed, which defines yield surfaces and their evolution based on stress states. The cap model in ANSYS consists of shear failure (Y_s) and compaction (Y_c) portions, shown in Figure 6.7. This unified and compacted CAP yielding function (Y) is formulated in Equation 6.8, and the cap hardening law is defined through a function of volumetric plastic strain (ϵ_v^p) and I_1, which has the exponential form in Equation 6.9. Two advantages for such formulation of CAP equations are: (1) a single continuous cap yield surface which overcomes the difficulty of transition from compactive to dilatant deformation before shear failure[36]; (2) the hydrostatic-pressure and volumetric-strain relationship (cap hardening law) in an exponential form which can capture a wide range of compaction behavior including one or two inflection points[36].

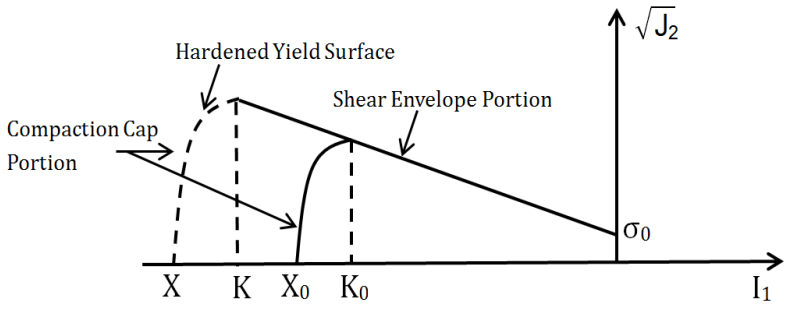

Figure 6.7. Schematic of CAP model [36].

$$Y(I_1, J_2, K, \sigma_0) = J_2 - Y_c(I_1, K, \sigma_0) Y_s^2(I_1, \sigma_0) \tag{6.8}$$

$$Y_s(I_1, \sigma_0) = \sigma_0 - \alpha I_1$$

$$Y_c(I_1, K, \sigma_0) = 1 - H(K - I_1)[\frac{I_1 - K}{R Y_s(K, \sigma_0)}]^2$$

$$\varepsilon_v^p = W\{e^{[D_1 - D_2(X - X_0)](X - X_0)} - 1\} \tag{6.9}$$

Where, σ_0 is a cohesion-related material constant; α is a material constant related to internal friction angle; H is unit step function; R is the shape function; K indicates the transition point at which the compaction cap surface and shear portion intersect; subscript s and c represent the shear envelope and compaction cap function, respectively.

The CAP plasticity model parameters have been properly chosen based on the values used for the Li_4SiO_4 pebble bed, listed in Table 6.1. The major work is focused on the identification of CAP hardening model parameters, W(T), D_1 and D_2, in which the parameter of W is defined as a function of temperature to reflect the influence of temperature on material's hardening. To do so, the 1st loading path in the stress-strain relation plot has been subtracted by its corresponding unloading path, which provides the volumetric plastic strain of pebble bed varying with applied

stress, shown in Figure 6.8. We see that the volumetric plastic strain increases with both temperature and stress. Based on the data of ε_v^p and X , the parameters of W(T), D_1 and D_2 have been identified through curve fitting. The "X" in the hardening model has the same definition as I_1.

Table 6.1: Pebble bed CAP plasticity model parameters.

Parameter	**Value**
σ_0	0.1 MPa
α	0.25
X_0	-0.1 MPa
R	0.44

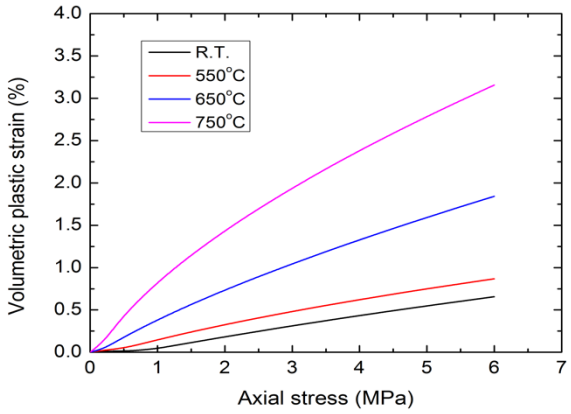

Figure 6.8 Volumetric plastic strain vs. axial stress at different temperatures.

Similarly to the demonstration of modulus derivation, the 1st-cycle loading and unloading data of pebble bed R.T. testing has been used to show the procedures of identifying W, D_1 and D_2 as follows:

1) Shift the unloading path to the origin, and subtract the loading path by the unloading path to obtain the volumetric plastic strain as the function of applied stress, shown in Figure 6.8.
2) Properly choose an initial W value (0.07 for the example case), and then curve-fit the data in Figure 6.8 with a parabolic function ($y = A + B * x + C * x^2$) to find the values of D1 and D2, illustrated in Figure 6.9.
3) Following the same procedure, find all the D1 and D2 values for other temperatures and properly choose one set.
4) Different W values for other temperatures can be determined by keeping the D_1 and D_2 values the same. Then the equation of W can be properly formulated based on the distribution of W with temperature.

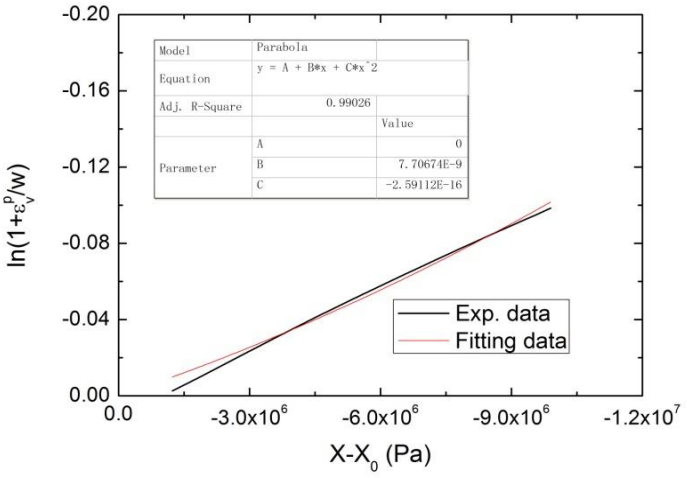

Figure 6.9. Curve fitting of volumetric plastic strain.

Strain-hardening creep model

The creep deformation of a pebble bed depends on its distributions and evolution of temperature and stress fields. To more accurately predict the creep behavior of pebble bed, the strain-hardening creep model is chosen, in which the volumetric creep strain rate ($\dot{\epsilon}_{v,cr}$) is expressed as a function of equivalent creep stress ($\bar{\sigma}_{cr}$), volumetric creep strain ($\epsilon_{v,cr}$) and temperature (T), shown in Equation 6.10 [36]. By employing the current creep strain state in the equation instead of time, the prediction can reflect the actual creep response of pebble bed to the dynamic temperature/stress fields. C_1-C_4 are material constants and need to be identified by experimental data. The obtained experimental data of creep strain evolution have been used to evaluate the creep rate for different temperature/pressure combinations, shown in Figure 6.10. Then C_1-C_4 can be identified through the power law curve fitting. The creep strain rate decreases with time and increases with temperature and pressure.

$$\dot{\varepsilon}_{v,cr} = C_1 \sigma_{cr}^{C_2} \varepsilon_{v,cr}^{C_3} e^{-C_4/T} \tag{6.10}$$

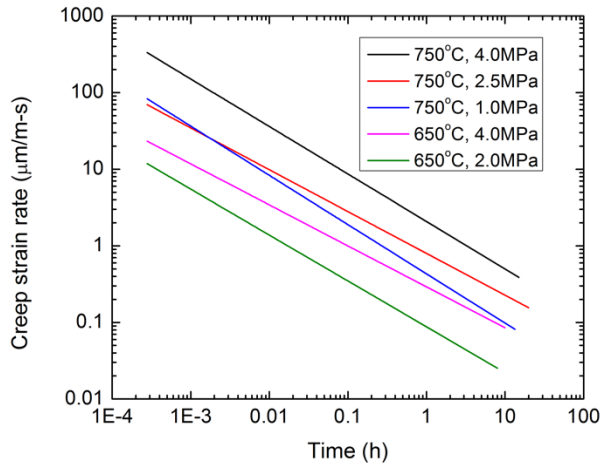

Figure 6.10. Creep strain rate evolution of KO Li_2TiO_3 pebble bed.

The specific procedures of identifying $C_{1\text{-}4}$ are:

1) Find the creep strain rate by curve-fitting the creep strain profile in Figure 6.2 for the example case of 750ºC/1MPa with a power-law function ($y = a * x^b$), shown in Figure 6.11.
2) Plot the obtained creep strain rate vs. creep strain, illustrated in Figure 6.12. Do another power-law curve-fitting of data ($y = a * x^b$, Figure 6.12) to find the C_3 (=b) value. Then the obtained "a" value represents the rest terms of C_1, C_2 and C_4.
3) Keep the C_3 value the same, and repeat the above procedures to obtain the "a" values for other temperature/stress conditions. Then the following equations (Equations 6.11 – 6.14) are available to be solved for the constants of C_1, C_2 and C_4.

$$a(T_1, \sigma_1) = C_1 \sigma_1^{C_2} e^{-C_4/T_1} \tag{6.11}$$

$$a(T_1, \sigma_2) = C_1 \sigma_2^{C_2} e^{-C_4/T_1} \tag{6.12}$$

$$a(T_2, \sigma_1) = C_1 \sigma_1^{C_2} e^{-C_4/T_2} \tag{6.13}$$

$$a(T_2, \sigma_2) = C_1 \sigma_2^{C_2} e^{-C_4/T_2} \tag{6.14}$$

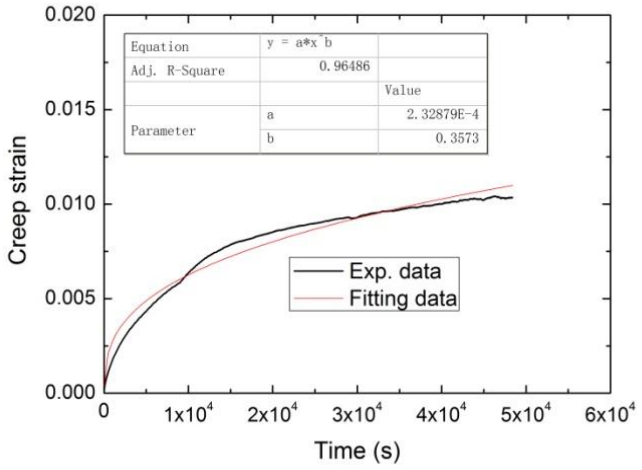

Figure 6.11. Curve fitting of creep strain profile.

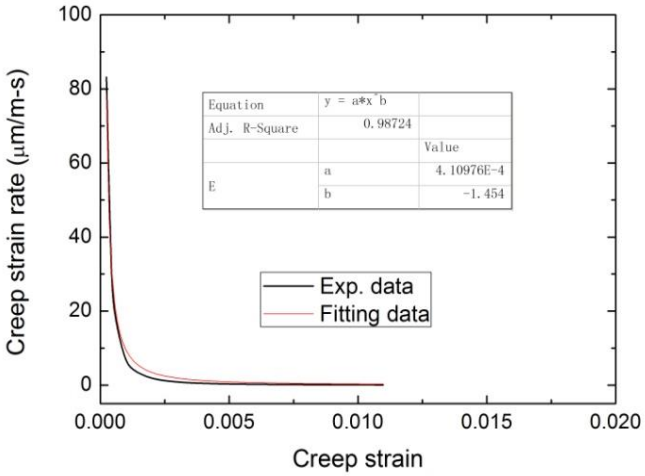

Figure 6.12. Creep strain rate vs. creep strain.

6.2.3 FEM model parameters and validation

Table 6.2 lists all the FEM model parameters for KO Li_2TiO_3 pebble bed identified by the experimental data. To validate the derived model parameters, the FEM simulations of uniaxial

compaction and creep tests have been performed. The predicted results of axial stress-strain relation and creep strain evolution are plotted and compared with experimental data in Figures 6.13 and 6.14. A good agreement is observed, which implies that the obtained FEM models can be applied to predict the pebble bed thermomechanical responses. With more tests conducted for other conditions in the future, these parameters will be updated and more reliable FEM material models are expected.

Table 6.2: FEM material model parameters for KO Li_2TiO_3 pebble bed

Parameter	**Value**
ν	0.25
s	0.84
$E_{0,}$ MPa	50
A_e	(142.9+0.14*T)* $f(\varepsilon_{vol}^{in})$
σ_0	0.1
α	0.25
X_0	-0.1
R	0.436
W	0.068+1.57e-4*exp(T/102.7)
D_1	6.2e-3
D_2	4.4e-4
C_1	8.44e12
C_2	4.92
C_3	-1.454
C_4	4.66e4

Note: The units of stress, strain and temperature are MPa, % and ^oC.

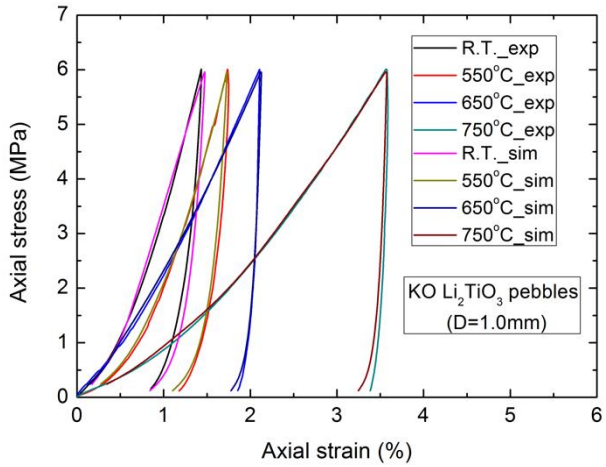

Figure 6.13. Stress-strain relation comparison of KO Li_2TiO_3 pebble bed.

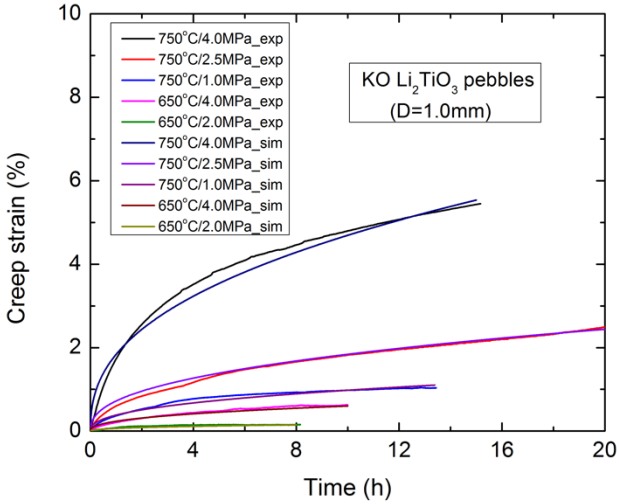

Figure 6.14. Creep strain evolution comparison of KO Li_2TiO_3 pebble bed.

6.2.4. Instructions for the Plotting of ANSYS CAP Model Yield Surface

This work is to provide the instructions for the yield surface plotting of CAP model embedded in ANSYS, and its schematic and governing equations are shown below. The uniaxial compaction test of KO Li_2TiO_3 pebble bed is chosen as the example. The CAP yield surface evolution is plotted in the plane of I_1 ($=\sigma_1+\sigma_2+\sigma_3$) and $\sqrt{J_2}$ ($=\sigma_{von}/\sqrt{3}$).

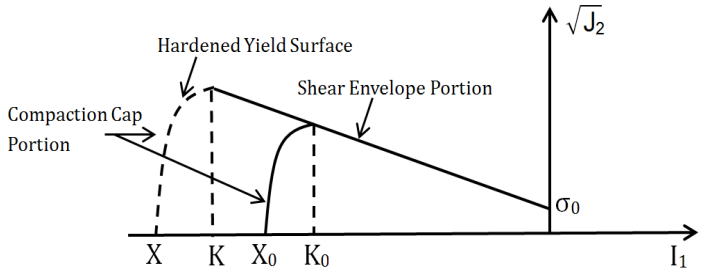

Figure 6.15: Schematic of CAP model.

$$Y(I_1, J_2, K, \sigma_0) = J_2 - Y_c(I_1, K, \sigma_0) Y_s^2(I_1, \sigma_0) \tag{6.15}$$

$$Y_s(I_1, \sigma_0) = \sigma_0 - \alpha I_1$$

$$Y_c(I_1, K, \sigma_0) = 1 - H(K - I_1)\left[\frac{I_1 - K}{R Y_s(K, \sigma_0)}\right]^2$$

Plotting of stress location

With the help of ANSYS FEM simulation of uniaxial compaction test, the stress state for different axial loads can be obtained and listed in Table 6.3. The I_1 and $\sqrt{J_2}$ columns can be used to identify the stress locations in the I_1 - $\sqrt{J_2}$ plane.

Table 6.3: Stress state for different axial loads

Axial stress (MPa)	σ_1 (MPa)	σ_2 (MPa)	σ_3 (MPa)	σ_{von} (MPa)	I_1 (MPa)	$\sqrt{J_2}$ (MPa)
-1.08	-0.30	-0.30	-1.08	0.78	-1.68	0.45
-2.04	-0.54	-0.54	-2.04	1.50	-3.12	0.87
-3.00	-0.84	-0.84	-3.00	2.16	-4.68	1.25
-4.08	-1.18	-1.18	-4.08	2.90	-6.44	1.67
-5.04	-1.48	-1.48	-5.04	3.56	-8.00	2.06
-6.00	-1.78	-1.78	-6.00	4.22	-9.56	2.44

Plotting of shear failure line

The shear failure line can be plotted with the shear failure function (Y_s) defined in Equation 6.15. For the example case, the values of σ_0 and α are 0.1MPa and 0.25, respectively. Therefore, the following equation has been used to plot the shear failure line.

$$\sqrt{J_2} = 0.1 - 0.25 I_1 \qquad (6.16)$$

Plotting of CAP surface

In order to plot the cap portion, the values of X and K, indicated in Figure 6.15, for different axial loads need to be determined first. The yielding function defined by Eq. 1 can be reformed as the following (Eq. 3) by applying the condition of $H(K - I_1)$ =1 (CAP portion). The values of K for different axial loads can be obtained by applying the values of I_1 and $\sqrt{J_2}$, listed in the Table 6.3, to Equation 6.16 and solving for K. Then the X values can be obtained as well with Equation 6.17. The results of K and X for the sample case are shown in Table 6.4. Finally, the yield surface of CAP portion can be plotted using Equation 6.17 for the I_1 range of $[X, K]$.

$$\sqrt{J_2} = \sqrt{1 - [\frac{I_1 - K}{R(\sigma_0 - \alpha K)}]^2}\,(\sigma_0 - \alpha I_1) \qquad (6.16)$$

$$= \sqrt{1 - [\frac{I_1 - K}{0.436 * (0.1 - 0.25 K)}]^2}\,(0.1 - 0.25 I_1)$$

$$X = K - R * (\sigma_0 - \alpha K) \qquad (6.17)$$

Table 6.4: X and K values for different axial loads

Axial stress (MPa)	X (MPa)	K (MPa)
-1.08	-1.78	-1.57
-2.04	-3.43	-3.05
-3.00	-5.12	-4.58
-4.08	-7.02	-6.30
-5.04	-8.71	-7.82
-6.00	-10.40	-9.34

With the plotting of all the data mentioned above, the stress position and CAP yield surface are illustrated in Fig. 6.16 for the sample case.

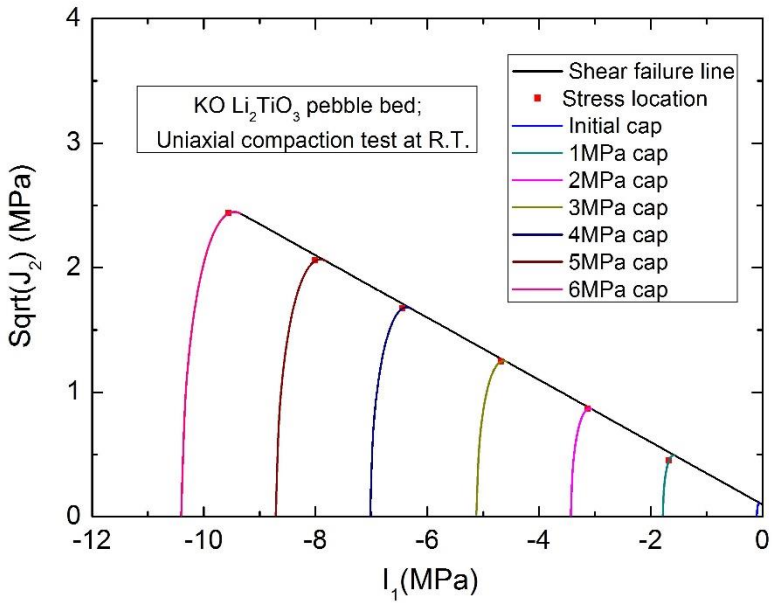

Figure 6.16: CAP yield surface and stress state for the uniaxial compaction test.

6.3. FEM model development and methodology

After deriving the material models parameters, a sequentially-coupled transient thermal-structural model was built in the ANSYS workbench environment as illustrated in Figure 6.17. The test box and the pebbles were modeled as two separate geometries in SolidWorks and imported into ANSYS Design Modeler in Parasolid format where further cleaning and defeaturing of the geometries was performed. Command objects that allow coding in ANSYS Parametric Design Language (APDL) were added to the setup/preprocessing section of the model. In the command line, coupled-field SOLID227 tetrahedral elements that solve for thermal and structural degrees of freedom were defined. Each element contains 10 nodes and is combined with thousands of other elements to form a fine mesh that is best-suited for nonlinear thermo-mechanical analyses. Mesh sensitivity analysis has been performed until the results became within 0.001 relative error for a highly refined mesh of 576,541 elements. Figure 6.18 (right) illustrates a snapshot of the mesh used.

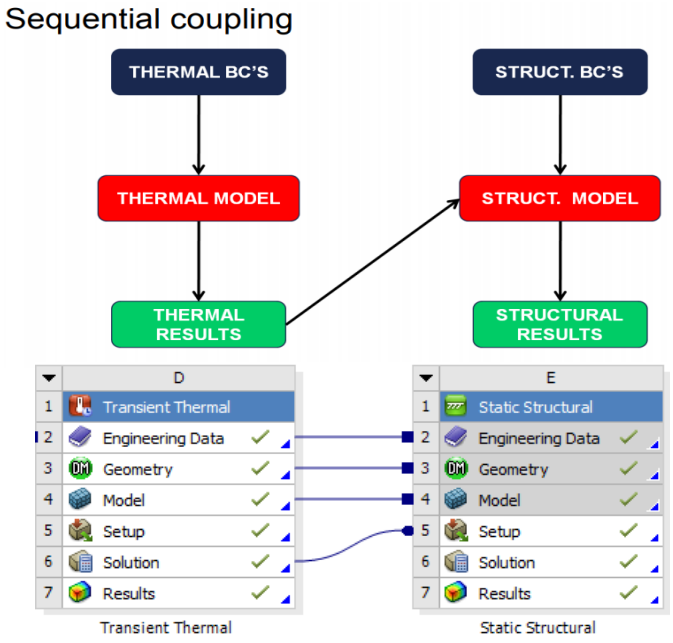

Figure 6.17: Sequential thermo-structural coupling in the ANSYS workbench environment

Effective temperature-dependent material properties have been applied for both the pebbles and the structural materials. The thermal boundary conditions applied include heat generation loads in tabular form due to nuclear heating, in addition to convection boundary conditions at the internal walls of the coolant channels with constant helium bulk temperatures and an approximated mean heat transfer coefficient of 2000 W/m^2 K. Two of the box edges have been fixed to avoid free rolling conditions. Furthermore, frictional contact elements have been defined at the interface between the box and pebbles to with a pre-defined interface thermal resistance. Standard earth gravity has also been included.

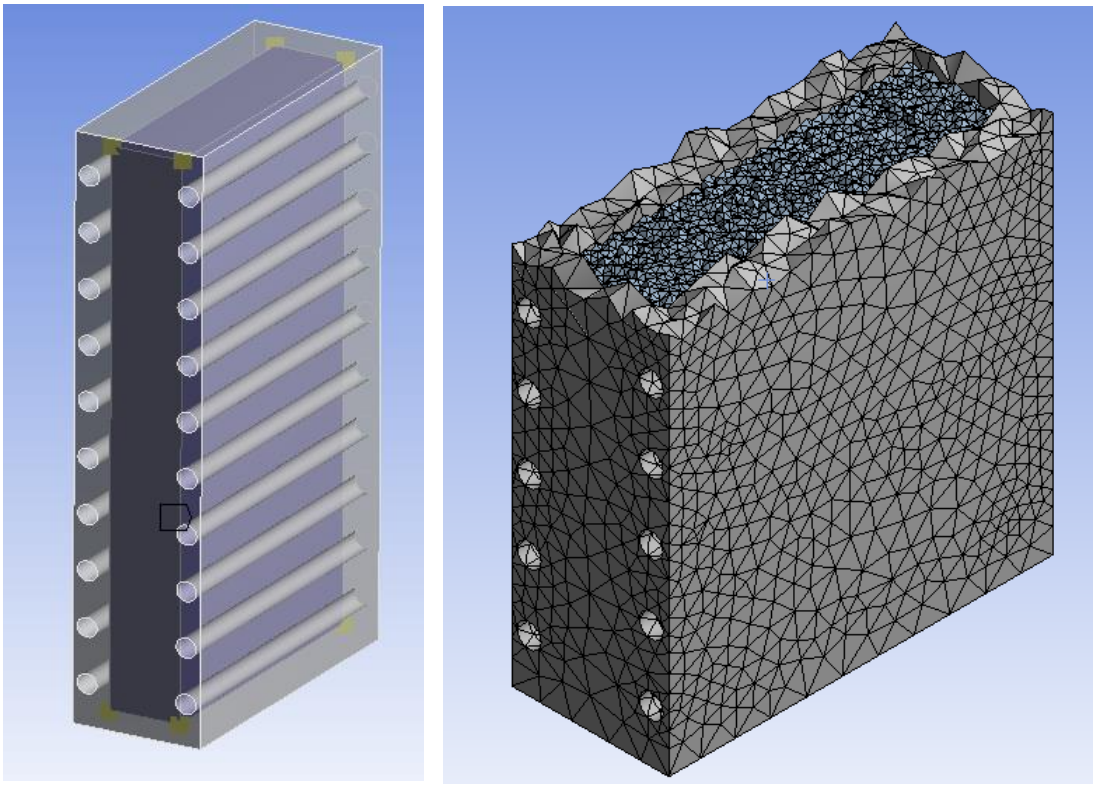

Figure 6.18: TESOMEX pebbles and box CAD (left). Refined tetrahedral mesh elements sectional view through the center plane (right).

Figure 6.19 (left) summarizes the high-level model tree with the aforementioned model development steps: CAD building, geometrical features cleaning, contact elements definitions, mesh building and refinement, transient thermal boundary conditions definition and analysis settings, thermal loads importing and structural analysis setup, followed by the solution and results presentation. An example of the command line objects used to define the material models, their parameters and all thermo-physical material properties is shown in Figure 6.19 (right). Appendix B provides the detailed codes used for building the material models.

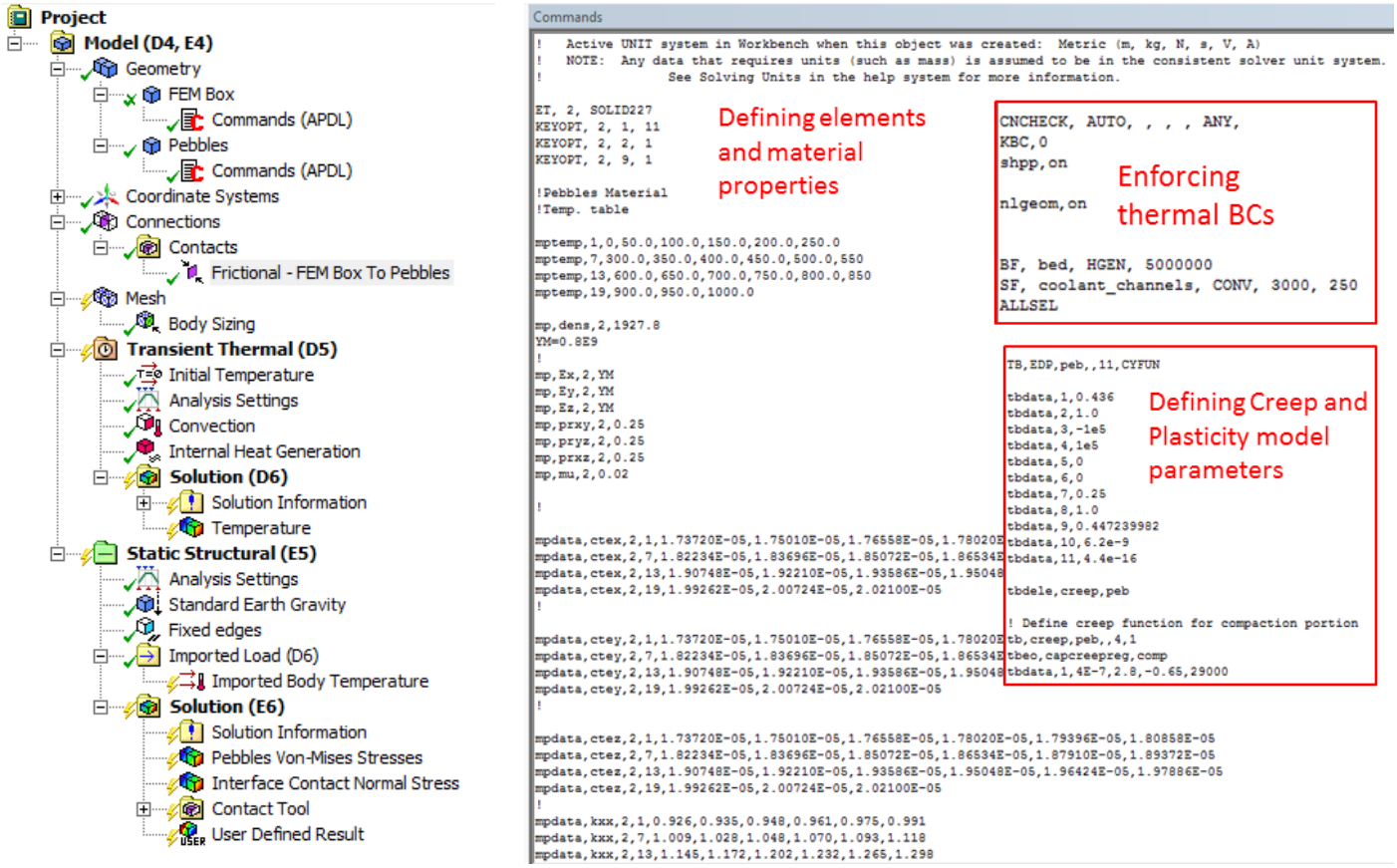

Figure 6.19: Model tree and ANSYS Parametric Design Language (APDL) command object

The same strain hardening creep model which uses Equation 6.10 highlighted in Section 6.2.2 of this work has been used. However, the material model parameters have been updated to fit the ANSYS workbench environment and units system used therein. The experimental data for different stress levels and temperatures was curve-fitted to re-derive the creep model parameters C_1, C_2, C_3, and C_4 as showing in Figure 6.17 and Table 6.5.

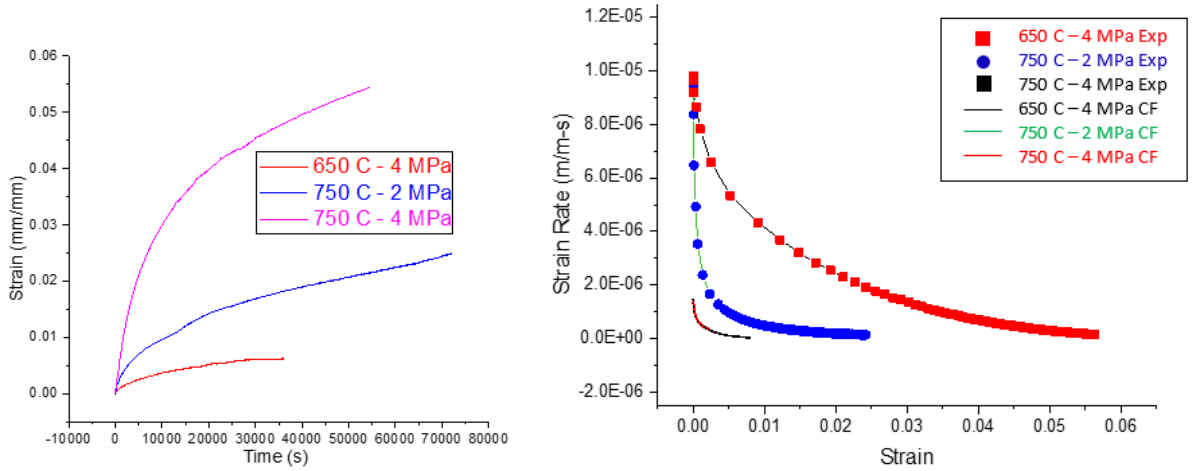

Figure 6.17 Strain hardening creep model parameters ANSYS Workbench re-calibration

Table 6.5: Strain hardening creep material model parameters

Parameter	Value
C_1	0.0002
C_2	2.8
C_3	-0.65
C_4	18000

6.4. FEM model validation against TESOMEX experiments

Figure 6.18 shows remarkable agreement with experimental data. The simulation results (right) for contact stresses at the pebbles/wall interface matched both the magnitudes and spatial distribution of the sensor measurements. The sensor's maximum contact stress measurement at the peak of the first thermal cycle and maximum bed temperature 860 °C was 220 kPa compared to 207 kPa for the model (left). Additionally, the location of the high contact stress zone is near the bottom center for both the simulation and experiment due to gravity effects which enhance the packing of pebbles near the bottom of the test article. After validating the contact stresses at the interface, results were scoped to the center of the bed showing the maximum stress of 1 MPa at the highest temperature location, as expected, corresponding to a 207 kPa contact stress at the coolant wall.

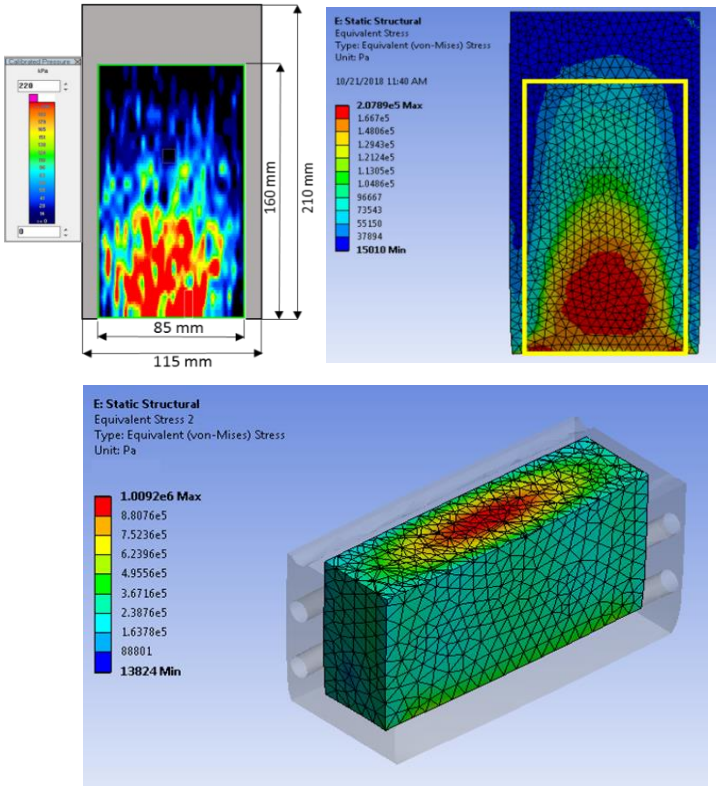

Figure 6.18 Contact stress validation and Equivalent (von-Mises) stress extrapolation

The 24-hr experimental campaign was also used to validate the model and the results are shown in Figure 6.19. The simulation ran for 24 hrs at the same heating rate as the experiment and the behavior of stress build-up and relaxation was recorded. The peak contact stress for the simulation is 129 kPa, compared to 120 kPa for the experiment. Moreover, creep results in a similar effect of gradual reduction of stresses as observed in the experiments. However, the simulations show a steeper decline since the bed temperature remains at the high temperature (820 °C) throughout the simulation time which maintains a higher creep strain rate than that of the experiment. The critical stress relaxation temperature T_{sr} was around 750 °C – agreeing with experiments.

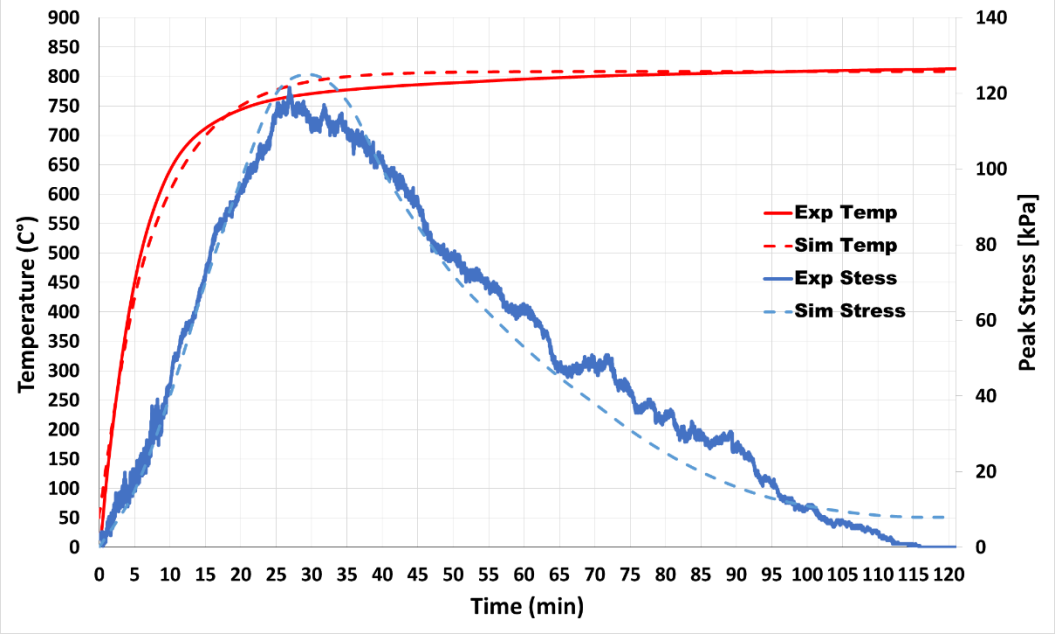

Figure 6.19 First 2 hours thermo-mechanical evolution transient simulation analysis

The overall model results are extremely promising and encourage further numerical enhancement to prepare for incorporation with blanket-scale FEM models.

6.5. Model opportunities and limitations

What the model can predict:

- Quantify and map out the spatial and temporal stress distributions and evolution of the first thermal cycle as well as for continuous operation, which is experimentally proven to capture the maximum stress the bed will experience during operation.

  Value: Accurately predict and extrapolate the stress results to every point in the bed after validating the interface stress distributions with experiments, which can (1) guide blanket designers in determining geometrical features, sizing components and selecting materials, and (2) predict failure of pebbles (crushing) or pebble bed (dimensional instability).

- Spatial and temporal creep strain/stress relaxation evolution.

  Value: locate regions with high propensity of sintering and correlate creep strain with the volume % of sintered pebbles from experiments. If creep is unavoidable, the model can predict the magnitude of creep deformation and assess what percentage of creep strain can be tolerated. Figure 6.20 shows an example of the model predicting the equivalent creep strain magnitude and location as expected at the hot-temperature region of the pebble bed at the end of the 2^{nd} hour of the continuous operation experiment.

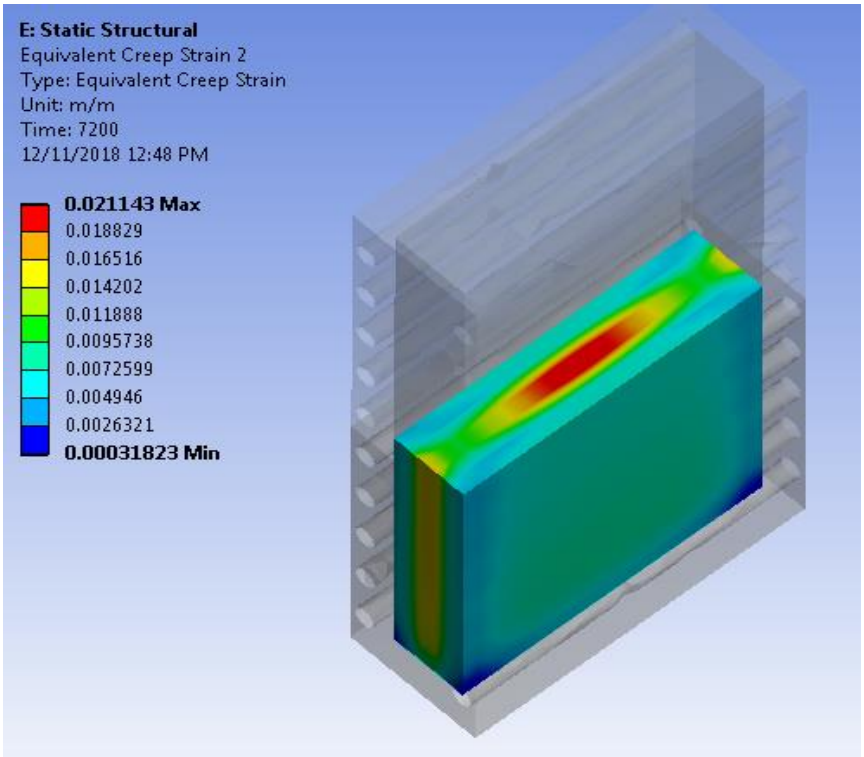

Figure 6.20 Equivalent creep strain simulation results showing magnitude and location of areas with high probability of sintering

What the model does NOT capture (due to inherent limitations of FEM and chosen material models):

- Impact of irreversible plasticity on bed/structure separation under pulsed operation is not accurately captured with FEM. When the bed separates, it does so as a whole (effects of pebbles resettling and rearrangement is not considered)
- Helium purge gas flowing effects.
- Bed/wall separation thermal effects (sequential coupling pre-determines and imposes bed temperature onto the mechanical model, not the other way around).

Chapter 7

7. Conclusion

7.1. Summary

Substantial advancement has been achieved in enriching the scientific understanding of fusion ceramic breeder pebble beds' thermo-mechanical behavior under prototypical reactor operations. The work started with developing a volumetric heating technique to recreate the external excitation source of the fusion reactor represented by the neutronic heat deposition. After exploring various methods of bulk heating, the power-optimized rod heaters scheme's ability to recreate temperature distributions characteristic of volumetric heating was proven to be the most practical scheme for use in the out-of-pile laboratory experiments. The experiments were carried out using a high-temperature working fluid Paratherm (~300 °C) for the heat rejection as well as maintaining coolant-containing wall temperature boundary. Thermocouples were strategically placed in the bed at locations where temperatures are likely to be affected by reactive mechanical response of the pebbles. The measured temperature evolution provided additional evidence/data for a deeper understanding of thermomechanical interaction and synergistic effects. The work provides a novel instrumentation scheme, proves important hypotheses regarding the competing thermo-mechanical forces and the importance of multiple-effects experiments, discovers and analyzes desirable self-stabilization mechanisms, and proposes updating the conventional representation of bed effective thermal conductivity.

A comprehensive picture of the stress distribution and evolution with time and thermal cycling inside the pebble bed was captured and carefully investigated. Unlike traditionally used

strain gauges which generally provide limited/insignificant information in pebble bed mock-up experiments, the tactile pressure sensor allowed for obtaining a complete picture of real-time/in-situ data of stress distribution and evolution with thermal cycling inside the pebble bed. The real-time in-situ spatial and temporal thermo-mechanical interactions and evolution were captured under reactor-relevant conditions for the first time using this novel tactile pressure sensor technology as the bed was volumetrically heated up to creep-relevant temperatures. Two types of bed-wall contact pressure drop were recorded: (1) within the subsequent cycles due to pebbles irreversible rearrangements, and (2) within the cycle itself as a result of creep/stress-relaxation. The measured stresses were self-generated, unlike previous experiments where an external force has to be applied on the bed. Consistently, by the fourth thermal cycle, the contact pressure drops to negligible values and remains stable. This stability is attributed to two modes of self-regulation: (1) stress self-regulation as a result of pressure rise and fall due to thermal expansion and creep/thermal cycling, respectively, and (2) temperature self-regulation due to the locally enhanced thermal conductivity in the core region of the bed accompanied by deteriorated interface conductance. These two mechanisms are desirable as they lower the probability of the events of pebbles crushing and further sintering/creep deformation and thermal runaways under high temperatures and poor heat extraction.

The results presented in this work showed that the use of bed effective thermal conductivity derived from a single packing density needs to be reevaluated since the thermal conductivity is not only a function of temperature and pressure, but it also varies greatly with the spatial distribution in the bed for two key reasons: (1) The pebble bed is more densely packed near the bottom under the effect of gravity, with the top region having minimal to no force contact with the coolant walls. This effect is amplified after the first cycle pressure drop and is clearly demonstrated by the results

of pressure mapping distribution. (2) The local thermal conductivity in the creep zone becomes higher than the normally derived bed conductivity due to pebbles necking together, which enables the bed to reach stable temperatures with a flatter profile.

Pebble bed pre-conditioning mechanisms have been investigated as part of the filling procedure and shown high promise of improving packing density and hence TBR and thermo-mechanical stability and predictability. A formal pre-conditioning procedure has been outlined as a necessary step towards defining control methodologies that enable us to reach an optimal initial packing configuration that allows for safe operation within the design margins.

A 3D, fully-coupled thermo-mechanical volumetrically-heated, transient breeder cell Finite Element Model capable of simulating continuous thermal cycles to reach stress-saturation levels has been developed and validated against current experiments. The model incorporates all previously validated single-effect material models, permitting the analysis of many synergistic effects of a solid breeder in a typical fusion environment. With the developed material models, Finite Element Analyses of structures containing pebble beds can be performed and incorporated with large-scale blanket models. In the present phenomenological model, the thermo-mechanical response of a pebble bed was represented by a nonlinear elasticity law, a modified Drucker-Prager plasticity model, a creep model and temperature-dependent physical properties. The material parameters in the phenomenological model have been successfully identified from the available experimental results. Finally, a benchmark exercise has been carried out on the basis of the present phenomenological model. The results from the simulation have been compared to the experimental data, showing that the present modelling is suitable for thermo-mechanical analyses of fusion blankets. The combination of data output from the TESOMEX program experiments and modeling

advancements allows for a significant improvement in understanding and predictive capabilities of solid breeder pebble bed thermo-mechanics.

7.2. Closing Remarks & Recommendation for Future Work

The goal of this research effort was to explore methods for simulating volumetric heating, and to investigate the thermo-mechanical behavior of ceramic breeder pebble bed blankets in the presence of volumetric heating and resultant temperature gradients representative of the fusion nuclear environment. The main focus was to use a combination of first-of-a-kind experiments and modeling efforts to answer the key questions pertaining to ceramic breeder pebble beds prototypical operation stability and reliability. TESOMEX is the first out-of-pile experiment that provides data with regards to thermal and mechanical interactions within a solid breeder cell. TESOMEX results proved our hypotheses pertaining to the interacting physics between creep, plastic rearrangements, pebbles resettling, and thermal cycling, besides capturing, with high granularity, the desirable self-regulation mechanisms and steep temperature gradient smoothing. Nevertheless, due to many of the limitations discussed in Sections 5.5 and 6.5, there is still room for improvement in order to reach more conclusive results that directly generalize to accurate magnitudes for blanket prototypical bed behavior. The findings of this work provide a comprehensive framework and guiding objectives to pave the way for "Next-Generation" ceramic breeder mock-up experiments, which are still needed in order to recreate a closer behavior to ideal reactor design and operations. The following key points on both the experimental as well as the modeling fronts need to be addressed in future mock-up solid breeder efforts:

On the experimental side:

- The current test box was not designed with the heating technique utilized in the experiments as there were not enough resources to support reconstruction of a related test box. Increasing the width of the pebble bed test box to be consistent with heating scheme and heat conductance of the bed could yield potential benefits, including:

  a) Lowering the heaters to pebbles volume ratio which minimizes the packing disturbances.

  b) Allowing for operating at a lower wall temperature and reduce the risk of damaging the pressure sensor.

  c) Increasing the allocated space for connections that accommodate thermocouples, heaters, purge gas lines, pressure sensors and filling holes.

However, those benefits may also come with the cost of: a) deviating from the prototypical nuclear temperature profile since the transient behavior will differ as the heat will take longer to diffuse from the surface of the heaters to the coolant walls in a low thermal diffusivity environment, and b) the temperature gradient will be much steeper than that of the nuclear gradient if the wall temperature is to be kept at the maximum operating temperature of the sensor. Therefore, careful investigations have to take place in order to reach an optimal box design that balances the above trade-offs.

- Increasing the safe operating temperature of the Tactile Pressure Mapping system to > 300^{o}C would enable us to run experiments for longer periods and at higher bed temperatures more consistently for a more relevant thermo-mechanics investigation. Unfortunately, however, at the time of writing this document, there are no manufacturers that produce similar sensors that can withstand temperatures over 200 ^{o}C. To reach 300 ^{o}C, during TESOMEX experiments,

flexible Silica sheets were used to thermally shield the sensor within thickness limit that is able to translate the forces and not take up much of the limited bed volume. Even with the employed precautions, 5 expensive sensors were completely damaged. Therefore, any future improvements in the high-temperature tactile pressure sensing technology could yield remarkable experimental benefits.

- Identifying and procuring robust, smaller diameter, high temperature and wattage capability heaters (~ 1000°C) would enable more reliable high-temperature operation. Without an exception, all the heaters used in the TESOMEX campaigns have failed at 850 °C, with some failing more prematurely than others. US and Korean manufacturers do not have off the shelve heaters that comply with our experiments specifications. Therefore, custom orders have to be made and carefully designed at a premium and with no manufacturers' guarantees on safe operation. Hence, future efforts to procure and design the required heating techniques at a reasonable cost are of interest.
- Due to the design of the test article box and flange connections, it was increasingly difficult to create a vacuum to run experiments under flowing helium conditions and at the same time accommodate the thermocouples, heaters, and pebble filling hole connections. In a new design, if all the sealed connections are adequately allocated to securely run experiments in a Helium gas environment, the effective thermal conductivity of the bed as well as the interface conductance will be higher and more representative of the actual breeder conditions.
- Other general experimental improvements may include: better defining pebble filling hole locations to ensure uniform packing, and b) incorporating double flanges at the top to separate the bed's physical boundary from the lead-wire penetrations boundary and have a clear solid upper boundary inside the bed.

On the modeling front:

- Since the impact of irreversible plasticity on bed/structure separation under pulsed operation is not accurately captured with FEM, the possibility of using an Adaptive (moving) Mesh technique to model the pebble bed evolution and pebbles rearrangement has to be explored. Currently this technique is exhaustively expensive from a computational point of view, cannot be run at scale, and does not allow thermo-mechanical analyses. Future studies on the feasibility of developing codes that use a similar approach at a lower computational cost that allows for coupled analyses can significantly improve FEM predictive capabilities.
- Direct coupling of simultaneous thermal and structural analyses through coupled-field elements and feedback loops is essential to accurately modeling bed/wall separation thermal effects (sequential coupling pre-determines and imposes bed temperature onto the mechanical model). Currently, directly-coupled thermo-mechanical analyses with pebble bed material models at scale would require enormous computational resources in addition to overcoming consistent numerical convergence issues. Also, the material models used for pebble bed modeling do not inherently allow direct thermo-mechanical coupling and are incompatible with coupled-field elements. Therefore, there is a lot of room for improvement in the area of simultaneously-coupled pebble bed FEM models.
- Lastly, the possibility of developing FEM/DEM coupled models can overcome the limitations of each method and combine the advantages that each has to offer. The microscopic effects that DEM captures can be complimented with the continuum approach's benefits as discussed in detail in Chapter 2 of this document. However, current models need to be improved and more effects have to be taken into account before exploring DEM/FEM coupling methods.

Appendix A. Experimental Matrix

Experiment #	Heater Type	Total Power [W]
1	Wire (NiCr)	920 W
2	Wire (NiCr)	1050 W
3	Wire (NiCr)	2250 W
4	Plate (SiN)	720 W
5	Plate (SiN)	850 W
6	Small Rod (Inconel)	1330 W
7	Small Rod (Inconel)	1450 W
8	Small Rod (Inconel)	1620 W
9	Large Rod (Inconel)	1664 W
10	Large Rod (Inconel)	1856 W
11	Large Rod (Inconel)	1837 W
12	Large Rod (Inconel)	1377 W
13	Large Rod (Inconel)	1562 W
14	Large Rod (Inconel)	1364 W

Appendix B. ANSYS APDL Code

Commands for box material properties:

! Commands inserted into this file will be executed just after material definitions in /PREP7.

! The material number for this body is equal to the parameter "matid".

! Active UNIT system in Workbench when this object was created: Metric (m, kg, N, s, V, A)

! NOTE: Any data that requires units (such as mass) is assumed to be in the consistent solver unit system.

! See Solving Units in the help system for more information.

wall=matid

!Temp. TESOMEX results proved our hypothesis

mptemp,1,0,50.0,100.0,150.0,200.0,250.0

mptemp,7,300.0,350.0,400.0,450.0,500.0,550

mptemp,13,600.0,650.0,700.0,750.0,800.0,850

mptemp,19,900.0,950.0,1000.0

```
!*******************
!Wall material
!*******************
mp,dens,wall,7730
mp,prxy,wall,0.3
mp,pryz,wall,0.3
mp,prxz,wall,0.3
mp,mu,wall,0.02
!
mpdata,ex,wall,1,2.06E11,2.06E11,2.01E11,1.94E11,1.94E11,1.88E11
mpdata,ex,wall,7,1.88E11,1.85E11,1.815E11,1.815E11,1.78E11,1.78E11
mpdata,ex,wall,13,1.78E11,1.75E11,1.63E11,1.51E11,1.51E11
!
mpdata,ey,wall,1,2.06E11,2.06E11,2.01E11,1.94E11,1.94E11,1.88E11
mpdata,ey,wall,7,1.88E11,1.85E11,1.815E11,1.815E11,1.78E11,1.78E11
mpdata,ey,wall,13,1.78E11,1.75E11,1.63E11,1.51E11,1.51E11
!
mpdata,ez,wall,1,2.06E11,2.06E11,2.01E11,1.94E11,1.94E11,1.88E11
mpdata,ez,wall,7,1.88E11,1.85E11,1.815E11,1.815E11,1.78E11,1.78E11
mpdata,ez,wall,13,1.78E11,1.75E11,1.63E11,1.51E11,1.51E11
!
```

mpdata,c,wall,1,448.85,462.76,484.11,503.92,523.04,542.34

mpdata,c,wall,7,562.69,584.94,609.96,638.61,671.75,710.25

mpdata,c,wall,13,754.96,754.96,754.96,754.96,754.96

!

mpdata,kxx,wall,1,25.90,25.90,27.00,27.00,28.10,28.10

mpdata,kxx,wall,7,28.80,28.8,29.20,29.2,29.20,29.2

mpdata,kxx,wall,13,29.2,29.2,29.2,29.2,29.2

!

mpdata,kyy,wall,1,25.90,25.90,27.00,27.00,28.10,28.10

mpdata,kyy,wall,7,28.80,28.8,29.20,29.2,29.20,29.2

mpdata,kyy,wall,13,29.2,29.2,29.2,29.2,29.2

!

mpdata,kzz,wall,1,25.90,25.90,27.00,27.00,28.10,28.10

mpdata,kzz,wall,7,28.80,28.8,29.20,29.2,29.20,29.2

mpdata,kzz,wall,13,29.2,29.2,29.2,29.2,29.2

!

mpdata,alpx,wall,1,1.040E-05,1.040E-05,1.080E-05,1.080E-05,1.120E-05,1.120E-05

mpdata,alpx,wall,7,1.160E-05,1.160E-05,1.190E-05,1.190E-05,1.220E-05,1.220E-05

mpdata,alpx,wall,13,1.250E-05,1.250E-05,1.250E-05,1.250E-05,1.250E-05

!

mpdata,alpy,wall,1,1.040E-05,1.040E-05,1.080E-05,1.080E-05,1.120E-05,1.120E-05

mpdata,alpy,wall,7,1.160E-05,1.160E-05,1.190E-05,1.190E-05,1.220E-05,1.220E-05

mpdata,alpy,wall,13,1.250E-05,1.250E-05,1.250E-05,1.250E-05,1.250E-05

!

mpdata,alpz,wall,1,1.040E-05,1.040E-05,1.080E-05,1.080E-05,1.120E-05,1.120E-05

mpdata,alpz,wall,7,1.160E-05,1.160E-05,1.190E-05,1.190E-05,1.220E-05,1.220E-05

mpdata,alpz,wall,13,1.250E-05,1.250E-05,1.250E-05,1.250E-05,1.250E-05

Commands for pebbles material properties and material models

! Commands inserted into this file will be executed just after material definitions in /PREP7.

! The material number for this body is equal to the parameter "matid".

! Active UNIT system in Workbench when this object was created: Metric (m, kg, N, s, V, A)

! NOTE: Any data that requires units (such as mass) is assumed to be in the consistent solver unit system.

! See Solving Units in the help system for more information.

```
!Pebbles


TOFFST,273

TREF,22


peb=matid


!Pebbles Material

!Temp. table


mptemp,1,0,50.0,100.0,150.0,200.0,250.0

mptemp,7,300.0,350.0,400.0,450.0,500.0,550

mptemp,13,600.0,650.0,700.0,750.0,800.0,850

mptemp,19,900.0,950.0,1000.0


mp,dens,peb,1927.8

YM=0.05E9

!

mp,Ex,peb,YM

mp,Ey,peb,YM

mp,Ez,peb,YM

mp,prxy,peb,0.25
```

mp,pryz,peb,0.25

mp,prxz,peb,0.25

mp,mu,peb,0.02

!

mpdata,alpx,2,1,0.758E-05,0.758E-05,0.758E-05,0.758E-05,0.835E-05,0.835E-05

mpdata,alpx,2,7,1.01E-05,1.01E-05,1.21E-05,1.21E-05,1.38E-05,1.38E-05

mpdata,alpx,2,13,1.64E-05,1.64E-05,1.72E-05,1.97E-05,2.22E-05,2.47E-05

mpdata,alpx,2,19,2.47E-05,2.47E-05,2.47E-05

!

mpdata,alpy,2,1,0.758E-05,0.758E-05,0.758E-05,0.758E-05,0.835E-05,0.835E-05

mpdata,alpy,2,7,1.01E-05,1.01E-05,1.21E-05,1.21E-05,1.38E-05,1.38E-05

mpdata,alpy,2,13,1.64E-05,1.64E-05,1.72E-05,1.97E-05,2.22E-05,2.47E-05

mpdata,alpy,2,19,2.47E-05,2.47E-05,2.47E-05

!

mpdata,alpz,2,1,0.758E-05,0.758E-05,0.758E-05,0.758E-05,0.835E-05,0.835E-05

mpdata,alpz,2,7,1.01E-05,1.01E-05,1.21E-05,1.21E-05,1.38E-05,1.38E-05

mpdata,alpz,2,13,1.64E-05,1.64E-05,1.72E-05,1.97E-05,2.22E-05,2.47E-05

mpdata,alpz,2,19,2.47E-05,2.47E-05,2.47E-05!

mpdata,kxx,peb,1,0.926,0.935,0.948,0.961,0.975,0.991

mpdata,kxx,peb,7,1.009,1.028,1.048,1.070,1.093,1.118

```
mpdata,kxx,peb,13,1.145,1.172,1.202,1.232,1.265,1.298
mpdata,kxx,peb,19,1.334,1.370,1.408
!
mpdata,kyy,peb,1,0.926,0.935,0.948,0.961,0.975,0.991
mpdata,kyy,peb,7,1.009,1.028,1.048,1.070,1.093,1.118
mpdata,kyy,peb,13,1.145,1.172,1.202,1.232,1.265,1.298
mpdata,kyy,peb,19,1.334,1.370,1.408
!
mpdata,kzz,peb,1,0.926,0.935,0.948,0.961,0.975,0.991
mpdata,kzz,peb,7,1.009,1.028,1.048,1.070,1.093,1.118
mpdata,kzz,peb,13,1.145,1.172,1.202,1.232,1.265,1.298
mpdata,kzz,peb,19,1.334,1.370,1.408
!
mpdata,c,peb,1,1062,1100,1150.95,1193.09,1233.68,1272.72
mpdata,c,peb,7,1310.21,1346.14,1380.52,1413.35,1444.63,1474.35
mpdata,c,peb,13,1502.52,1529.14,1554.21,1577.72,1599.68,1620.09
mpdata,c,peb,19,1638.95,1656.25,1672.00
```

!Note: the following EDP plasticity function was not used for the results shown in this work. Including this function caused numerical convergence issues and required massive computational/storage resources. Instead, only the strain hardening creep law was used in the workbench environment as outlined in section 6.3.

!EDP Definition for 11 temperatures

TB,EDP,peb,11,11,CYFUN

tbtemp,0

tbdata,1,0.436

tbdata,2,1.0

tbdata,3,-1e5

tbdata,4,1e5

tbdata,5,0

tbdata,6,0

tbdata,7,0.25

tbdata,8,1.0

tbdata,9,0.068157

tbdata,10,6.2e-9

tbdata,11,4.4e-16

tbtemp,100

tbdata,1,0.436

tbdata,2,1.0

tbdata,3,-1e5

tbdata,4,1e5

tbdata,5,0

tbdata,6,0

tbdata,7,0.25

tbdata,8,1.0

tbdata,9,0.068415697

tbdata,10,6.2e-9

tbdata,11,4.4e-16

tbtemp,200

tbdata,1,0.436

tbdata,2,1.0

tbdata,3,-1e5

tbdata,4,1e5

tbdata,5,0

tbdata,6,0

tbdata,7,0.25

tbdata,8,1.0

tbdata,9,0.06910066

tbdata,10,6.2e-9

tbdata,11,4.4e-16

tbtemp,300

tbdata,1,0.436

tbdata,2,1.0

tbdata,3,-1e5

tbdata,4,1e5

tbdata,5,0

tbdata,6,0

tbdata,7,0.25

tbdata,8,1.0

tbdata,9,0.070914272

tbdata,10,6.2e-9

tbdata,11,4.4e-16

tbtemp,400

tbdata,1,0.436

tbdata,2,1.0

tbdata,3,-1e5

tbdata,4,1e5

tbdata,5,0

tbdata,6,0

tbdata,7,0.25

tbdata,8,1.0

tbdata,9,0.075716261

tbdata,10,6.2e-9

tbdata,11,4.4e-16

tbtemp,500

tbdata,1,0.436

tbdata,2,1.0

tbdata,3,-1e5

tbdata,4,1e5

tbdata,5,0

tbdata,6,0

tbdata,7,0.25

tbdata,8,1.0

tbdata,9,0.088430721

tbdata,10,6.2e-9

tbdata,11,4.4e-16

tbtemp,600

tbdata,1,0.436

tbdata,2,1.0

tbdata,3,-1e5

tbdata,4,1e5

tbdata,5,0

tbdata,6,0

tbdata,7,0.25

tbdata,8,1.0

tbdata,9,0.12209542

tbdata,10,6.2e-9

tbdata,11,4.4e-16

tbtemp,700

tbdata,1,0.436

tbdata,2,1.0

tbdata,3,-1e5

tbdata,4,1e5

tbdata,5,0

tbdata,6,0

tbdata,7,0.25

tbdata,8,1.0

tbdata,9,0.211231094

tbdata,10,6.2e-9

tbdata,11,4.4e-16

tbtemp,800

tbdata,1,0.436

tbdata,2,1.0

tbdata,3,-1e5

tbdata,4,1e5

tbdata,5,0

tbdata,6,0

tbdata,7,0.25

tbdata,8,1.0

tbdata,9,0.447239982

tbdata,10,6.2e-9

tbdata,11,4.4e-16

tbtemp,900

tbdata,1,0.436

tbdata,2,1.0

tbdata,3,-1e5

tbdata,4,1e5

tbdata,5,0

tbdata,6,0

tbdata,7,0.25

tbdata,8,1.0

tbdata,9,1.072132272

tbdata,10,6.2e-9

tbdata,11,4.4e-16

tbtemp,1000

tbdata,1,0.436

tbdata,2,1.0

tbdata,3,-1e5

tbdata,4,1e5

tbdata,5,0

tbdata,6,0

tbdata,7,0.25

tbdata,8,1.0

tbdata,9,2.726690191

tbdata,10,6.2e-9

tbdata,11,4.4e-16

tbdele,creep,peb

! Define creep function for compaction portion

tb,creep,peb,,4,1

tbeo,capcreepreg,comp

tbdata,1,2E-4,2.8,-0.65,18000

! Define creep function for shear portion

tb,creep,peb,,4,1

tbeo,capcreepreg,shea

tbdata,1,2E-4,2.8,-0.65,18000

```
/solu

CNCHECK, AUTO, , , , ANY,
KBC,0
nlgeom,on              !Turn on large deflection analysis

RATE,OFF               !Creep analysis turned off
TIME,1.0E-8            !Time period set to a very small value
nsubst,100,1000,10
SOLV                   !Solve this load step


TIME,1
RATE,on     !Turn on creep analysis
nsubst,100,1000,100
solv

TIME,5          !Continue substeps as defined in the workbench analysis settings
environment
RATE,on
nsubst,1000,10000,1000
solv
```

Appendix C. Temperature Gradient Experiments Temperature Control Loop Design and Experimental Procedure

Purpose

The temperature-control loop will serve for the following two main purposes.

(1) To maintain a constant steady state for the upper piston of the thermomechanical test stand at different cycles, which is for minimizing the thermal expansion influence of the upper piston.

(2) To control the transient time during cooling down of the tested pebble bed sample after one cycle. This transient time can be controlled to a desired value.

Method

To realize the above mentioned purposes, a high-temperature liquid, Paratherm Oil with effective working temperature up to 371 °C, will be used as flow medium circulating through the upper and lower pistons. Two Paratherm loops will be designed for the heating up and hot-maintaining stage and the cooling down stage for the pebble bed sample, respectively.

Static thermohydraulic calculations

The arrangement of test section part of pebble bed thermomechanical cycling experimental system is shown in Figure C.1 schematically.

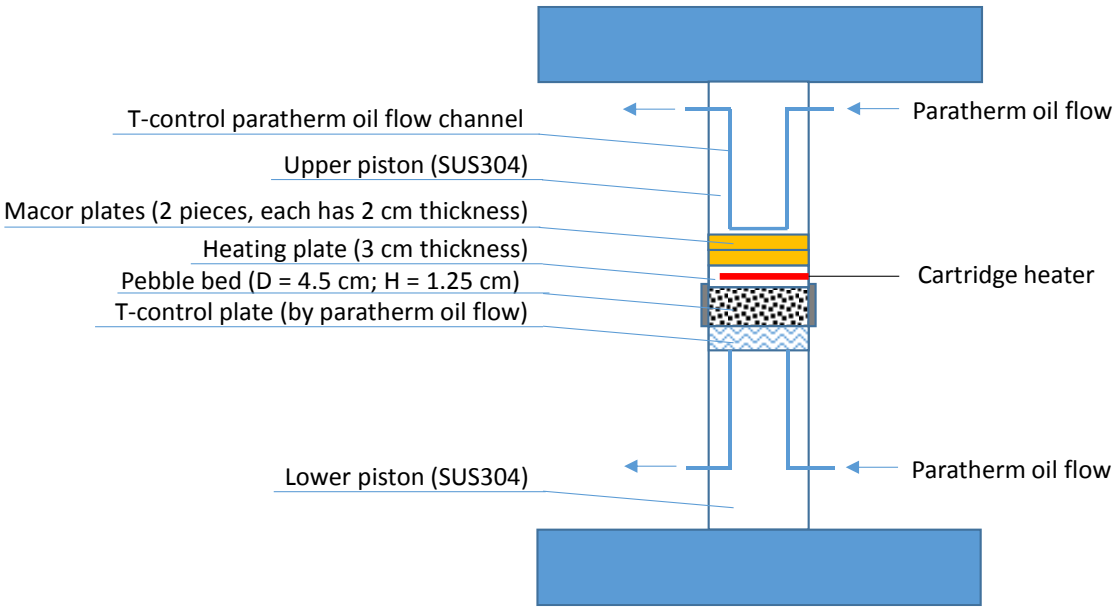

Figure. C.1 Test section of pebble bed thermomechanical cycling experimental system

The supposed working conditions during thermal cyclic operations and the other known parameters are given in Table C.1.

Using the parameters given in Figure. C.1 and Table C.1, the static thermohydraulic characteristics of the pebble bed and paratherm oil flow loops are calculated as follows.

Table C.1 Working conditions and the known parameters

	Temperature of Paratherm flow in the upper piston (constant), T_U	250 °C
	Temperature of Paratherm flow in the lower T-control plate during heating up and hot-maintaining stage, T_{LH}	250 °C
	Temperature of Paratherm flow in the lower T-control plate during cooling down stage, T_{LC}	~ 25 °C
	Net heating power of heating plate (with removal of heat loss), P	~ 30 W (arbitrary)
	Pebble bed effective thermal conductivity, k	0.3 W/m°C
	Pebble bed density (33% packing ratio), ρ	1132 kg/m^3
	Pebble bed heat capacity, c_p	1300 J/kg°C
	Paratherm oil viscosity at 250 °C, ν	0.59×10^{-6} m^2/s
	Paratherm oil heat capacity at 250 °C, c_p	3014.6 J/kg°C
	Paratherm oil density at 250 °C, ρ_P	730 kg/m^3
	Paratherm oil thermal conductivity at 250 °C, λ_o	0.0862 W/m°C
	Pipeline (1/4" pipe) inner diameter and characteristic size of channel in lower T-control plate, D_P	0.1875 inch = 0.476 cm
	Flow velocity in both upper and lower oil loops, V	0.2 m/s (adjustable)
	Thermal conductivity of Macor plate, λ	~ 1.4 W/m°C
	Thermal conductivity of stainless steel 304, λ_s	~ 10.5 W/m°C

Heat capacity of stainless steel 304, c_p	~ 500 J/kg°C
Density of stainless steel 316, ρ_s	~ 8030 kg/m^3

- Take the flow loop through upper piston as a reference to estimate pressure drop.

  Suppose the total pipeline length is 4 m, including 9 elbows, 3 Tees, 2 valves, 3 sudden expansion/contraction joints, 1 flow inlet (from tank), 1 flow outlet (to tank).

  The flow Reynolds number $Re = \frac{0.2 \times 0.00476}{0.59 \times 10^{-6}} = 1613$, indicating the flow is still at laminar state. The total pressure drop through the flow loop,

  $\Delta p = \left(\frac{64}{1613} \times \frac{4}{0.00476} + 9 \times 0.3 + 3 \times 2.0 + 2 \times 1.0 + 3 \times 0.3 + 0.5 + 1.0\right) \times \frac{730 \times 0.2^2}{2} =$ 678 Pa

  Note that, more pipe-fittings could be used in assemble the piping systems and the total length of the piping arrangement could be longer than the assumption of 4 m, resulting in higher pressure drop than the above estimation. However, the total pressure drop will not become orders higher than the estimation at the same flow rate, which will not affect the performance of the key components of flow system, such as the pump.

  If the flow rate is increased 5 times, for example, the temperature increase of Paratherm oil flow through both upper and lower pistons will be decreased 5 times accordingly. The flow state will become turbulent at Re = 8065. Then the total pressure drop through the flow loop becomes,

  $\Delta p = \left(4 \times 0.0791 \times 8065^{-0.25} \times \frac{4}{0.00476} + 9 \times 0.3 + 3 \times 2.0 + 2 \times 1.0 + 3 \times 0.3 + 0.5 + 1.0\right) \times \frac{730 \times 1.0^2}{2} = 15022\ Pa$

It indicates that, for even turbulent flow state at an increased flow rate, the total pressure drop through the flow loop is still within an acceptable range.

Since the temperature boundary conditions for upper piston and lower piston are controlled, and the thermal conductivities for different materials (including the effective thermal conductivity of pebble bed) are known, the temperatures at different locations, as indicated in Figure C.2, can be calculated through the following procedures.

Note that, since we don't have *insitu* measured values of the contact thermal resistances at different interfaces. Rough assumption values are chosen referring to the information from the following link: http://www.thermopedia.com/content/1188/: order of 0.01 m^2°C/W for the interface between Marco plates, half (0.005 m^2°C/W) for the interface between metallic and non-metallic materials, order of 0.001 m^2°C/W between metallic materials. The above assumptions may give some errors to the estimation results. Nevertheless, it may provide some references to the temperatures at different locations.

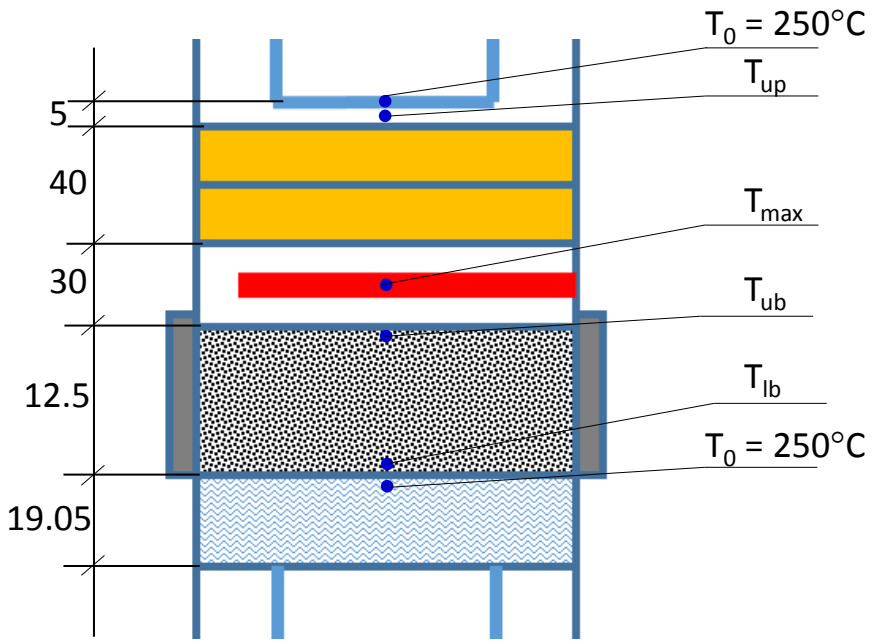

Figure C.2 Schematic showing the details around the tested pebble bed, herein T_{up} represents temperature at the tip of upper piston, T_{mas} temperature at the center of heater, T_{ub} temperature at upper surface of pebble bed, T_{lb} temperature at lower surface of pebble bed, T_0 controlled temperatures for both upper and lower pistons.

- The total heating power will be divided into two parts, one goes downward through the pebble bed and the other goes upward through the Marco plates. The power distributions are determined by the total thermal resistances at two sides of the heater.

  The total thermal resistance between the lower side of heater and the T-control plate is,

  R_L = 0.015/10.5 + 0.005 + 0.0125/0.3 + 0.005 + 0.001 = 0.0541 m^2°C/W.

  The total thermal resistance between the upper side of heater and the upper piston is,

  R_U = 0.015/10.5 + 0.005 + 0.02/1.4 + 0.01 + 0.02/1.4 + 0.005 + 0.005/10.5 = 0.0505 m^2°C/W.

  Therefore, the powers goes to the downward and upward are respectively,

  $$P_L = \frac{P_0 R_U}{R_L + R_U} = 30 \times \frac{0.0505}{0.0541 + 0.0505} = 14.48\ W$$

  $$P_U = P_0 - P_L = 30 - 14.48 = 15.52\ W$$

- Temperature at the heater center,

  $$T_{max} = T_0 + \frac{P_L R_L}{A} = 250 + \frac{14.48 \times 0.0541}{\pi \times 2.25^2 \times 10^{-4}} = 742\ °C.$$

- Temperature at upper surface of pebble bed,

  $$T_{ub} = T_{max} - \frac{P_L}{A} \times \left(\frac{0.015}{10.5} + 0.005\right) = 742 - \frac{14.48 \times 0.00643}{\pi \times 2.25^2 \times 10^{-4}} = 683\ °C.$$

- Temperature at lower surface of pebble bed,

  $$T_{lb} = T_{ub} - \frac{P_L}{A} \times \left(\frac{0.0125}{0.3}\right) = 683 - \frac{14.48 \times 0.0417}{\pi \times 2.25^2 \times 10^{-4}} = 304\ °C.$$

- Temperature at the upper piston tip,

$$T_{up} = T_0 + \frac{P_U}{A} \times \left(\frac{0.005}{10.5}\right) = 250 + \frac{15.52 \times 4.762 \times 10^{-4}}{\pi \times 2.25^2 \times 10^{-4}} = 255\ ^\circ\text{C}.$$

All the calculated temperatures and their corresponding positions are shown in Figure C.3.

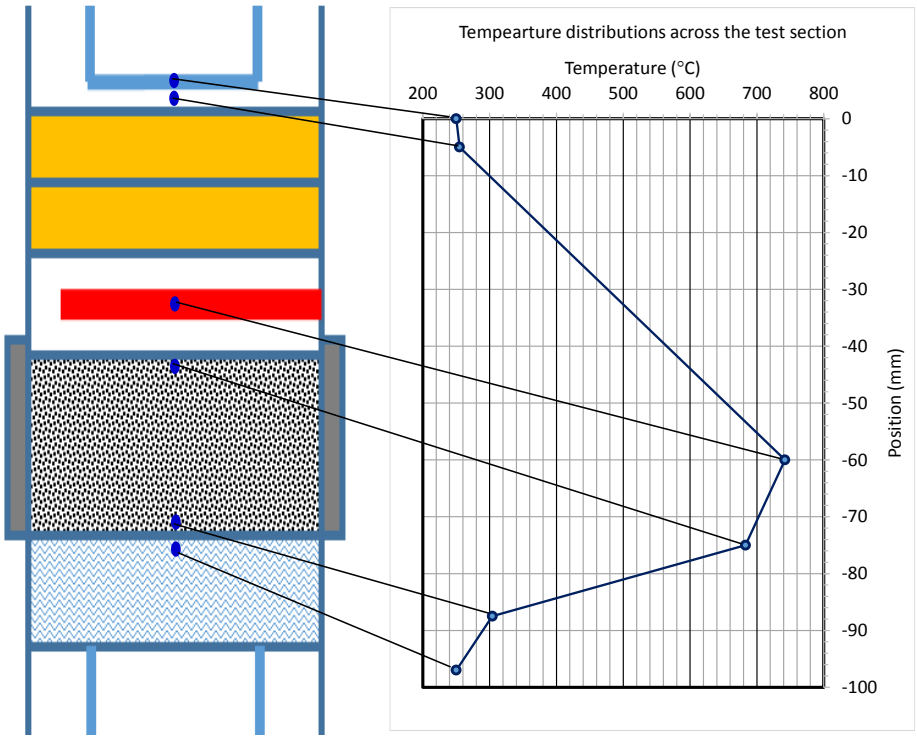

Figure C.3 The estimated temperature distributions at different locations in the test section region, considering contact thermal resistance at all interfaces with assumption values.

- Flow rate of Paratherm in each loop,

$$m = \rho_P V A_P = 730 \times 0.2 \times \pi \times (\frac{0.476}{2})^2 \times 10^{-4} = 2.6 \times 10^{-3}\ \text{kg/s}$$

($Q = 3.56 \times 10^{-6}$ m^3/s = 0.2 LPM)

Note that, the flow rate can be increased since the pump will have enough capacity (both ranges of flow rate and water head), and the increase of flow rate within the allowed range is beneficial to the performance of the T-control system.

- Temperature increase of Paratherm after passing through lower T-controlled plate,

$$\Delta T_L = \frac{P_L}{mc_p} = \frac{14.48}{2.6 \times 10^{-3} \times 3014.6} = 1.8\ ℃$$

- Temperature increase of Paratherm flowing through the upper piston,

$$\Delta T_U = \frac{15.52}{14.48} \times 1.8 = 1.9\ ℃$$

- The estimated Paratherm volume in one loop is less than 1 liter. Therefore, the tank for each loop may have 2 liters in volume.

Transient behavior estimations

During the cyclic experiments, the transient behaviors of the system during two procedures need to be particularly paid attention to. One is the temperature transient behavior of the pistons during heating up procedure at the very beginning of the experiment, since it determines how long time it needs to take to reach steady state for the experiment. The other is the temperature transient behavior of the pebble bed during cooling down procedure, since it determines how long time it needs to take to reach the desired low temperature for the beginning of next cycle of experiment. These two temperature transient behaviors are estimated as follows.

- Estimation of the temperature transition during heating up of upper piston (lower piston may show similar behavior) at the very beginning (without considering heat loss to the environment).

  At the beginning, heating is only due to the flowing of hot Paratherm oil inside the piston (with mass of m_P). The energy equation governing this heat transfer process is (assume negligibly small temperature change of the fluid from inlet to outlet of the piston, and assume constant convective heat transfer coefficient),

  $$\alpha A(T_{oil} - T) = m_P c_P \frac{dT}{dt}$$

  With assumption of uniform wall temperature, Nu = 3.66 for laminar flow. Then the convective heat transfer coefficient can be estimated, $\alpha = 66.3$ W/m^2. The total length of flow channel inside the upper piston ~ 80 cm. Then the heat transfer area is calculated, A = 0.012 m^2. And so the thermal time constant of upper piston can be estimated,

  $$\tau_P = \frac{m_P c_P}{\alpha A} = 3242\ s$$

  Solution of the energy equation can be obtained as,

  $$T(t) = T_{oil} + (T_0 - T_{oil})e^{\frac{-t}{\tau}}$$

  The temperature transition versus time during heating up of the upper piston is shown in Figure C.4. It can be seen that, in order to obtain a steady state (at least an asymptotic steady state), the hot Paratherm flow needs to be run for more than 4 hours before the performance of experiment. Note that, if taking heat loss to the environment into account, this waiting time can be even longer. To shortening this waiting time, an additional heater (such as a rope heater) could be used for the piston.

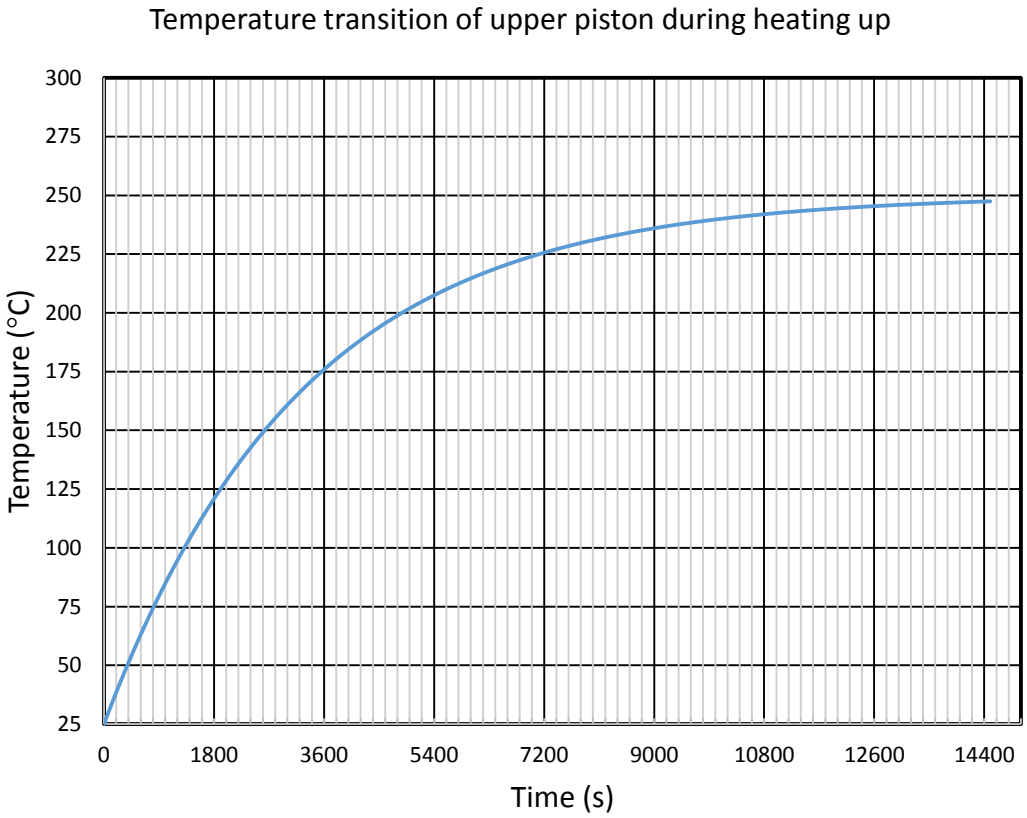

Figure C.4 Temperature variation versus time during heating up of the upper piston at the beginning of preparing experiment.

- Estimation of the temperature transition during cooling down of pebble bed.

  Suppose cooling is only due to heat conduction from high temperature region to low temperature region

  $$\frac{k}{H}A(T_{L0} - T) = mc_P \frac{dT}{dt}$$

  $$\tau = \frac{mc_P}{\frac{k}{H}A} = 706.3\ s$$

$T(t) = T_{L0} + (T_{H0} - T_{L0})e^{\frac{-t}{\tau}}$, where T_{L0} represents the controlled (by Paratherm oil flow) low temperature at the lower surface of pebble bed, and T_{H0} represents the original hottest temperature of pebble bed to be cooled down.

The temperature transition behaviors of the pebble bed during cooling down procedure, at different controlled T_{L0} are shown in Figure C.5. Estimations are made for $T_{H0} = 683$ °C. Apparently, Figure C.5 shows that the cooling down process can be accelerated at a lower temperature of the bottom boundary of the pebble bed.

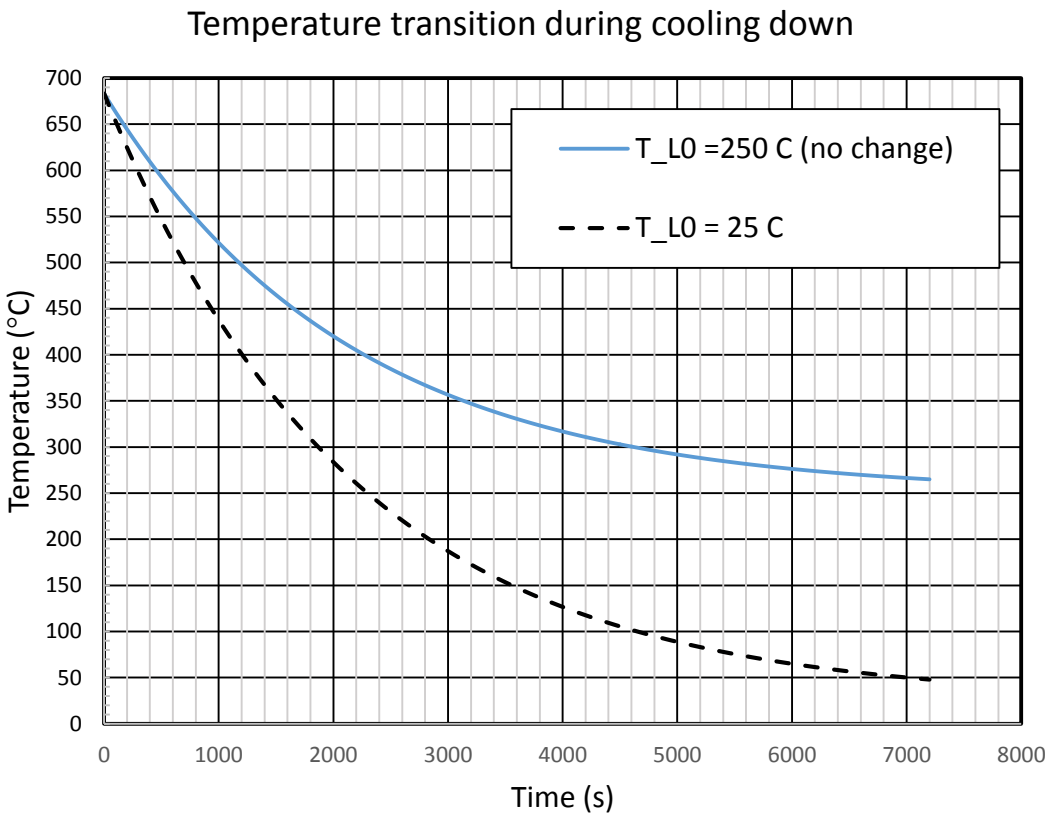

Figure C.5 Temperature variations versus time during cooling down of the hot pebble bed after finishing experiment for one cycle.

T-control loop design sketch and operation procedures

Based on the abovementioned pre-design estimations, and some other considerations about the conveniences for performing experiments, the temperature-control-loop design is finalized, as shown in Figure C.6. The experiment operating procedures are then provided in consequence. The temperature control system consists of two Paratherm oil flow loops. One is for hot Paratherm flow at temperature of 250 °C (flow loop plotted in pink color in Figure C.6), which is adjustable within the upper temperature limitation of 371 °C. The other is for normal-temperature (room temperature 25 °C) Paratherm flow (flow loop plotted in blue color in Figure C.6). Note that part of the blue colored loop (through lower piston and the lower T-control plate) will be also flowed with hot liquid during experimental operation.

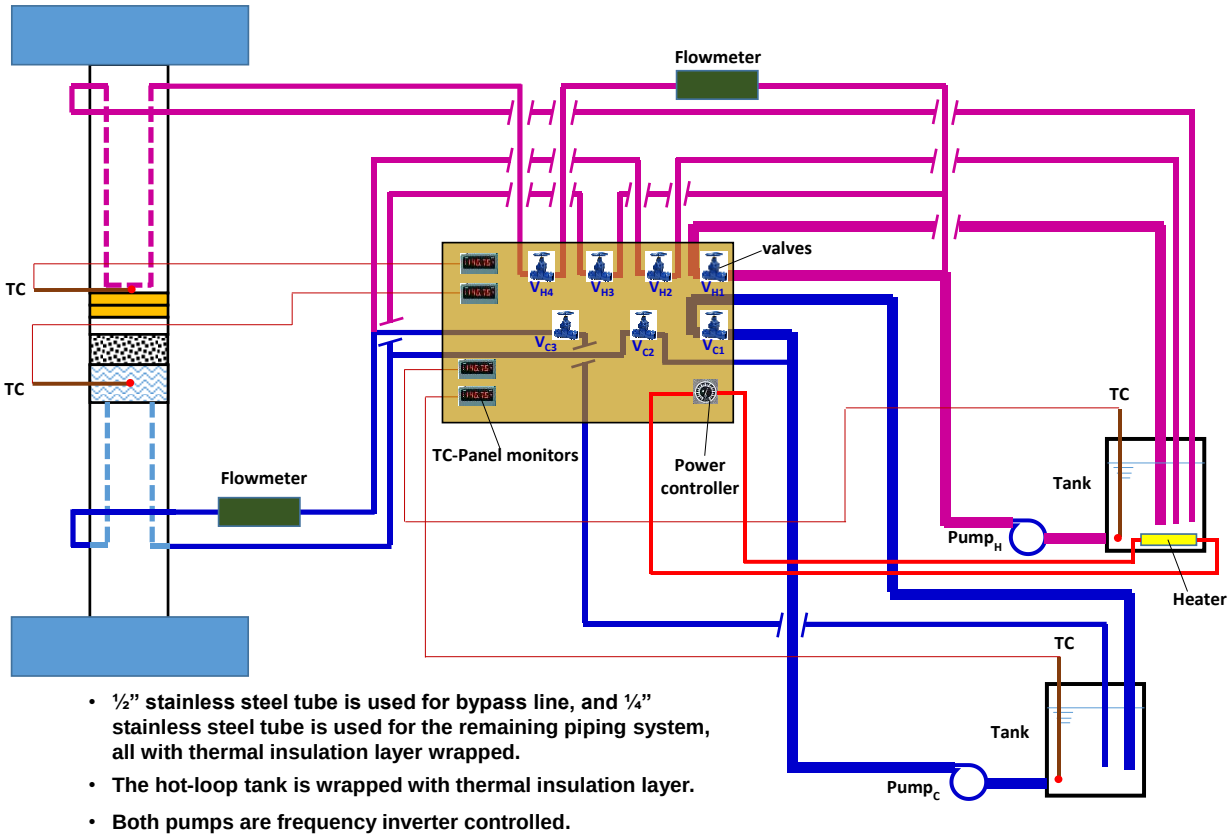

Figure C.6 A schematic showing the Paratherm oil flow loops for temperature control purpose.

The operation procedures of the above designed T-controlling loop for pebble bed thermomechanical cyclic experiment are suggested as follows.

(1) Keep all the valves closed. Turn on the heater in the storage tank of hot loop with full power until the Paratherm temperature in the tank reaches the setup temperature, e.g. 250 °C. Based on the monitored liquid temperature value in the tank, adjust the power input using the Power controller for heater, so as to keep a constant liquid temperature of 250 °C;

(2) Open the valve V_{H1} (by-pass line control valve), turn on the hot loop $pump_H$ at low frequency;

(3) Open the valves V_{H2} (returning line control valve for hot Paratherm flow through the lower piston), and V_{H3} and V_{H4} (supplying line control valves for both hot loops);

(4) Slowly close the valve V_{H1} and adjust the flow rates in both loops until reaching desired values of the flowrates, then stop closing the valve V_{H1}; Note that, in order to get the desired flowrates in the two loops, V_{H3} and V_{H4} may need to be slightly adjusted as well since the flow resistances in the two loops are different;

(5) Keep running the hot Paratherm flow, and monitor the temperatures at the upper piston tip and in the lower T-control plate, until they both approach to an asymptotic steady state temperature (close to 250 °C);

(6) Start pebble bed thermomechanical experiment for the 1st cycle;

(7) After finishing one cycle experiment (turn off the heater at the top of pebble bed), open the valve V_{C1} (by-pass line control valve for cooling loop), turn on the cold loop $pump_C$;

(8) Close the valves V_{H2} and V_{H3}, open the valves V_{C3} (returning line control valve for the cold Paratherm flow through the lower piston) and V_{C2} (supplying line control valve for the cold loop);

(9) Slowly close the valve V_{C1} and adjust the flow rate in the cold flow loop until reaching the desired value of flowrate, then stop closing the valve V_{C1};

(10) Keep running the cold Paratherm flow, and monitor the temperatures in the pebble (Note that, temperature monitoring is not shown in Figure C.6, since it is supposed this temperature should be monitored during thermomechanical experiment), until it approaches to a setup value (e.g., 250 °C);

(11) Start to prepare experiment for next cycle: (turn on the heater at the top of pebble bed) Open the valve V_{H2}, slowly open the valve V_{H3} and adjust the flow rate to be a desired value;

(12) Keep running the hot Paratherm flow in lower piston, and monitor the temperature in the lower T-control plate, until it approaches to an asymptotic steady state temperature (close to 250 °C);

(13) If the pebble bed temperature also reaches its desired value. Start pebble bed thermomechanical experiment for the next cycle;

(14) Repeat steps (7) – (13).

Temperature Gradient Experimental Procedure for Fixed Boundary Configuration

The experiment primarily aims to quantify how much stress is generated by the pebble bed due to the prototypical solid breeder blanket temperature gradients and magnitudes. Preliminary temperature gradient tests have shown that a previous method of estimating a gap distance between the upper piston and the surface of the pebbles before running the experiment introduces a lot of uncertainty. The principal source of ambiguity is verifying how much of the total displacement and associated forces are generated due to the thermal expansion of the pebbles as opposed to the upper piston assembly, which includes: the piston rod, two ceramic plates, and the heater itself. In order to eliminate this confusion, the experimental procedure has been updated. This procedure separates expansion of piston-heater assembly from that of pebble bed by heating the piston-heater assembly to an equilibrium temperature before it (the heater) contacts and heats the pebble bed. The procedure defined below is to study pebble bed thermo-mechanics evolution for a fixed boundary configuration (simulating a fixed geometric container as in the blanket):

Experimental Procedure

1- Pack the pebble bed to about 63% packing fraction.

2- Make sure all thermocouples are installed in the designated positions in bed (3 TCs), piston (at the mid-plane location), and heater.

3- Assemble the quartz tube, the upper piston and test the vacuum pressure. Connect coolant lines.

4- Run the coolant at 525 ml/min.

5- Turn on the furnace middle heater to raise the background temperature to an initial low temperature gradient. Alternatively, the initial gradient can be established by relying on the coolant and radiant heat.

6- As the temperature starts to stabilize, lower the upper piston and run a force-controlled mode of a pre-compaction value (defined in test matrix) for 5 minutes. Record the piston crosshead position and mark it as the pebble bed surface reference point. This value will remain the fixed displacement boundary position throughout 4 thermal cycles. (A 4-thermal-cycles run is the first attempt.)

7- Retract the upper piston as far as possible from the pebble bed surface to minimize radiative bed heat-up, and take note of the piston maximum displacement that maintains vacuum conditions.

8- Turn on the heater at 130 W, and wait until the upper piston assembly temperature gets to the desired quasi-steady-state value depending on the power level response (preferably to about 600 ^{o}C or higher- to be determined.)

9- Start lowering the upper piston to the position recorded in step (6) as quickly as possible in order to make contact with the pebbles and capture most of the thermal induced stresses.

10- Fix the piston positon and run a displacement-controlled mode at 0 mm target and 24 hr wait for hold time.

11- Measure the induced forces as the bed heats up to near equilibrium temperatures or the slope begins to flatten out.

12- Turn off the heater and manually retract the piston to the position defined in step (7) and let the bed cool down to the initial baseline temperatures.

13- Turn the heater back on to step (8) temperature and repeat steps (9)-(11).

14- Repeat the above procedure under a pre-compaction load of 1 MPa and 2 MPa instead of 200 N after repacking the bed.

Specifically, we would like to consider pre-compaction load as a design parameter, where its effect on bed thermomechanics evolution will be studied. Here we define three pre-compaction loads in current experimental matrix.

Experimental Matrix

Set 1: 200 N initial load (Good contact/no compaction) followed by 3-4 thermal cycles under fixed piston displacement.

Set 2: 1 MPa pre-compaction load followed by 3-4 thermal cycles under fixed piston displacement.

Set 3: 2 MPa pre-compaction load followed by 3-4 thermal cycles under fixed piston displacement.

Experimental Considerations

1- Previous tests showed that radiation becomes a dominant mode of heat transfer as the piston approaches the bed, which prevents us from recording a substantial amount of thermal stresses. Therefore, the piston lowering and program setup time has to be minimized.

2- The heater temperature has to remain constant throughout the bed heat-up cycle in order to isolate the thermal expansion of the upper assembly. This has been tested, and the temperature remains constant within +- 3 ^{o}C. If larger deviation occurs, the heater power has to be adjusted accordingly to keep the upper piston assembly temperature fairly constant.

3- Previous results also showed that the forces measured during the cool-down period are strongly linked to the heater contraction since the stress drops much faster than the bed temperatures. Therefore, the cool down portion of the stress results will be neglected, and the piston will be immediately brought back to the initial position (away from the bed) in order to speed up the cooling process.

4- Due to the extreme sensitivity of the stress measurement to the total piston displacement, the experimental procedure has to be perfected and updated in order to isolate the stresses generated by the significantly smaller pebbles thermal strains compared to the piston and heater thermal expansion.

Expected Pebble-bed Behavior

The amount of stress induced by the imposed temperature gradient depends on the initial bed stress state. This is due to the bed elastic modulus dependence on compressive stress invariants. Additionally, the initial bed density significantly influences the bed mechanical behavior since the pebbles undergo more deformations under low initial density than under comparably high pre-compaction. This is due to the irreversible rearrangements and reorientations of the pebbles, and should not be confused with the creep deformation/stress relaxation mechanisms. Therefore, the stresses measured in the 2 MPa pre-compaction run are expected to be the highest since a much larger percentage of the pebbles thermal strains will be translated into direct normal stresses on the piston than pebbles rearranging.

As expected, preliminary tests have shown that at a delta temperature of 289 ^{o}C, the bed exerts a pressure of 0.86 MPa on the wall. However, for the same temperature gradient, this value increases to 1.48 MPa after the application of pre-compaction pressure of 1.625 MPa. Under a fixed boundary configuration, the force may decrease as cycle number increases (to be found out). The goal of this experiment is to provide concrete repeatable results to verify the above mentioned phenomena, and study the effects on heat transfer performance relevant to solid breeder blanket designs. Additionally, benchmarking FEM material models: the internal stresses developed in the pebble bed corresponding to different temperature gradients can be compared to the experimental results.

Appendix D. Further considerations on dielectric heating of ceramics

Microwave Hybrid Heating

- **Microwave Hybrid Heating (MHH):** heating a low-loss material to a critical temperature where microwave absorption becomes sufficient to cause self-heating.

-Preheating can be achieved by radiation of another high-loss (susceptor) material that couples well with microwave.

-More uniform temperature gradients result from the presence of an external heat source that minimizes surface heat losses.

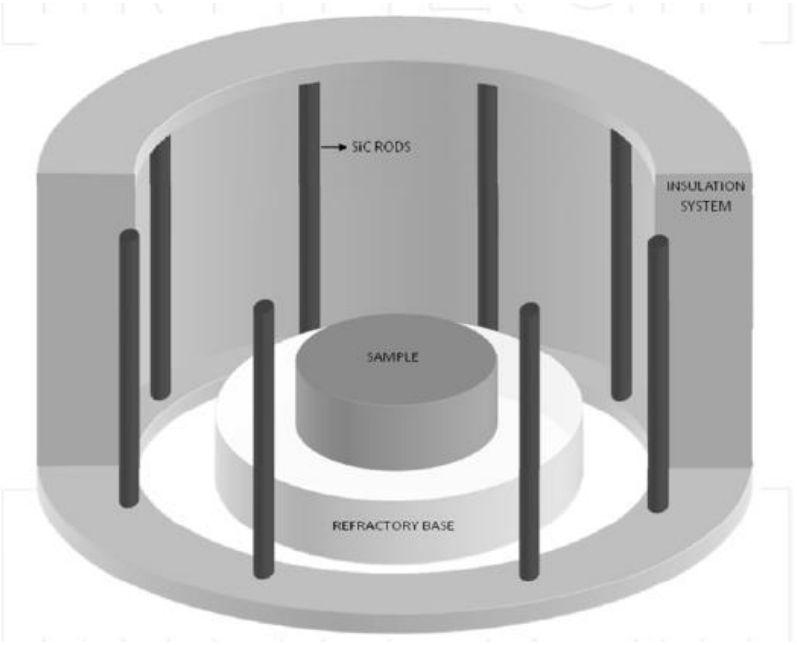

Figure D.1 Microwave Hybrid Heating example configuration

-The challenge for the system designer is to create a **controlled** environment by which ceramic materials can be brought to a sufficient self-heating temperature using a known susceptor.

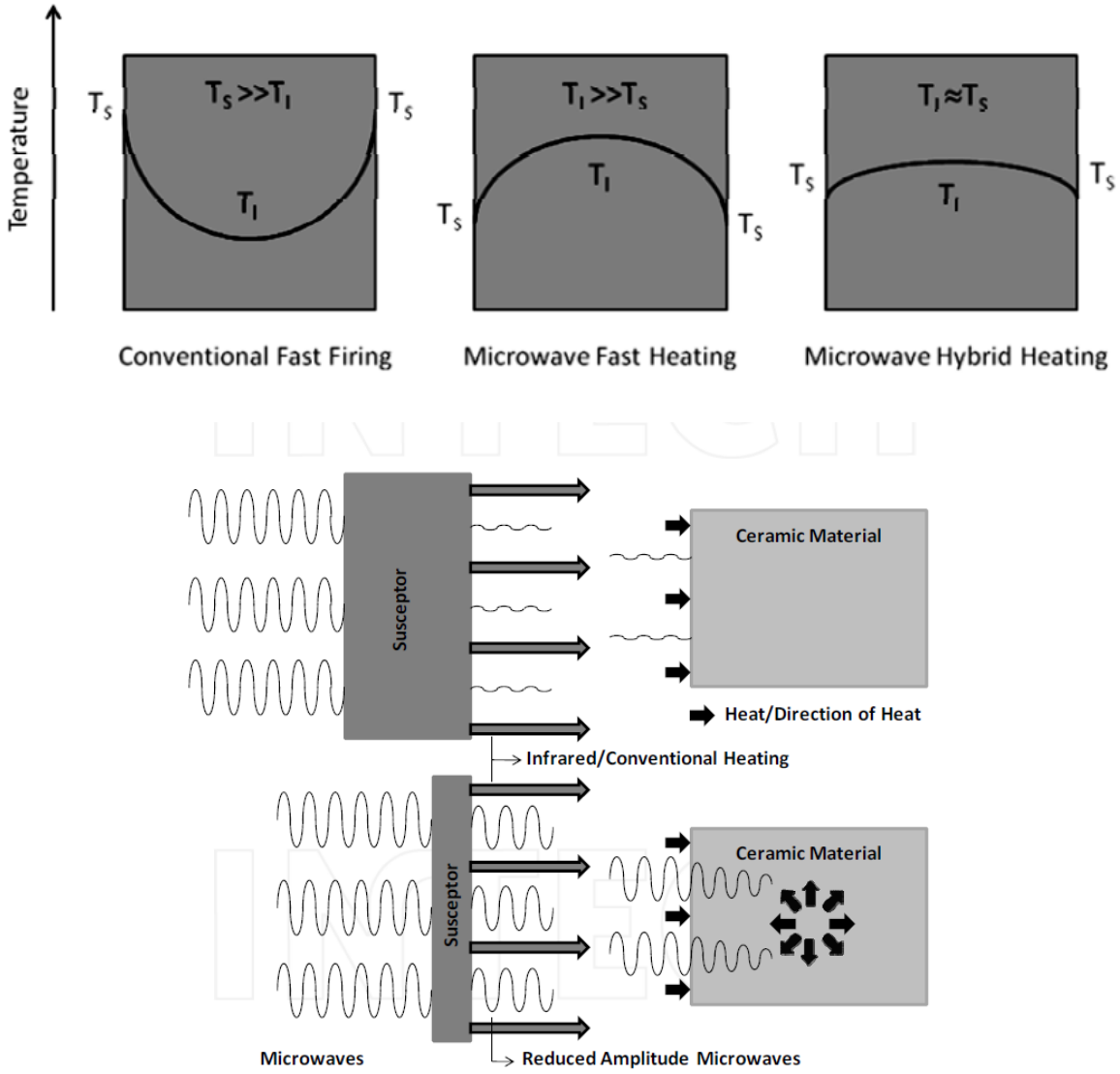

Figure D.2 Microwave Hybrid Heating example temperature profile

Considerations:

Thermal Runaway: Thermal instability caused by an increase in local temperature accompanied by an enhanced microwave energy absorption (rapid rise in the dielectric loss factor), which results in local acceleration of heating, a further rise in temperature in an uncontrolled manner.

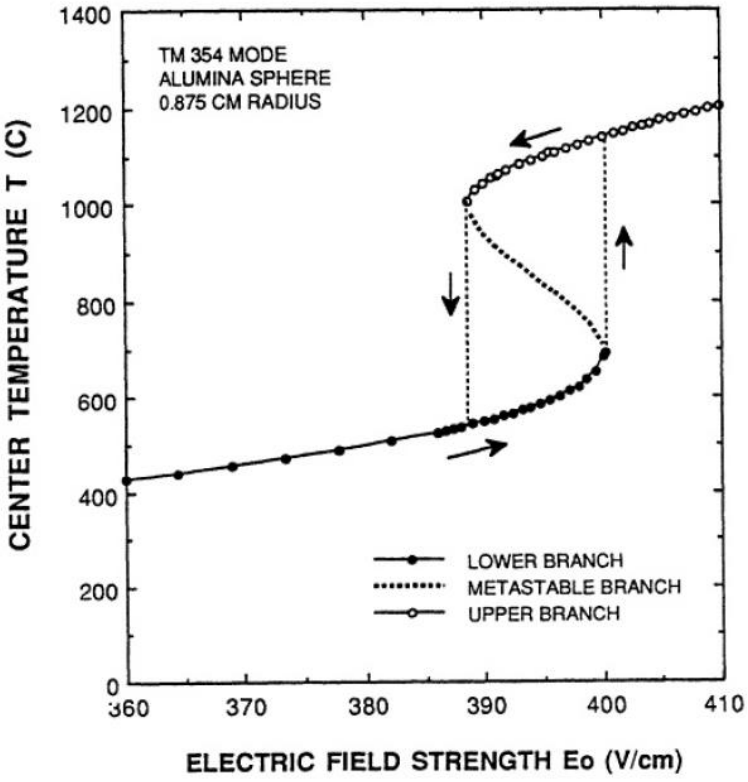

Figure D.3 S-type dynamic curve of temperature versus power

-This instability develops when microwave power exceeds some threshold value, which corresponds to an S-type dynamic curve of temperature versus power shown in Figure D.3. Below a "critical power level", the material will heat in a stable manner to a steady state value on the lower branch of the response curve. If the power is increased to exceed the upper critical power,

the temperature will jump to the upper branch of the temperature-power curve, giving rise to thermal runaway.

Temperature Measurement:

Typical thermocouples have proven ineffective for temperature sensing and control for microwave processing. Much early work using thermocouples led to misinterpretations of the results. The new equipment must use infrared pyrometers or Fiber Optic Temperature probes.

Non-thermal Influence on Mass Transport:

-Studies showed apparent evidence of accelerated kinetics for a range of processes. Kinetics of synthesis and sintering reactions of ceramic materials is reportedly augmented by two or three orders of magnitude or even more when conventional heating is substituted for microwave radiation.

Other Design Considerations

-Susceptors of various refractory-grade aluminas, silicon carbide, silicon/silicon carbide, carbon/graphite, zirconia and molydisilicide have been demonstrated to be effective heat sources that readily absorb electromagnetic radiation, depending on the frequency (RF KHz vs. microwave MHz to GHz). Aluminas and zirconia show better performance at higher microwave frequencies, while carbides do better at the lower RF range. One particular alumina susceptor is extremely durable and has been tested with heating rates in excess of 50°C per minute. The available frequencies for industrial power supplies are typically 450 KHz, 2.5-5 MHz, 915 MHz and 2450 MHz.

-Insulation choice plays an important role as well. Whether using fiber or brick, certain material systems absorb electromagnetic radiation while others are transparent. Another consideration is

part geometry, which will have a greater impact on design in order to determine the best susceptor geometry and position in relation to the part being fired.

The material being processed, production rates, powder vs. compact, and the behavior of the material in an electromagnetic field need to be considered for optimal design. Some materials can exhibit a thermal runaway condition once they begin to increase sintered density. This change in electromagnetic susceptibility with increased densification can introduce a variable that is very difficult to control. In many instances, the ability of the part or powder being processed to receive electromagnetic radiation can be more of a hindrance than a help.

-Consistency becomes extremely challenging if we rely solely on the ability of a material to receive electromagnetic radiation. In ceramic processing, the material being processed quite often may remain constant, but there are variations in mass and geometry that require different microwave processing parameters for each change. For these reasons, it's critical to design a system with known susceptors to create a stable heating environment whereby the influence of the process material's mass, geometry and electromagnetic susceptibility are minimized. Under these conditions, with microwave recipes properly established and automated, it is possible to produce the same quality of material from batch to batch. By comparison, the larger hot zones and variable temperatures in the currently used electrical resistance-heated furnaces create more heterogeneous sintering conditions.

Induction Heating

This report summarizes the electrical conductivity and permittivity of the silicate material and draws conclusions about the viability of using induction heating to simulate nuclear heating in Lithium Orthosilicate solid breeder.

Physical properties of Lithium Orthosilicate

Lithium Orthosilicate is an ionic solid electrolyte that is considered for use in lithium batteries as well as a solid breeder material for fusion. The critical properties for evaluation of induction heating are the electrical conductivity and permittivity of the material.

The data shown in Figure D.4 was converted into (S/m) versus T (K). It is evident that Li4SiO4 is a very poor electrical conductor with a strong temperature dependence. The highest value at 1100K is less than 100 S/m (to be compared to 316 SS with 1.25 MS/m at 300K). The implication of the low conductivity is that the skin depth will be very long in the silicate at typical induction heating frequencies.

For poor conductors the permittivity of the material does influence the skin depth at high frequencies. Figure D.5 shows the relative permittivity (divided by ε_0) versus temperature. This data indicates the silicate has a large dielectric constant.

The breakdown voltage for the silicate is shown in Figure D.6. The strong decrease in breakdown voltage may be an issue during disruptions at the desired operating temperature of a breeder.

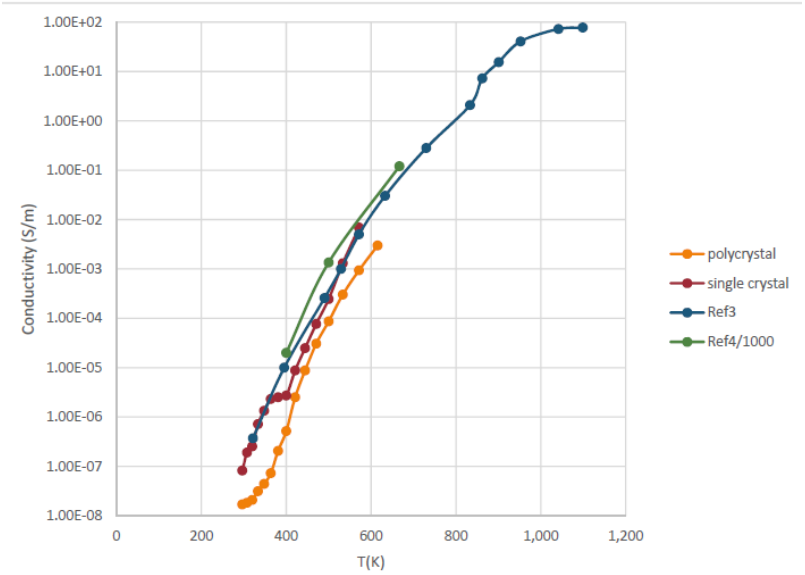

Figure D.4 The electrical conductivity of Lithium Orthosilicate versus temperature.

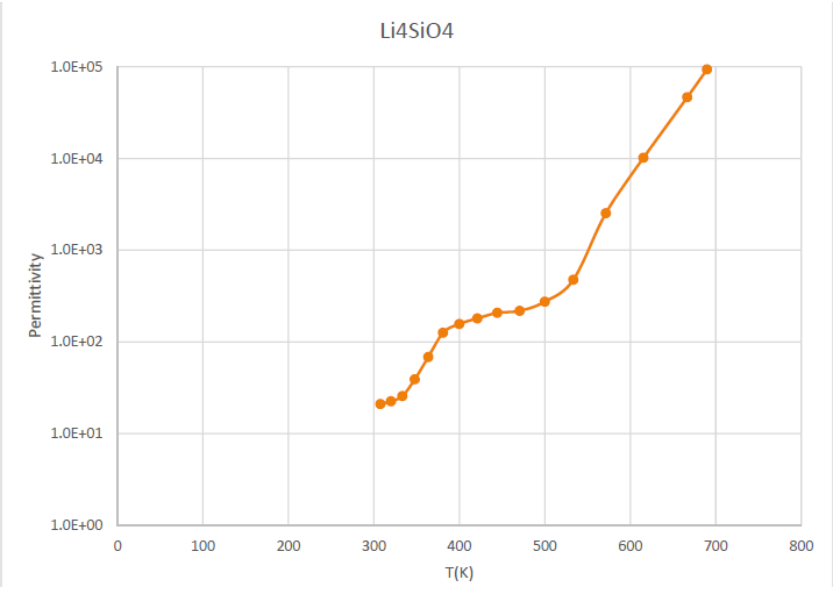

Figure D.5 The relative permittivity of Lithium Orthosilicate versus temperature.

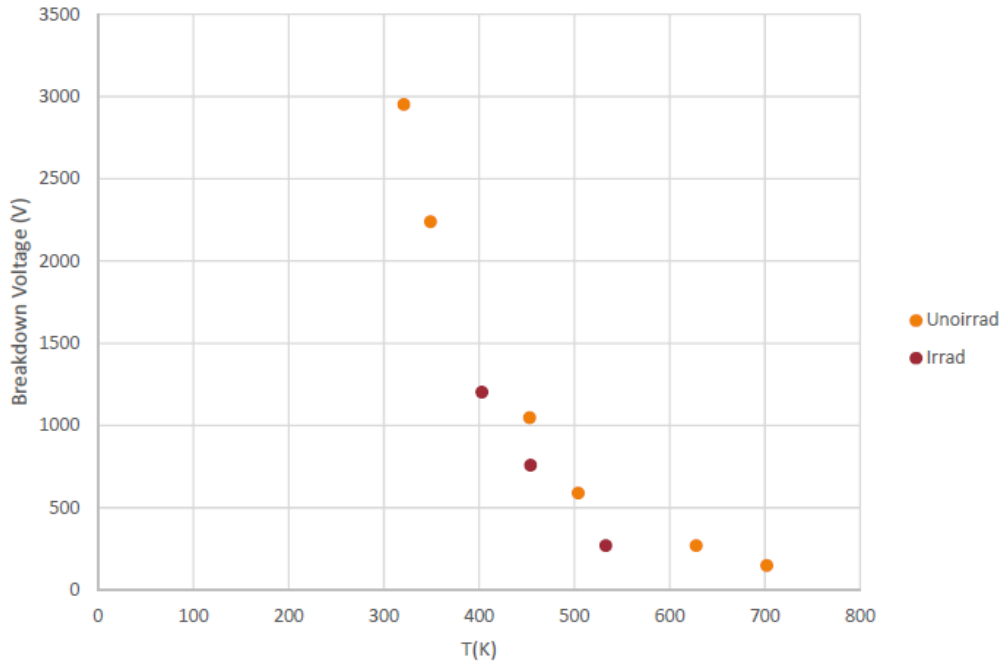

Figure D.6 The electrical breakdown voltage versus temperature

SKIN DEPTH ESTIMATE

An electromagnetic wave incident on a conducting surface is attenuated in the material over a characteristic distance known as the skin depth. For a highly conductive material the skin depth is given by

$$\delta = \sqrt{\frac{2\rho}{\omega\mu}}$$

where ρ is the electrical resistivity, ω is the angular frequency, and μ is the permeability. If the material has poor electrical conductivity, the polarizability (permittivity) of the material is important. For poor conductors the skin depth is given by

$$\delta = \sqrt{\frac{2\rho}{\omega\mu}} \sqrt{\sqrt{1+(\rho\omega\varepsilon)^2}+\rho\omega\varepsilon}$$

Since it appears one can make δ arbitrarily small at high frequency, it is important to take the limit at high frequency. At high frequency the above is approximately

$$\delta \approx 2\rho \sqrt{\frac{\varepsilon}{\mu}}$$

For a non-magnetic material like lithium orthosilicate $\mu=\mu_0$, we have

$$\delta \approx 2\rho \sqrt{\varepsilon} \sqrt{\frac{\varepsilon_0}{\mu_0}}$$

where ε is now the relative permittivity (or dielectric constant).

Since the breeder material is contained in a conducting box, any induction heating scheme must operate at a frequency low enough to have significant energy penetrate through the box wall. If we assume the box is SS316 and the wall is 4 mm thick, an operating frequency of 400 Hz will allow about 83% of the wave energy to be transmitted through the wall to the silicate. Table D.1 shows the estimated skin depth for various conditions without any doping of the silicate material. It is easy to see that none of the conditions create acceptable heating profiles in the silicate. Only very high frequency and hot silicate pebbles come close to having an acceptable e-folding length, but such high frequency waves will not penetrate the steel box.

Table D.1 The estimated skin depth for various conditions

Frequency (Hz)	Temperature (K)	Permittivity (ε/ε0)	Skin depth
400	300	ignored	59 km
400	1100	ignored	1.8 m
Very high	300	21	270 km
Very high	1100	10^5	17 mm
400	300	21	201 km
400	1100	10^5	2.5 m

The possibility of adding a higher conductivity material to the silicate pebbles to decrease the skin depth has been explored. Since the skin depth effect is due to generation of eddy currents in the conducting material that oppose the AC magnetic field, any added material would have to be arranged such that the eddy currents can flow. Small isolated pebbles of a highly conductive material would be surrounded by the very resistive silicate pebbles, it is very unlikely significant eddy currents would flow in the conductive pebbles (especially given the long wavelength of 400 Hz radiation). A wire mesh made from conductive material would likely allow eddy currents to form. However, the mesh would disturb the packing of the silicate pebbles and the mesh would have to have small mesh spacing and there would have to be several layers of mesh to replicate the heating profile in the silicate.

CONCLUSIONS AND RECOMMENDATIONS

Induction heating of a representative pebble bed may be possible, but considerable effort may be needed to determine the optimum configuration of metal mesh and pebbles. Additionally, the steel container surrounding the pebbles will limit the frequency that can be used.

Appendix E. Oil Heat Transfer Loop System Design

Any thermal fluid system requires the following basic components to operate:

(1) A pump that circulates the (2) heat transfer fluid though an (3) insulated piping system to a (4) heater that raises the fluid's temperature to a desired value that provides adequate boundary conditions at the test article or process equipment. An (5) expansion tank is needed to allow for the expansion and contraction of the fluid during heating and cooling cycles respectively. In addition to Pressure Safety Valves, Control Valves, Catch Tanks, drains and vents depending on the application.

Thermal Fluid System Design Considerations:

Fluid Selection

Safety – Flash Point, Fire point, and AIT have to be well above operating temperature.

Thermal Stability- The ability of the oil to withstand molecular cracking at specified temperatures. It is a primary factor in determining the appropriate operating temperatures.

Overall Heat Transfer Coefficient- Plays an important role in evaluating the heat transfer rate for a specific flow speed and pipe diameter.

Pump-ability Point- The temperature at which the pump can no longer circulate the oil due to its high viscosity.

Other fluid selection parameters include serviceability, cost, disposal and transport.

Pump Selection

A centrifugal pump should be selected according to the desired ranges of flow rate, required head, appropriate cold start temperature for the oil, and compatibility with the heat transfer fluid.

Heater Sizing and Selection

The heater should be selected according to the required heat load while accounting for at least 10-20% heat losses. Oil heaters are available on the market with various configurations and capacities depending on the application.

Expansion Tank Size and Selection

The operating temperature and the coefficient of thermal expansion of the oil should be carefully considered before sizing the expansion tank in order to accommodate for any volume fluctuations during heating and cooling cycles. The main purpose of the tank is to keep the system full; it provides space for the fluid to expand during heating, and it adds fluid to the system during contraction as a result of cooling. It is also important to monitor the level of fluid in the tank in order to check for leakages. The temperature inside the tank should be always maintained below a certain value that is different for every fluid in order to prevent oxidation. A nitrogen blanket may be required if the temperature is meant to exceed that value.

Insulation

In the case of poorly selected insulation, any oil leakages may penetrate through the insulation at high temperatures, and spontaneous ignition may occur if the system is exposed to air. Therefore, for safety reasons, insulation should be carefully designed, especially around valves, gaskets, and welds. Closed-cell insulation is usually preferred to avoid penetration.

Piping System

Piping material has to be compatible with the oil used. For example, brass, copper, or aluminum cannot be used with thermal oils as these materials act as oxidation catalysts. Thus, carbon steel or Stainless Steel should be used. There are general guidelines for piping selection that should be followed to minimize/prevent leakages, stresses, and unnecessary pressure drops in the system. Those can be found online on the ASME website.

Flow Measurement & Control

Flow control is a key component in any fluid loop. Flow meters/regulators serve two purposes in the system. First, they provide a real indication of the flow rate in the system at the desired location regardless of the user set point. Second, they reveal hidden failures in the system that can cause a disaster. These can be failures related to the heater, pump motor, defective valves, or leakages. Therefore, for safety reasons, the flow meters have to be incorporated in the control loop to trigger a low-flow shutdown in case of an incident.

Temperature Control

Like flow measurement, temperature monitoring serves obvious functions in addition to safety. Controlling the system temperature within a certain range via PID controllers linked to a computer interface can be an efficient means of maintaining flow temperatures at the desired values. Temperature sensors have to be placed in strategic locations to give a meaningful and representative measurement of the system temperature and the level of uniformity.

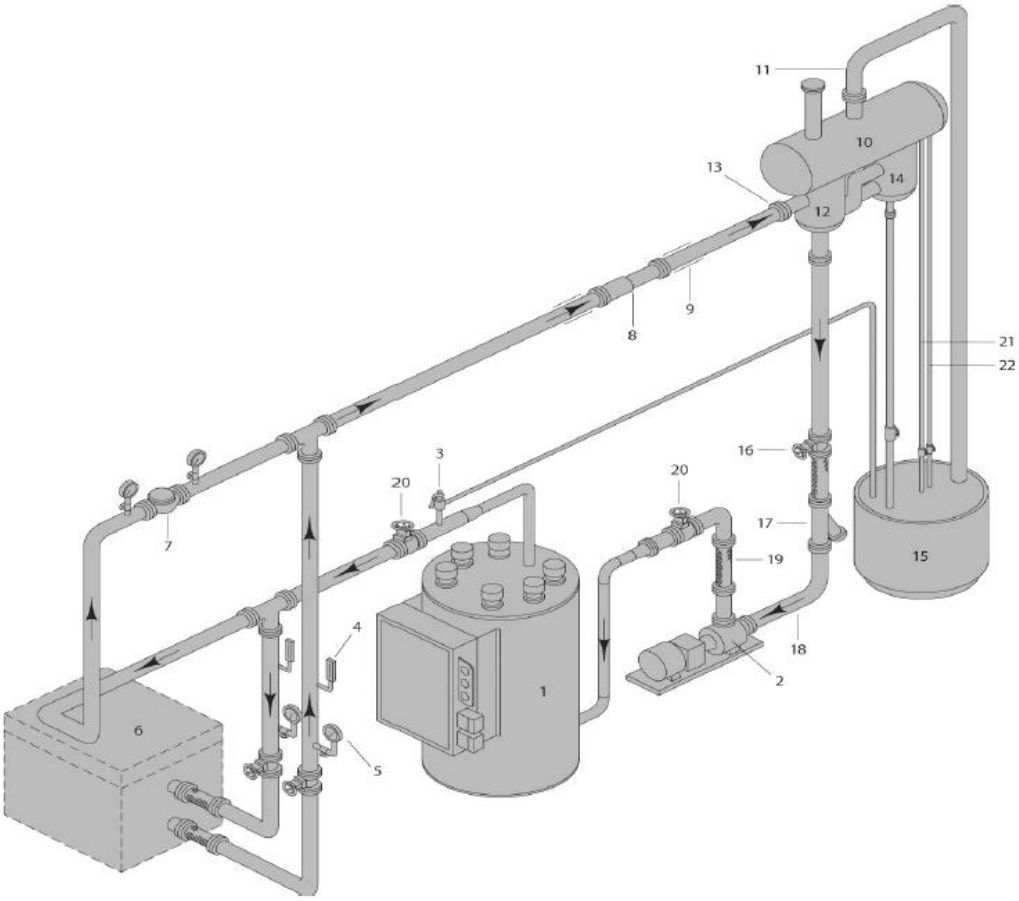

Figure E.1. Basic Fluid Loop Components

(1) Thermal Fluid Heater, (2) Thermal Fluid Circulating Pump, (3) Safety Relief Valve, (4) Thermocouple, (5) Pressure Gauge, (6) Thermal Fluid Heated Equipment, (7) Bypass Valve to maintain full flow to heater, (8) Expansion Joints (9) Anchor and Pipe Guides, (10) Expansion Tank, (11) Vent Piping, (12) De-aerator Tank, (13) De-aerator Tank inlet, (14) Thermal Buffer Tank, (15) Catch Tank for drain of pressure relief valve, cold seal, expansion tank, and vent, (16) Gate Valve, (17) Strainer, (18) System Fill Connection, (19) Flexible Connection, (20) Isolating Valve, (21) Manual Low Level Test Line, (22) Manual High Level Test Line.

The Start-up Procedure

1. First you start your system pump to get the fluid flowing through the system.
2. Second, after you know you have good flow, you apply the heat. Heat should be applied in 11°C to 14°C increments until the heat transfer fluid gets to a viscosity of 10 cP (centipoise) or less. The reason for this is to ensure that you have turbulent flow through the heater (where the heat transfer fluid can remove just as much heat as the heater can supply to the coil in the heater) and there will be no thermal cracking of the oil.
3. These increment steps are done by taking a system from 21°C and increasing the heat by 11°C and letting the system run until the temperature on the heater reads 32°C. Once the heater reads that then dial it up another 11°C.
4. Keep dialing up the heater to your desired safe operating temperature.

Things to watch for are the level in the expansion tank should rise as the heat transfer fluid expands. If it does not, you may have a line clogged. Also, at the 93°C temperature, you may occur some pump cavitation. If you do, that means you have water or some light end molecules that are low boilers in your system.

The Shutdown Procedure - This procedure is more than just going to the heater and shutting the pump and heater off at the same time. If you do your shut down this way, the residual heat that is left in the heater can exceed the film temperature of the oil and thermal crack the oil that is not moving through the pipe. What we would suggest you do as a shutdown procedure is:

1. Turn off the heater first.
2. Let the pump continue to circulate the heat transfer fluid to remove any residual heat that is in

the heater, the process and the pipes. For some systems this may take a while depending on your system size. The reason for this is to make sure that when the pump gets turned off, the residual heat in the various components of the system does not thermally crack the heat transfer fluid.
3. Once the temperature has dropped to 93°C the residual heat has been removed and you are safe to shut off the pump.

Standard Operating Procedures - Once you get the heat transfer fluid system up and running, it should run pretty much on its own.

But here are some daily things to keep an eye on when operating your system:

· Check the temperature of the oil returning to the heater as well as the oil exiting the heater. When your system is running smooth & efficient, the temperature difference should remain constant. If the temperature difference increases, that is an indication that something is changing in your system.
· When checking the temperatures, you should also check the pressure drop across the pump and through the heater. If there are no changes in pressure drops, everything is fine. If there are changes, then your system is telling you there is a problem.
· Check the pump out - is it running smooth, making noise, leaking oil or what appears to be smoking?
· Check the heater out - walk around it and make sure that the outer case is ok. Check for leaking oil, burning of paint, nothing appears to be loose or out of place. If you have a flow meter, make sure that the flow rate does not change.
· Check the expansion tank - is the paint burnt off, are there leaks, does it make noise, does it smell, is the oil at the normal level, does the level tube appear to be clogged, is there what

appears to be smoking coming from the vent pipe?

· Walk the piping system - check all elbows and connections for leaks (if there is --never open up insulation to find the leak when the system is hot - this is one of the ways you can start a fire - let the system cool down before investigating the leak), any pungent odors, all gates or vents or valves appear to be operating properly, is there what appears to be smoke coming from any of the sections, any different noises from normal?

References

[1] Enoeda, Mikio, et al. "Design and technology development of solid breeder blanket cooled by supercritical water in Japan." *Nuclear Fusion* 43.12 (2003): 1837.

[2] Knitter, R., Alm,B., Roth,G., 2007.J.Nucl.Mater.367–370, 1387–1392. 113. Roux, N.,Tanaka,S.,Johnson,C.,Verrall,R.,1998.FusionEng.Des.41,31–38.

[3] G. Piazza, J. Reimann, E. Günther, R. Knitter, N. Roux, and J. D. Lulewicz. Characterisation of ceramic breeder materials for the helium cooled pebble bed blanket. Journal of Nuclear Materials, 307-311(0):811–816, dec 2002.

[4] J. Reimann, L. Boccaccini, M. Enoeda, and A. Ying. Thermomechanics of solid breeder and Be pebble bed materials. Fusion Engineering and Design, 61-62:319–331, nov 2002.

[5] J. Reimann, D. Ericher, and G. Wörner. Influence of pebble bed dimensions and filling factor on mechanical pebble bed properties. Fusion Engineering and Design,69(1-4):241–244, 2003.

[6] Y. Gan and M. Kamlah. Thermo-mechanical analysis of pebble beds in HELICA mock-up experiments. Fusion Engineering and Design, 83(7-9):1313–1316, Dec 2008.

[7] J. G. van der Laan, A. Fedorov, S. van Til, and J. Reimann. Ceramic Breeder Materials.Technical report, 2011.

[8] H. Tanigawa, M. Enoeda, and M. Akiba. Measurement of thermal expansion of Li2TiO3 pebble beds. Fusion Engineering and Design, 82(15-24):2259–2263, Oct 2007.

[9] L. Bühler and J. Reimann. Thermal creep of granular breeder materials in fusion blankets. Journal of Nuclear Materials, 307-311:807–810, dec 2002.

[10] J. Reimann and H. Harsch. Thermal creep of beryllium pebble beds. Fusion Engineering and Design, 75-79:1043–1047, nov 2005.

[11] J. Reimann and G. Wörner. Thermal creep of Li4SiO4 pebble beds. Fusion Engineering and Design, 58-59:647–651, nov 2001.

[12] J. H. Fokkens. Thermo-mechanical Finite Element Analyses for the HCPB In-pile Test Element, 2003.

[13] Y. Gan and M. Kamlah. Identification of material parameters of a thermo-mechanical model for pebble beds in fusion blankets. Fusion Engineering and Design, 82(2):189– 206, feb 2007.

[14] G. Dell'Orco, P. A. Di Maio, R. Giammusso, A. Tincani, and G. Vella. A constitutive model for the thermo-mechanical behaviour of fusion-relevant pebble beds and its application to the simulation of HELICA mock-up experimental results. Fusion Engineering and Design, 82(15-24):2366–2374, oct 2007.

[15] G. Dell'Orco, P. A. Di Maio, R. Giammusso, A. Tincani, and G. Vella. On the theoretical–numerical study of the HEXCALIBER mock-up thermo-mechanical behavior. Fusion Engineering and Design, 85(5):694–706, aug 2010.

[16] P. A. Di Maio, G. Dell'Orco, R. Giammusso, A. Malavasi, I. Ricapito, A. Tincani, and G. Vella. Experimental tests and thermo-mechanical analyses on the HEXCALIBER mock-up. Fusion Engineering and Design, 83(7-9):1287–1293, dec 2008.

[17] P. A. Di Maio, R. Giammusso, and G. Vella. On the hyperporous non-linear elasticity model for fusion-relevant pebble beds. Fusion Engineering and Design, 85(7-9):1234– 1244, 2010.

[18] Y. Gan and M. Kamlah. Thermo-mechanical analyses of HELICA and HEXCALIBER mock-ups. Journal of Nuclear Materials, 386-388:1060–1064, Apr 2009.

[19] Y. Gan and M. Kamlah. Thermo-mechanical modelling of pebble bed–wall interfaces. Fusion Engineering and Design, 85(1):24–32, Jan 2010.

[20] Y. Gan, M. Kamlah, H. Riesch-Oppermann, R. Rolli, and P. Liu. Crush probability analysis of ceramic breeder pebble beds under mechanical stresses. Journal of Nuclear Materials, pages 10–13, Dec 2010.

[21] P. A. Cundall and O. D. L. Strack. A discrete numerical model for granular assemblies. Geotechnique, 29(1):47–65, 1979.

[22] Z. Lu, A. Y. Ying, and M. A. Abdou. Numerical and experimental prediction of the thermomechanical performance of pebble beds for solid breeder blanket. Fusion

Engineering and Design, 49-50:605–611, 2000.

[23] A. Y. Ying, H. Huang, and M. A. Abdou. Numerical simulation of ceramic breeder pebble bed thermal creep behavior. Journal of Nuclear Materials, 307-311:827–831, dec 2002.

[24] Z. An, A. Y. Ying, and M. A. Abdou. Application of discrete element method to study mechanical behaviors of ceramic breeder pebble beds. Fusion Engineering and Design, 82(15-24):2233–2238, 2007.

[25] Y. Gan and M. Kamlah. Discrete element modelling of pebble beds: With application to uniaxial compression tests of ceramic breeder pebble beds. Journal of the Mechanics and Physics of Solids, 58(2):129–144, Feb 2010.

[26] J. T. Van Lew, A. Ying, and M. A. Abdou. A discrete element method study on the evolution of thermomechanics of a pebble bed experiencing pebble failure. Fusion Engineering and Design, 89(7-8):1151–1157, Oct 2014.

[27] G. Dell'Orco, P. A. Di Maio, R. Giammusso, A. Malavasi, L. Sansone, A. Tincani, and G. Vella. Progress in the benchmark exercise for analyzing the lithiate breeder pebble bed thermo-mechanical behaviour. Fusion Engineering and Design, 81(1-7):169–174, Feb 2006.

[28] A. Magielsen, M. M. W. Peeters, J. Hegeman, M. Stijkel, and J. G. van der Laan. Analysis of the in-pile operation and preliminary results of the post-irradiation dismantling of the pebble bed assemblies, presented at the 8th ISFNT, 2007.

[29] Park, Yi-Hyun, et al. "Optimization of mass-production conditions for tritium breeder pebbles based on slurry droplet wetting method." Fusion Engineering and Design, 109–111, 443 (2016).

[30] C. ZHANG et al., "Ceramic breeder pebble bed packing stability under cyclic loads," Fusion Engineering and Design, 109, 267-271 (2016).

[31] Y. GAN et al., "Thermal discrete element analysis of EU solid breeder blanket subjected to neutron irradiation," Fusion Science and Technology, 66(1), 83-90 (2014).

[32] J. T. VAN LEW, et al., "Numerical study on influences of bed resettling, breeding zone orientation, and purge gas on temperatures in solid breeders," Fusion Engineering and Design, 109–111, 539 (2016).

[33] M. Abdou, et al., "Challenges and Pathways for Fusion Nuclear Science and Technology toward DEMO", Keynote Presentation at the 12th International Symposium on Fusion Nuclear Technology (ISFNT-12), Jeju, Korea, September 14, 2015.

[34] F. Hernándeza, et al., "Set-up of a pre-test mock-up experiment in preparation for the HCPB Breeder Unit mock-up experimental campaign," Fusion Engineering and Design, 2378– 2383, 88 (2013).

[35] TEKSCAN, Inc. The Difference Between Film & Tactile Sensors for Pressure Measurements, Machine Design (2016).

[36] Mechanical APDL Theory Reference, ANSYS release 14.0 (2011).